THE UNIVERSITY OF CHICAGO

THE NUCLEON AXIAL FORM FACTOR AND STAGGERED LATTICE QCD

A DISSERTATION SUBMITTED TO
THE FACULTY OF THE DIVISION OF THE PHYSICAL SCIENCES
IN CANDIDACY FOR THE DEGREE OF
DOCTOR OF PHILOSOPHY

DEPARTMENT OF PHYSICS

BY
AARON SCOTT MEYER

CHICAGO, ILLINOIS
JUNE 2017

TABLE OF CONTENTS

LIST OF FIGURES

LIST OF TABLES

ACKNOWLEDGMENTS

I would like to thank Richard Hill and Andreas Kronfeld for their continued support throughout my graduate school education. Without their wisdom and expertise, this research would not have been possible.

I would like to thank my thesis committee for their helpful advice while preparing for my defense and for accommodating my expedited schedule. I would like to thank Jim Simone for imparting his coding expertise to me. I thank Zech Gelzer, Ciaran Hughes, Max Hutchinson, Jim Simone, for useful discussions. I would additionally like to thank Katy Colleton, Max Hutchinson, Ciaran Hughes, Seyda Ipek, and Tracey Ziev for providing me with food and much-needed distractions during my final work binge while writing this thesis.

Support for this research was provided by was supported by DOE Grant No. DE-FG02-13ER41958, the U.S. Department of Energy, Office of Science Graduate Student Research (SCGSR) program, and the Visiting Scholars Award Program of the Universities Research Association. The SCGSR program is administered by the Oak Ridge Institute for Science and Education for the DOE under Contract No. DE-AC05-06OR23100. Support for travel was provided by the UChicagoGRAD travel grant, the American Physical Society FGSA travel award, and the Institute for Advanced Study, Technical University of Munich. I would like to thank the Kavli Institute for Theoretical Physics, which is supported by the National Science Foundation under Grant No. PHY11-25915, for its hospitality.

Computation for this work was done on the USQCD facilities at Fermilab and, for the MILC ensembles, at the Argonne Leadership Computing Facility, the National Center for Atmospheric Research, the National Center for Supercomputing Resources, the National Energy Resources Supercomputing Center, the National Institute for Computational Sciences, the Texas Advanced Computing Center, and under grants from the NSF and DOE. Fermilab is operated by Fermi Research Alliance, LLC, under Contract No. DE-AC02-07CH11359 with the United States Department of Energy.

ABSTRACT

The study of neutrino oscillation physics is a major research goal of the worldwide particle physics program over the upcoming decade. Many new experiments are being built to study the properties of neutrinos and to answer questions about the phenomenon of neutrino oscillation. These experiments need precise theoretical cross sections in order to access fundamental neutrino properties. Neutrino oscillation experiments often use large atomic nuclei as scattering targets, which are challenging for theorists to model. Nuclear models rely on free-nucleon amplitudes as inputs. These amplitudes are constrained by scattering experiments with large nuclear targets that rely on the very same nuclear models. The work in this dissertation is the first step of a new initiative to isolate and compute elementary amplitudes with theoretical calculations to support the neutrino oscillation experimental program.

Here, the effort focuses on computing the axial form factor, which is the largest contributor of systematic error in the primary signal measurement process for neutrino oscillation studies, quasielastic scattering. Two approaches are taken. First, neutrino scattering data on a deuterium target are reanalyzed with a model-independent parametrization of the axial form factor to quantify the present uncertainty in the free-nucleon amplitudes. The uncertainties on the free-nucleon cross section are found to be underestimated by about an order of magnitude compared to the ubiquitous dipole model parametrization.

The second approach uses lattice QCD to perform a first-principles computation of the nucleon axial form factor. The Highly Improved Staggered Quark (HISQ) action is employed for both valence and sea quarks. The results presented in this dissertation are computed at physical pion mass for one lattice spacing. This work presents a computation of the axial form factor at zero momentum transfer, and forms the basis for a computation of the axial form factor momentum dependence with an extrapolation to the continuum limit and a full systematic error budget.

CHAPTER 1

INTRODUCTION

The nonzero mass of the neutrinos, a consequence of neutrino flavor oscillation, is one of the few instances of physics beyond the Standard Model. This discovery has sparked a worldwide interest in neutrino oscillation physics and the creation of many new neutrino oscillation experiments. Several accelerator-based neutrino oscillation experiments are being built or are ongoing in Europe, Japan, and the US. These experiments seek to make precision measurements of neutrino oscillation parameters and to definitively determine the few remaining unknowns, including the neutrino mass ordering and the possibility of charge-parity violation in the lepton sector. To back up the experimental precision goals, a corresponding improvement in the theoretical precision is needed.

One of the difficulties facing precision measurements in neutrino oscillation experiments is that the target consists of large atomic nuclei, which must be modeled before fundamental physics can be extracted. Currently, nuclear models are subject to a certain redundancy from their construction. Nuclear models are built from free-nucleon amplitude inputs. The free nucleon amplitudes are often determined from data taken on large nuclear targets, which in turn have been extracted assuming some form for the nuclear model. Free-nucleon targets in neutrino beams, on the other hand, often have too few statistics to constrain the nucleon amplitudes. This circularity is difficult to break, since neutrino interaction experiments have traditionally been the only way to access certain hadronic matrix elements.

Lattice QCD is a tool that has been successful in computing the baryon spectrum and a wide range of matrix elements in the mesonic sector. Lattice QCD computations use first principles to determine the physical quantities from a numerical solution to the path integral. Precision calculations of some hadron masses and hadronic matrix elements are reaching the sub-percent level. Computations for baryonic physics are now at the point that mesonic physics was a decade ago. This means that lattice QCD is a tool that may be used to determine physics involving free nucleons, which is difficult to determine experimentally.

The goal of this thesis is driven by these considerations. The work presented here seeks to determine the nucleon axial form factor from theoretically clean data. The first approach is to fit to the cleanest data from experiment available, deuterium bubble chamber data, using a new model-independent parametrization. This parametrization helps to understand the true systematic errors on the free-nucleon amplitudes used in nuclear models. The second approach is to use lattice QCD to perform a first-principles calculation of the axial form factor at zero momentum transfer. This calculation is free from nuclear corrections and can be used as an input to nuclear models used to constrain oscillation data. Later extensions of this work will seek to determine the full momentum dependence of the axial form factor from first principles.

The chapters of this dissertation are organized as follows. The remainder of the first chapter is an introduction to both neutrino physics and to lattice QCD. This chapter is meant to give the background for the work presented in the rest of this dissertation. Chapter 2 deals with fits to deuterium bubble chamber data using the z expansion framework, a model-independent parametrization meant to replace the dipole form factor model parametrization. Chapter 3 describes the group theory necessary to explain the computational results presented in the following chapters. Chapter 4 details the computation of the mass spectrum of the baryon sector using staggered lattice QCD. A blinded computation of the axial charge, the value of the axial form factor at zero momentum transfer, is presented in Chapter 5. Chapter 6 contains remarks about the results of this thesis and discusses how work completed here will be extended in the future.

1.1 Neutrino Oscillation

1.1.1 Physics of Neutrino Oscillations

The neutrino flavor eigenstates are defined according to the leptons that they produce when interacting with matter. For quasielastic scattering, a simple neutrino interaction with a

nucleon, the reaction proceeds according to its flavor eigenstate,

$$\nu_\ell + n \to \ell^- + p\,, \tag{1.1}$$

where ℓ represents by any of the three neutrino flavors, e, μ, or τ. Similarly for antineutrino beams, the characteristic process is $\bar{\nu}_\ell p \to \ell^+ n$.

The flavor eigenstates are distinct from the mass eigenstates, which are the states that propagate through spacetime via Hamiltonian time evolution. The mass eigenstates are a linear combination of the flavor eigenstates described by the change of basis

$$|\nu_\alpha\rangle = \sum_i U^*_{\alpha i} \, |\nu_i\rangle \ , \tag{1.2}$$

where α is a flavor index, i is a mass eigenstate index, and U is known as the PMNS (Pontecorvo-Maki-Nakagawa-Sakata) matrix. It is usually parametrized as [1]

$$\begin{aligned} U &= \begin{pmatrix} 1 & 0 & 0 \\ 0 & c_{23} & s_{23} \\ 0 & -s_{23} & c_{23} \end{pmatrix} \begin{pmatrix} c_{13} & 0 & s_{13}e^{-i\delta} \\ 0 & 1 & 0 \\ -s_{13}e^{+i\delta} & 0 & c_{13} \end{pmatrix} \begin{pmatrix} c_{12} & s_{12} & 0 \\ -s_{12} & c_{12} & 0 \\ 0 & 0 & 1 \end{pmatrix} \\ &= \begin{pmatrix} c_{12}c_{13} & s_{12}c_{13} & s_{13}e^{-i\delta} \\ -s_{12}c_{23} - c_{12}s_{23}s_{13}e^{+i\delta} & c_{12}c_{23} - s_{12}s_{23}s_{13}e^{+i\delta} & s_{23}c_{13} \\ s_{12}s_{23} - c_{12}c_{23}s_{13}e^{+i\delta} & -c_{12}s_{23} - s_{12}c_{23}s_{13}e^{+i\delta} & c_{23}c_{13} \end{pmatrix} \end{aligned} \tag{1.3}$$

with $c_{ij} \equiv \cos\theta_{ij}$, $s_{ij} \equiv \sin\theta_{ij}$, and $\delta \equiv \delta_{CP}$ a phase that violates charge-parity (CP) symmetry. The θ_{ij} are the neutrino mixing angles that govern the amplitude for the change from the produced flavor to the detected one, a phenomenon known as neutrino oscillation.

Computing the oscillation probability is an exercise in quantum mechanics. The propa-

gation of neutrinos proceeds as a plane wave solution

$$|\nu_i(\vec{x},t)\rangle = e^{-ip\cdot x}\,|\nu_i\rangle = e^{-iE_it+i\vec{p}\cdot\vec{x}}\,|\nu_i\rangle = e^{-iE_it}e^{+i|p|L}\,|\nu_i\rangle\ , \tag{1.4}$$

where $\hbar = c = 1$. In the limit where $E_i \gg m_i$, the momentum is approximately

$$p = E_i\sqrt{1-\frac{m_i^2}{E_i^2}} \approx E - \frac{1}{2}\frac{m_i^2}{E}\,, \tag{1.5}$$

which gives

$$|\nu_i(t)\rangle \approx e^{-iE(t-L)}e^{-im_i^2L/2E}\,|\nu_i\rangle\ . \tag{1.6}$$

In the limit where $E \gg m_i$, one has $t \approx L$, so the first exponential is unity and only the second is relevant. The oscillation probability is then the square of the matrix element connecting the two flavor eigenstates,

$$\begin{aligned}\mathcal{M}_{\alpha\beta}(L/E) = \big|\,\langle\nu_\beta(t)|\nu_\alpha(0)\rangle\,\big|^2 &= \left|\sum_i U_{\beta i}U^*_{\alpha i}e^{-im_i^2L/2E}\right|^2 \\ &= \sum_i U_{\alpha i}U^*_{\alpha i}U_{\beta i}U^*_{\beta i} + \sum_{i>j} U_{\beta i}U^*_{\alpha i}U^*_{\beta j}U_{\alpha j}e^{-i(m_i^2-m_j^2)L/2E} \\ &+ \sum_{i>j} U^*_{\beta i}U_{\alpha i}U_{\beta j}U^*_{\alpha j}e^{+i(m_i^2-m_j^2)L/2E}\,.\end{aligned} \tag{1.7}$$

Using the relation (from the form of the PMNS matrix, Eq. (1.3)),

$$\sum_i U_{\alpha i}U^*_{\alpha i}U_{\beta i}U^*_{\beta i} = \delta_{\alpha\beta} - \sum_{i>j}\Big(U_{\beta i}U^*_{\alpha i}U^*_{\beta j}U_{\alpha j} + U^*_{\beta i}U_{\alpha i}U_{\beta j}U^*_{\alpha j}\Big) \tag{1.8}$$

the matrix element may be rewritten

$$\mathcal{M}_{\alpha\beta}(L/E) = \delta_{\alpha\beta} - 4\sum_{i>j} \mathrm{Re}\left[U_{\beta i}U^*_{\alpha i}U^*_{\beta j}U_{\alpha j}\right] \sin^2\left(\Delta m^2_{ij}L/4E\right) + 2\sum_{i>j} \mathrm{Im}\left[U_{\beta i}U^*_{\alpha i}U^*_{\beta j}U_{\alpha j}\right] \sin\left(\Delta m^2_{ij}L/2E\right) , \quad (1.9)$$

where $\Delta m^2_{ij} \equiv m^2_i - m^2_j$.

To understand neutrino oscillations in detail, including the prospect of CP violation, it is necessary to know the parameters of the PMNS matrix as precisely as possible. Experiments measure the mass-squared splittings via the E dependence in the sine functions and the PMNS matrix elements, or equivalently, the mixing angles via the size of the oscillatory behavior. These parameters are determined by measuring neutrino survival, disappearance, or appearance probabilities and comparing them to an assumed set of PMNS matrix parameter values. The primary channels that are used to study neutrino oscillations are through electron antineutrinos (which are produced as a byproduct of nuclear reactors) or muon neutrinos (which are created in accelerator experiments through a decay chain). These interaction channels give experimental constraints on only a few elements of the PMNS matrix, although the goal is to eventually test unitarity of the PMNS matrix by constraining all of the matrix entries. A violation of unitarity would indicate the existence of some unknown particle that mixed with the neutrinos to produce a larger unitary matrix of which the 3×3 PMNS matrix is a non-unitary submatrix.

1.1.2 Neutrino Flux and Quasi-Elastic Cross Section

For accelerator neutrino oscillation experiments, measuring oscillation parameters requires knowledge of the neutrino beam flux. The beam creation process makes this determination quite difficult to do because of how the beam is constructed [2]. In these experiments, an initial beam of protons is launched at a target, which emits a stream of particles including

pions. These pions are focused by a magnetic horn, which also acts as a filter that selects particles based on their charge. The focused pions are sent down a decay pipe, where the pions decay into muons and muon neutrinos. The muons are stopped by the rock between the decay pipe and the detector, so the non-neutrino particles are filtered out before reaching the detector.

Other particle decays may generate neutrinos, making it impossible to discern which particle decays generated each neutrino. Contamination from antineutrinos or from other flavors of neutrinos from different decay channels are a concern and, if not properly handled, may fake a neutrino oscillation signal. Furthermore, the energy spectrum of the neutrino beam is not well controlled as, for example, an electron beam. This is an effect of the decay chain employed to create the beam. These factors force neutrino experiments to measure the flux at both a near and far detector. The near detector serves to measure the unoscillated neutrino energy spectrum, which is then compared to the oscillated neutrino spectrum at the far detector.

Measurements of the flux at the near and far detector are not simple. The typical strategy is to measure the flux on some large nuclear target. The nuclear model used to compute the interaction topology can change the prediction for the interaction cross section, leading to estimates of the flux that are substantially different. One of the theoretically cleanest interaction channels that is used for measuring the flux is quasielastic scattering, where an incident neutrino is converted to a charged lepton by interaction with a single nucleon. In the absence of re-interactions of the nucleon as it leaves the nucleus and assuming the hit nucleon was at rest initially, the energy of the neutrino is entirely determined by the momentum of the outgoing charged lepton via

$$E_\nu^{QE} = \frac{2\left(M_n - E_B\right)E_\mu - \left(\left(E_B - M_n\right)^2 - M_p^2 + m_\mu^2\right)}{2\left(M_n - E_B - E_\mu + |p_\mu|\cos\theta_\mu\right)}, \tag{1.10}$$

where E_B is the binding energy of the nucleon within the nucleus, M_n and M_p are the

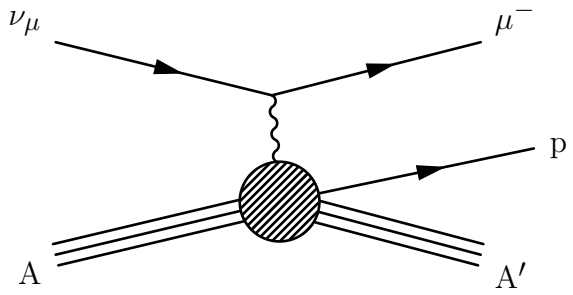

Figure 1.1: Feynman diagram for quasielastic scattering. The neutrino interacts with a nuclear target by imparting momentum to a single nucleon, leaving the rest of the nucleus intact. During the process, the neutrino is converted to a charged lepton via emission of a W boson.

neutron and proton mass, and E_μ, p_μ, and θ_μ are the energy, momentum, and angle of the outgoing charged lepton, respectively. Other event topologies can fake a signal by emitting some other particle in the initial neutrino interaction that is reabsorbed by the nucleus before it can escape. These events will also look like quasielastic scattering events, yet they will have the wrong kinematical distribution for the outgoing lepton.

For neutrino energy E_ν and a spacelike four-momentum transfer Q^2, the quasielastic cross section for a free-nucleon target is [3]

$$\frac{d\sigma_{CCQE}}{dQ^2} \propto \frac{1}{E_\nu^2}\left(A(Q^2) \mp \left(\frac{s-u}{M_N^2}\right) B(Q^2) + \left(\frac{s-u}{M_N^2}\right)^2 C(Q^2)\right), \tag{1.11}$$

where M_N is the nucleon mass and

$$s - u = 4M_N E_\nu - Q^2 - m_\ell^2 . \tag{1.12}$$

Defining $\eta \equiv \frac{Q^2}{4M_N^2}$, the factors A, B, and C are

$$A(Q^2) = \frac{m_\ell^2 + Q^2}{M_N^2} \times \left[(1+\eta)F_A^2 - (1-\eta)(F_1^2 + \eta F_2^2) + 4\eta F_1 F_2 - \frac{m_\ell^2}{4M_N^2}\left((F_1+F_2)^2 + (F_A+2F_P)^2 - 4(1+\eta)F_P^2\right)\right], \tag{1.13}$$

$$B(Q^2) = 4\eta F_A \left(F_1 + F_2\right), \tag{1.14}$$

and

$$C(Q^2) = \frac{1}{4}\left(F_A^2 + F_1^2 + \eta F_2^2\right). \tag{1.15}$$

The quasielastic cross section depends on four form factors: the vector form factors F_1 and F_2, the axial form factor F_A, and the pseudoscalar form factor F_P. The vector form factors are known from high-statistics, mono-energetic scattering data of electrons on a free nucleon target, and are precisely determined compared to the other form factors. The effects of the pseudoscalar form factor are suppressed by the lepton mass and are related to the axial form factor through the axial Ward identity,

$$\partial^\mu A_\mu^a(x) = 2\hat{m} P^a(x) \tag{1.16}$$

where $\hat{m}$ is the bare quark mass. For these reasons, the axial form factor is the most important systematic contribution to the free-nucleon cross section. This will be discussed in detail in Chapter 2.

1.1.3 Progress and Goals in Neutrino Oscillation

In recent years, the first measurements of neutrino oscillation parameters were completed. The mass-squared splittings and mixing angles have been determined by oscillation experi-

ments measuring a variety of channels, including both neutrino appearance and disappearance probabilities. The values of the mass-squared differences and mixing angles were measured by experiments to determine their values. To date, the values of Δm^2_{21}, Δm^2_{32}, and all of the mixing angles have been measured by experiments. The last mixing angle, θ_{13}, was only recently established to be nonzero at the Daya Bay experiment in Ref. [4]. This result ensures that a nonzero CP violation in the lepton sector is possible if δ_{CP} is nonzero. There is still more to do, with the CP violation and neutrino mass ordering still unknown.

In the following years, neutrino experiments will transition from discovery-based measurements of oscillation parameters to high-precision measurements of oscillation physics, filling in the two remaining unknowns. One of the flagship experiments is the Deep Underground Neutrino Experiment (DUNE) [5], which aims to unambiguously determine CP violation parameter δ_{CP} and the neutrino mass ordering by determining the sign of the mass-squared splitting Δm^2_{13}. To do this, DUNE will measure both the survival probability for ν_μ and the oscillation probability for $\nu_\mu \to \nu_e$, as well as the antineutrino counterpart to these probabilities. For neutrinos propagating through matter and to leading order, the effect has the form [6]

$$\begin{aligned} P(\overset{(-)}{\nu}_\mu \to \overset{(-)}{\nu}_e) = \sin^2\theta_{23}\sin^2 2\theta_{13}\frac{\sin^2(\Delta_{31}\mp aL)}{(\Delta_{31}\mp aL)^2}\Delta^2_{31} \\ + \sin 2\theta_{23}\sin 2\theta_{13}\sin 2\theta_{12}\frac{\sin(\Delta_{31}\mp aL)}{(\Delta_{31}\mp aL)^2}\Delta_{31}\frac{\sin(aL)}{aL}\Delta_{21}\cos(\Delta_{31}\pm\delta) \\ + \cos^2\theta_{23}\sin^2 2\theta_{12}\frac{\sin^2(aL)}{(aL)^2}\Delta^2_{21}\,, \end{aligned} \tag{1.17}$$

where the upper sign is for the neutrino probability, $\Delta_{ij} = \frac{\Delta m^2_{ij}L}{4E}$ and $a = G_F N_e/\sqrt{2}$, proportional to the Fermi constant G_F and the number density of electrons in the Earth, N_e. Since the effects of both the matter contribution and the CP violation change sign when changing from neutrinos to antineutrinos, the asymmetry between the two measurements gives a measurement of δ_{CP} and of the sign of Δm^2_{31}, which is necessary to determine the

	$\delta = 0$	$\delta = \pi/2$	$\delta = \pi$	$\delta = 3\pi/2$	observed
ν_e	24.2	19.6	24.1	28.7	32
$\overline{\nu}_e$	6.9	7.7	6.8	6.0	4

Table 1.1: Expected versus observed number of electron neutrino CC events in a recent T2K measurement, for a few values of δ_{CP} in the normal ordering. Reproduced from Ref. [8].

mass ordering. The effect becomes enhanced for large L, so the long baseline design for DUNE will be able to resolve these effects well.

To reach the precision goals set by DUNE, an equivalent improvement of the theory predictions of neutrino cross sections in nuclear matter is necessary. DUNE plans to use a 40-kiloton liquid argon time projection chamber to detect neutrino interaction events. The argon nucleus is not a small nuclear target and will have considerable nuclear effects. Without control of these nuclear effects, it will be challenging to precisely predict the expected number of events, complicating the extraction of PMNS oscillation parameters. This is apparent in a recent global fit to neutrino oscillation data in Ref. [7], that shows a hint that the CP violation in the lepton sector may be nonzero and maximal. This conclusion is mostly driven by the T2K measurement of ν_e appearance, which is summarized by Table 1.1. In this measurement, the number of ν_e appearance events observed is more than the number of events predicted by theory for all values of δ_{CP}. Taken at face value, one concludes that the data favor $\delta_{CP} = \frac{3\pi}{2}$. If the predictions continue to underestimate the number of events as the statistics are increased, this could indicate that the neutrino cross section has been underestimated. An enhancement of the neutrino cross section could bring the observed number of events into agreement with $\delta_{CP} = 0$, meaning that the original conclusion of $\delta_{CP} = \frac{3\pi}{2}$ was incorrect. Therefore, accurate predictions of the neutrino cross section are of the utmost importance for constraining δ_{CP} in the lepton sector.

1.2 Lattice QCD

1.2.1 Formalism

The quark action of QCD in the continuum is

$$S = \int d^4x\, \mathcal{L} = \int d^4x\, \overline{\psi}(x) \left(i\not{D} - m \right) \psi(x) \,. \tag{1.18}$$

The action is combined with a background field to create a generating functional,

$$Z[\eta, \overline{\eta}] = \int \mathcal{D}\psi \mathcal{D}\overline{\psi}\; e^{i \int d^4x \left(\mathcal{L} + \overline{\eta}\psi + \overline{\psi}\eta \right)} \,. \tag{1.19}$$

Expectation values are then computed from applying derivatives to the generating functional

$$\langle \psi(x) \overline{\psi}(y) \rangle = Z[\eta, \overline{\eta}]^{-1} \left(-i \frac{\delta}{\delta \overline{\eta}(x)} \right) \left(-i \frac{\delta}{\delta \eta(y)} \right) Z[\eta, \overline{\eta}] \,, \tag{1.20}$$

which is reminiscent of a partition function from statistical mechanics. Feynman showed that the Green's functions in quantum field theory may be recast into a partition function of a Euclidean action by applying a Wick rotation $t \to -ix_4$. The action is transformed into its Euclidean equivalent

$$iS_E = i \int d^4x\, \mathcal{L}_E = i \int d^4x\, \overline{\psi}(x) \left(\not{D} + m \right) \psi(x) \,. \tag{1.21}$$

The degrees of freedom of the theory must be made finite to compute correlation functions of observables on the lattice. This is done by discretizing spacetime and defining the quark fields on the sites of a lattice with lattice spacing a and confining the theory to a box of size $L = N \cdot a$. To preserve gauge invariance, this requires that the gauge fields be defined on the links between sites, defined by Wilson lines in the form

$$U_\mu(x) = e^{ig \sum_b \lambda^b \int_x^{x + a\hat{\mu}} A_\mu^b(y) dy} \,, \tag{1.22}$$

where g is the bare coupling constant of the strong force, λ^b are the generators of the $SU(3)$ color symmetry, and $A^b_\mu(y)$ is the gluon field. The links U_μ take the form of $SU(3)$ matrices in lattice QCD calculations. Then gauge transformations on the quark and gluon fields may be written as

$$\psi(x) \to V(x)\psi(x) \tag{1.23}$$

and

$$U_\mu(x) \to V(x)U_\mu(x)V^\dagger(x + a\hat{\mu}) \tag{1.24}$$

for an $SU(3)$ gauge transformation matrix V. Gauge invariant quantities may be constructed by constructing loops from links, or by capping chains of gauge links with quark and anti-quark fields.

The derivative in the action of Eq. (1.21) must also be discretized to make the action amenable to lattice QCD. The first guess would be to use the finite difference

$$\frac{d}{dx_\mu}\psi(x) \to \frac{1}{a}\left[\psi(x + a\hat{\mu}) - \psi(x)\right] . \tag{1.25}$$

This operator does not preserve the Hermiticity of the derivative operator though. Instead, one must define a lattice derivative

$$i\frac{d}{dx_\mu}\psi(x) \to \frac{i}{2a}\left[\psi(x + a\hat{\mu}) - \psi(x - a\hat{\mu})\right] , \tag{1.26}$$

involving a finite difference in both directions about site x. To make this derivative covariant under gauge transformations, the gauge links must be added to form the operator

$$iD_\mu\psi(x) \to \frac{i}{2a}\left[U_\mu(x)\psi(x + a\hat{\mu}) - U^\dagger_\mu(x - a\hat{\mu})\psi(x - a\hat{\mu})\right] . \tag{1.27}$$

These fixes are enough to construct the lattice QCD action for the quark fields. After

replacing the integral over Euclidean spacetime with a sum, the action becomes

$$\begin{aligned} iS_E =& ia^4 \sum_x \left[\frac{1}{2a} \sum_\mu \overline{\psi}(x)\gamma_\mu \left[U_\mu(x)\psi(x+a\hat{\mu}) - U_\mu^\dagger(x-a\hat{\mu})\psi(x-a\hat{\mu}) \right] \right. \\ & \left. + \, m\overline{\psi}(x)\psi(x) \right]. \end{aligned} \tag{1.28}$$

The lattice spacing still shows up in this expression. To make the action fully dimensionless, the spacing a is absorbed into the definitions of the quark fields,

$$a^{3/2}\psi(x) \to \psi(x)\,. \tag{1.29}$$

Then the action is fully reduced to the naive lattice action, of the form

$$\begin{aligned} iS_{\text{lat}} =& i \sum_x \left[\frac{1}{2} \sum_\mu \overline{\psi}(x)\gamma_\mu \left[U_\mu(x)\psi(x+\hat{\mu}) - U_\mu^\dagger(x-\hat{\mu})\psi(x-\hat{\mu}) \right] \right. \\ & \left. + \, am\,\overline{\psi}(x)\psi(x) \right]. \end{aligned} \tag{1.30}$$

Using this action, observables may be computed in terms of the partition function. Taking Eqs. (1.19) and (1.20) as a guide, a general observable may be computed with the equation

$$\langle \mathcal{O} \rangle = \frac{1}{Z_0} \int \mathcal{D}U\mathcal{D}\psi\mathcal{D}\overline{\psi}\; \mathcal{O}\, e^{-S_{\text{lat}}}\,, \tag{1.31}$$

which reduces to

$$\langle \mathcal{O} \rangle = \frac{1}{\text{Tr}\left[e^{-HT}\right]} \text{Tr}\left[\mathcal{O}e^{-HT}\right] \tag{1.32}$$

where T is the length of the lattice in the temporal direction and H is the Hamiltonian.

1.2.2 Doubling Symmetry and Summary of Lattice Actions

One of the consequences of discretizing spacetime is the introduction of unwanted extra species of quarks, usually known as doublers. The number of doublers is 2^D, where D is

the number of spacetime dimensions, and are referred to as quark "tastes". The existence of the doublers is intimately tied with chiral symmetry. Nielsen and Niyomiya proved a no-go theorem [9] stating that it is not possible to have a doubler-free field theory in lattice QCD that preserves chiral symmetry. The ramifications of this discovery add the intricacies that make lattice QCD such a widely studied field.

To obtain results that accurately pertain to physical field theories, it is necessary to remove the contributions of these extra doublers from the calculations of observables. There are a variety of methods for achieving this goal, all with their own set of advantages and disadvantages that depend on the problem being studied. Some methods, such as Wilson (or clover) quarks, break chiral symmetry explicitly to give the doublers a mass term of order $\mathcal{O}(a^{-1})$, where a is the lattice spacing, such that they decouple in the continuum limit. Other methods choose to preserve chiral symmetry in the continuum limit at the expense of more costly computing times, such as domain wall fermions. The method of choice in this thesis is to use staggered fermions, which remove only a factor of four doublers (leaving four remnant tastes), with the benefit of improved computation time. This extra computing time can then be used to perform higher statistics simulations, with physical quark masses, more ensembles, and finer lattice spacings than other methods.

One concern with staggered quarks is that the four extra tastes contribute to observables through virtual quark-antiquark pairs (or "sea" quarks) that interact with the "valence" quarks that are explicitly introduced into the computation. Written in terms of the path integral, the virtual quark-antiquark pairs appear as the determinant after integrating out the quark fields:

$$\langle \mathcal{O} \rangle = \frac{1}{Z} \int \mathcal{D}U \, \mathcal{O} \det \left[\not{D} + m \right] e^{-S[U]} \, . \tag{1.33}$$

Since there are more quarks tastes interacting with the valence quarks than the continuum theory, the calculation results will differ from their physical values unless the extra tastes

are removed. The simple remedy to this problem is to take a fourth root of the determinant,

$$\det\left[\not{D}+m\right] \to \left(\det\left[\not{D}+m\right]\right)^{\frac{1}{4}} . \tag{1.34}$$

This is called the "rooting" trick. This is based on the observation that the tastes are degenerate in the continuum limit, and so the fermion determinant can be rewritten as

$$\det\left[\not{D}_4+m\right] = \det\left[\left(\not{D}_1+m\right)\otimes \mathbb{1}_4\right] = \left(\det\left[\left(\not{D}_1+m\right)\right]\right)^4 , \tag{1.35}$$

where $\not{D}_n$ is the fermion derivative for n tastes.

The rooting procedure still depends on whether the continuum limit commutes with the fourth root. If taste symmetry is broken at finite lattice spacing, then it is possible that the taste breaking effects spoil the continuum limit. While the former is true, it does not necessarily imply the latter and the latter does not seem to be an issue. This was tested in Ref. [10] using a method of rooted staggered chiral perturbation theory developed in Ref. [11]. This method was used to compute observables that are sensitive to the number of quarks in the sea as a means to test the number of replicas, i.e. the number of tastes of quarks in the sea. If the rooting trick is valid, then the number of replicas per staggered flavor n_r, which was treated as a fit variable, should be equal to $\frac{1}{4}$. The result of this study was $n_r = 0.28(2)(3)$, in good agreement with expectation. This test is reassuring, although not a proof of the validity of the procedure. Despite this, other criticisms raised about the rooting procedure were found to be harmless (see Ref. [12] for a summary of these arguments).

1.3 Success of Lattice QCD

Lattice QCD calculations of nucleon physics today are at the same level of precision that meson calculations were a decade ago. As computers become more powerful and computational strategies are refined, it will be possible to probe more physics and with greater

precision. Lattice QCD computations are systematically improvable, since better precision can be achieved by running more computations.

The success of lattice QCD makes it an appealing tool to help inform neutrino physics. The matrix elements needed for predicting neutrino cross sections are often difficult to probe with scattering experiments. With lattice QCD, these matrix elements can be computed directly from first principles. Lattice QCD can fill in gaps left by experiments or serve as a check of the values obtained from experimental measurements.

1.3.1 Lattice QCD for Spectrum Computations and CKM Matrix Elements

Lattice QCD is a first-principles computation, not a simulation like the Monte Carlo generators that are widely used in neutrino physics. The gauge ensembles are generated from only the bare quark masses and the strong coupling constant, and an equal number of inputs from experiment are necessary to connect lattice QCD measurements to the physical theory. These inputs are typically taken from observables that are precisely determined and independent of the physics that is being studied. Once the scale is set in this way, any other observables computed with lattice QCD are predictions from theory.

Not only is lattice QCD theoretically robust, but the computations of observables with lattice QCD are both consistent with each other and with experiment. A compilation of computations from lattice QCD and the experimental measurements of hadron masses is shown in Fig. 1.2. The measurements in this figure come from several collaborations and make use of a variety of lattice QCD actions to compute the spectrum. Open symbols indicate observables that were used to fix the scale and bare quark masses, and closed symbols indicate the results for computed observables.

The results from lattice QCD are useful for studying the CKM matrix in flavor physics. Determinations of the CKM matrix elements from particle decays get contributions from both the CKM matrix elements and from form factors. Since experiments have difficulty determining form factor contributions to the observed decays, they rely on theory to compute

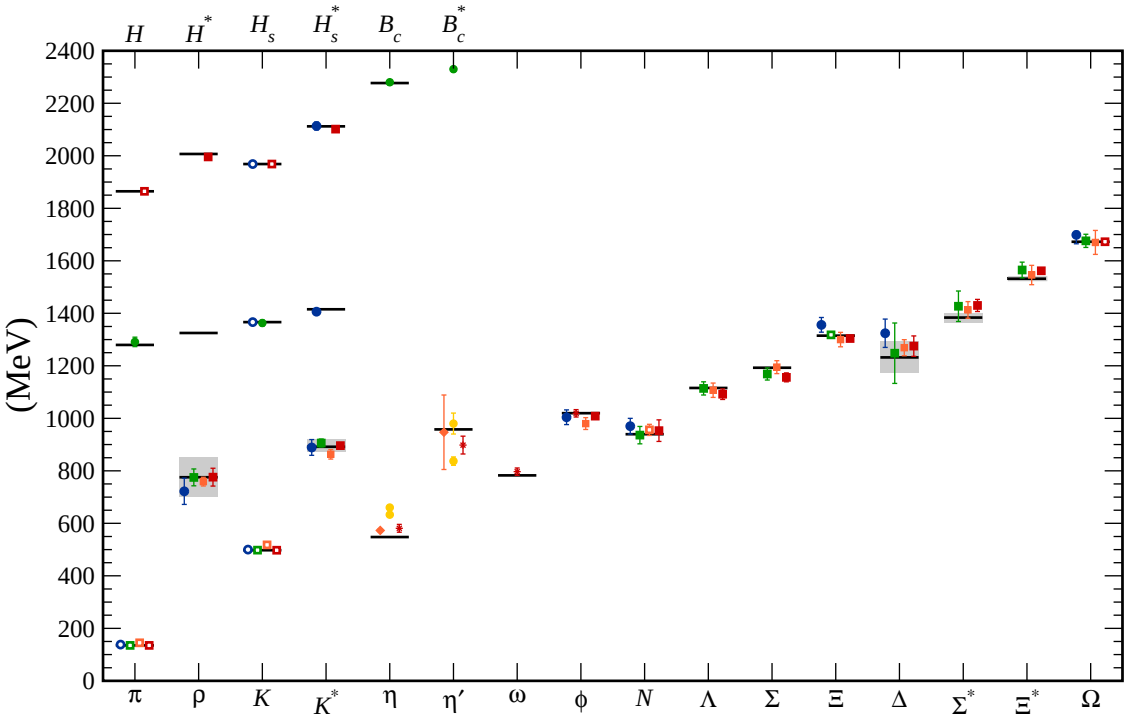

Figure 1.2: Figure showing the mass spectrum for the mesons and baryons computed with lattice QCD by various collaborations. Masses from experiment are shown as black lines with gray boxes to indicate widths. The colors indicate how many ensembles were used in the measurement, where the colors red, orange, yellow, green, and blue are ordered from fewest to most. The symbol shapes denote the type of lattice QCD action used. Open symbols denote values that were used to fix the parameters in the computation. Closed symbols are results. The meson masses that include b quarks are offset downward by 4 GeV. Reproduced from Ref. [13].

the form factor contributions. Lattice QCD offers the only systematically improvable method of computing the form factor contributions. As a result, results from lattice QCD are widely used by the flavor physics community, for instance in the extraction of $|V_{ub}/V_{cb}|$ by the LHCb collaboration [14]. Using the results of lattice QCD, the first row of the CKM matrix are known to sub-percent accuracy from experiment, and elements from the second row are known to few-percent accuracy from lattice QCD [15].

Determinations of the CKM matrix elements have also served as a proving ground for the z expansion parameterization of form factors, which will be covered in more detail in Chapter 2. The z expansion is a model-independent framework based on constraints from analyticity. Using the z expansion, lattice QCD data at high momentum transfer could be

used to perform a controlled extrapolation down into the region of low momentum transfer where experiment is most constraining. Recent results for meson decays [16, 17] as well as those for baryon decays mentioned above [18] determine the CKM matrix elements $|V_{ub}|$ and $|V_{cb}|$ precisely with the z expansion, showing how powerful the strategy can be. A similar transition of the neutrino community to the z expansion is also necessary. The z expansion has now been implemented into the GENIE Monte Carlo framework to facilitate the use of the z expansion by neutrino experiments; see Sec. 2.3 for details.

As lattice QCD computations of nucleon form factors become more precise and better controlled, the neutrino community should incorporate the form factors from lattice QCD into their analyses. Lattice QCD offers a way to access matrix elements that are difficult for neutrino physics to determine experimentally. The axial form factor is one specific example of a matrix element that is useful to compute from first principles. Since this matrix element is only accessible through neutrino interactions, lattice QCD can be applied both as a check of the form factor extracted from experiment and as an experiment-free determination of the form factor to build a theory upon. Since the axial charge is an integral part of the axial form factor, the work of this thesis focuses on the axial charge. Later extensions of this work will compute the full momentum dependence of the axial form factor.

1.3.2 The Nucleon Axial Charge in Lattice QCD

Computing the axial charge with lattice QCD has proved to be a formidable challenge in the past. Many computations of the axial charge have been attempted, and yet the axial charge has typically come out $10 - 20\%$ too small. Reproduction of the experimental value for the axial charge has become a litmus test for control of systematic effects.

Computation of nucleon matrix elements is difficult from a theoretical standpoint. As will be discussed in Chapter 4, baryon correlation functions computed with lattice QCD suffer from an exponential signal-to-noise degradation due to a three-pion contribution to the statistical noise. The nucleon is much larger than the pion, meaning that correlation

functions are sensitive to the size of the lattice ensemble due to pions that wrap around through the periodic boundary conditions. Excited states can also be a contributing factor, since the second-lowest nucleon excited state in the same-parity channel is much lower than other radial excitations.

Past computations of the axial charge have been limited by how well the systematics could be controlled. Due to restrictions imposed by the amount of computing resources available, computations needed to be computed at unphysically large pion masses and with small lattice spatial boxes. Measurements of the axial charge needed to be done for a range of pion masses and extrapolated to physical masses and infinite volume. These restrictions have made controlling systematic finite size corrections difficult, since these corrections depend

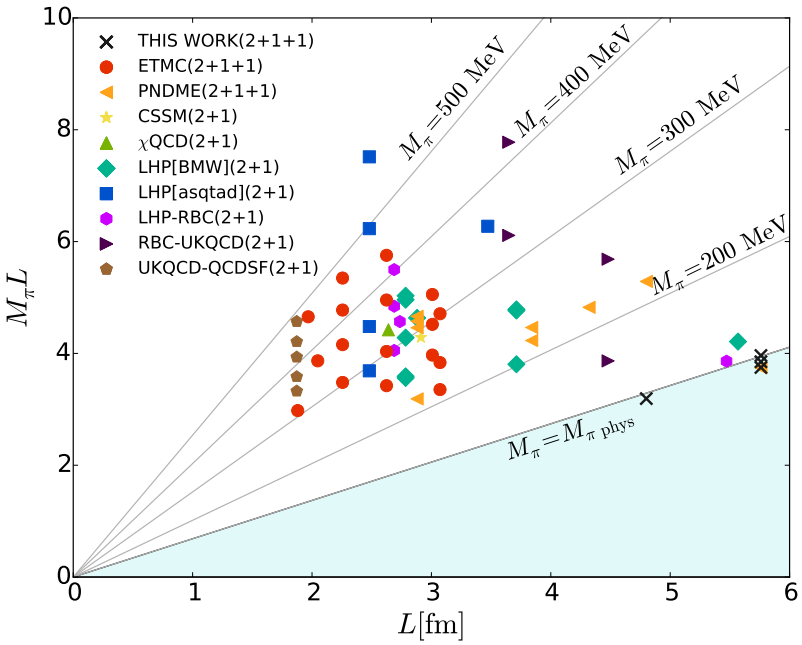

Figure 1.3: Plot of lattice spatial extent versus physical box size for lattice QCD computations of g_A with at least 3 flavors of sea quarks. The physical box size is given in dimensionless units of $M_\pi L$, which is an estimate of how easily pions can propagate around the periodic boundary conditions. Lines of constant M_π are plotted, and the region of $M_\pi < M_\pi^{\mathrm{phys}}$ (bottom right) is shaded. Ideally, calculations should have masses as close to the physical line and as far in the vertical direction as possible. The ensemble for this work is the $\times$ plotted at $L \approx 5$ fm along the line denoting physical pion mass, and future extensions of this work will use the ensembles at $L \approx 6$ fm. Computations from Refs. [20–32].

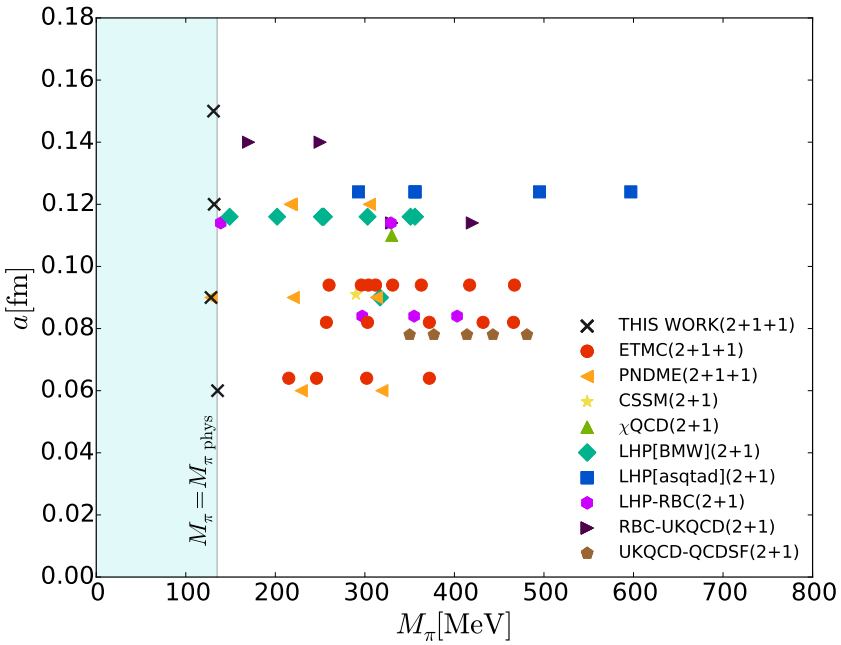

Figure 1.4: Plot of pion mass versus lattice spacing for lattice QCD computations of g_A with at least 3 flavors of sea quarks. The region of $M_\pi < M_\pi^{\mathrm{phys}}$ (left) is shaded. The horizontal axis is the pion mass, in MeV, and the vertical mass is the lattice spacing, in units of 10^{-15} m. Ideally, calculations should be as close to physical pion mass and for the smallest lattice spacing possible. The ensemble used in this plot is the $\times$ plotted at $a = 0.15$ fm, and future extensions of this work will use the ensembles at $a = 0.12$, 0.09, and 0.06 fm. Computations from Refs. [20–32].

on both the spatial volume and the pion mass. A survey of past calculations of the axial charge is given in Figs. 1.3 and 1.4. These two plots give an idea of how large of a body of work has been done to compute the axial charge.

Now, ensembles generated with physical pion masses are available, making it possible for the first time to do a computation of the axial charge at the physical point. Systematic effects of nucleon matrix elements are better understood and simulations with full systematic error budgets are possible. A measurement of the nucleon vector form factors with controlled systematic errors has already been completed near the physical point in Ref. [33]. Additionally, a recent paper [34] shows agreement between a new lattice QCD computation of g_A and the experimental value. Even with one value in agreement with experiment, cross

checks are necessary for giving confidence in lattice QCD results.

The work presented in this thesis represents a first step in a program to compute the axial form factor with lattice QCD. The nucleon axial form factor is studied by reanalyzing deuterium bubble chamber data with the z expansion parametrization to determine the present uncertainty on the free-nucleon cross section from the most theoretically clean data available. Following this, the results of a computation of the nucleon spectrum and axial charge using staggered lattice QCD are detailed.

CHAPTER 2

THE AXIAL FORM FACTOR FROM NEUTRINO SCATTERING DATA

The axial form factor contributes the largest systematic uncertainty to the quasielastic scattering cross section. Direct experimental determinations of the form factor are sparse, since only the weak current probes the axial form factor. Experiments that constrain the form factor are limited to low-statistics neutrino scattering experiments on small nuclear targets, scattering data with large nuclear targets and significant nuclear effects, or determinations from pion electroproduction with model-dependent corrections.

The dipole model was introduced by Llewellyn-Smith [35] as an ansatz to explain neutrino quasielastic scattering data, and is the most ubiquitous parametrization for the axial form factor. The dipole axial form factor is

$$F_A^{\mathrm{dpl}}(Q^2) = g_A \left(1 + \frac{Q^2}{m_A^2}\right)^{-2} \tag{2.1}$$

where g_A is the axial charge and m_A is a free model parameter, the axial mass. The axial charge is determined precisely from neutron beta decay experiments, with the value $g_A = -1.2723(23)$ from Ref. [36]. A motivation for the model comes from assuming an exponential falloff in a nonrelativistic charge distribution for the nucleon wavefunction with distance, which yields a dipole form factor when a Fourier transform is applied. The dipole model reproduces the power law scaling that is expected from perturbative QCD, but this scaling takes effect well outside of the window where neutrino scattering data are collected. There is no reason to expect that a model fit to data well below the perturbative region will be an accurate description of the physics at high momentum transfer.

The comparison of the world average dipole mass [37] with the MiniBooNE extraction of m_A [38] shows how adherence to the dipole model introduces ambiguities. For example,

some representative values of the axial mass are

$$\begin{aligned} m_A &= 1.069 \pm 0.016 \text{ GeV} && \text{Ref. [37]}, \\ m_A^{\text{eff}} &= 1.35 \pm 0.17 \text{ GeV} && \text{Ref. [38]}. \end{aligned} \tag{2.2}$$

The extracted m_A is either accompanied by an unphysically small error, as in the former value, or entangles the extraction of the free nucleon form factor with the nuclear corrections used to determine it, as in the latter case. Disagreement in the central values of m_A indicate shortcomings in Eq. (2.1), suggesting that it leads to underestimated uncertainties, and attempts to compare different regions of Q^2 will be incompatible.

This chapter covers a model-independent parametrization, the z expansion. Whereas the dipole assumes a particular shape with a single characteristic, the z expansion is more flexible. Term-by-term it can accommodate any shape, and addition of more precise information will constrain the expansion parameters a systematic way. The first section covers the details of the z expansion and the advantages conferred by using such a framework. The following section details an extraction of the best z expansion parameters implied by deuterium bubble chamber data, along with a full error budget. Finally, some details are given about the implementation of the z expansion as a module in a neutrino Monte Carlo event generator, GENIE.

2.1 The z Expansion Parameterization

The z expansion is a model-independent approach for parameterizing hadronic form factors, appealing only to constraints from analyticity imposed by QCD. This method makes use of analytic continuation and a conformal mapping to reparametrize the form factor as a power series in a small expansion parameter. As the data improve, the expansion is systematically improvable by carrying out the expansion to a higher power.

For concreteness, we will focus on the z expansion as it pertains to the nucleon axial

form factor. The form factor is written as a function of the Lorentz invariant 4-momentum transfer, Q^2. There are two regions of interest. The first is the particle production region corresponding to timelike Q^2, starting at $Q^2 = -9m_\pi^2$ and extending to $Q^2 \to -\infty$. The second is the spacelike quasielastic scattering region, extending from $Q^2 = 0$ up to some finite $Q^2_{\rm max}$ determined by the experiment of interest.

The form factor is analytic outside the branch cut and may be parametrized by applying the mapping (for $t = -Q^2$)

$$z(t; t_0, t_+) = \frac{\sqrt{t_+ - t} - \sqrt{t_+ - t_0}}{\sqrt{t_+ - t} + \sqrt{t_+ - t_0}}\,, \tag{2.3}$$

where $t_+ = 9m_\pi^2$ is the particle production threshold. t_0 is an unphysical parameter that corresponds to $z(t_0) = 0$ and is typically chosen to minimize $|z(t)|$ in the range of t under consideration [39]. The optimal choice of t_0 for a choice of $Q^2_{\rm max}$ is

$$t_0^{\rm opt}(Q^2_{\rm max}) = t_+ \left(1 - \sqrt{1 + Q^2_{\rm max}/t_+}\right)\,. \tag{2.4}$$

Under the chosen mapping in Eq. (2.3), the parameter $|z(-Q^2)| < 1$, so the form factor can be written as a power series with the small expansion parameter z,

$$F_A(Q^2) = \sum_{k=0}^{\infty} a_k z^k(-Q^2)\,. \tag{2.5}$$

Fall off of the form factor and the finiteness of $\sum_k |a_k|^2$ require that the z expansion coefficients a_k in Eq. (2.5) be not only bounded, but also decreasing [39]. As a result, the power series is convergent within $|z| < 1$ and expansion terms of a sufficiently high order contribute negligibly to the value of the form factor within the fit region $0 < Q^2 < Q^2_{\rm max}$. The form factor may therefore be truncated at some finite order $k_{\rm max}$ without introducing a large truncation error. If new and better information comes along, the maximum power can be increased to keep the truncation error negligible.

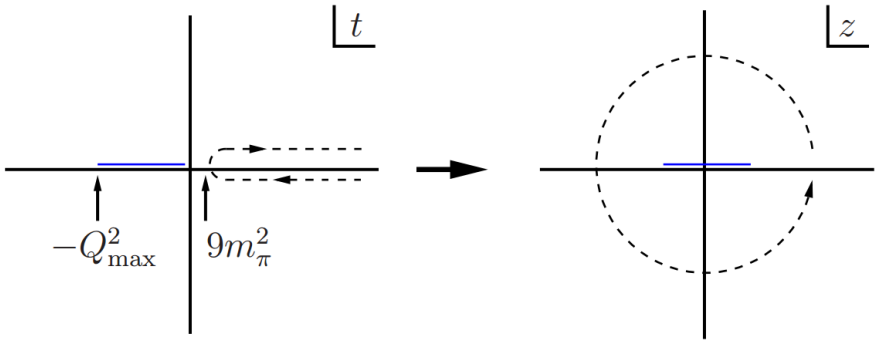

Figure 2.1: A diagram depicting the conformal mapping of the form factor from complex Q^2 space to z parameter space. There are two regions of interest: first, the branch cut corresponding to particle production that starts at the three-pion production threshold at $t = 9m_\pi^2$ and continues to $t \to \infty$, and second, the quasielastic region (blue line segment) for $-Q^2_{\rm max} < t < 0$. After applying the z expansion conformal mapping, the quasielastic region is mapped to within $|z| < 1$, meaning that the form factor can be expanded as a power series in z. Figure adapted from Ref. [39].

The coefficient bounds are better understood by imposing an ansatz for the form factor shape, following the argument in Ref. [39]. In an "axial-vector dominance" ansatz, the form factor takes a Breit-Wigner form

$$F_A \sim \frac{m_{a_1}^2}{m_{a_1}^2 - t - i\Gamma_{a_1} m_{a_1}} \equiv -\frac{m_{a_1}^2}{b(t)} \,. \tag{2.6}$$

This is recovered by assuming

$$\mathrm{Im}F_A(t + i0) = \frac{\mathcal{N} m_{a_1}^3 \Gamma_{a_1}}{|b(t)|^2} \theta(t - t_+) \tag{2.7}$$

and applying the dispersion relation

$$F_A(t) = \frac{1}{\pi} \int_{t_+}^{\infty} \frac{\mathrm{Im}F_A(t' + i0)}{t' - t} \,. \tag{2.8}$$

The normalization $\mathcal{N}$ is determined by computing $F_A(t)$ and setting $t = 0$. One can then

define norms

$$
\begin{aligned}
||F_A||_p &\equiv \left(\sum_k |a_k|^p\right)^{\frac{1}{p}} , \\
||F_A||_2 &= \left(\sum_k |a_k|^2\right)^{\frac{1}{2}} = \left(\oint \frac{dz}{z}|F_A|^2\right)^{\frac{1}{2}} , \\
||F_A||_\infty &= \lim_{p\to\infty}\left(\sum_k |a_k|^p\right)^{\frac{1}{p}} \to \max\{|a_k|\} ,
\end{aligned} \tag{2.9}
$$

to find that $||F_A||_\infty \leq ||F_A||_2$, which is only possible if $|a_k|$ falls off as k increases. One can then use the definition of $||F_A||_\infty$ to determine the condition

$$
\left|\frac{a_k}{a_0}\right| \leq \frac{2|\mathcal{N}|}{|F_A(t_0)|}\mathrm{Im}\left(\frac{-m_{a_1}^2}{b(t_+)+\sqrt{(t_+-t_0)b(t_+)}}\right) \tag{2.10}
$$

for all k. Substitution of explicit values for the parameters yields a bound for the maximum relative parameter size.

Outside of the fit region, one may exert additional control over the form factor shape by applying sum rules to constrain the expansion coefficients a_k. We may use the sum rules to satisfy arguments from perturbative QCD in Ref. [40] that require the axial form factor exhibit a Q^{-4} power law behavior as $Q^2 \to \infty$. Other sum rules may be derived from this one by applying chain rule to derivatives $\left(\frac{d}{dz}\right)^n F_A(z)\big|_{z\to 1}$ and inverting Eq. (2.3) to get $\frac{dt}{dz}$. These restrictions are encoded into the sum rules

$$
\sum_{k=n}^{\infty} k(k-1)\ldots(k-n+1)a_k = 0 \quad (n \in 0,1,2,3) \tag{2.11}
$$

where $a_k = 0$ for $k > k_{\max}$. We may derive these relations by noting that $z(-Q^2) = 1$ at $Q^2 \to \infty$, and so

$$
\sum_{k=0}^{\infty} a_k = F_A\left(z(-Q^2)\right)\Big|_{z\to 1} \propto Q^{-4} . \tag{2.12}
$$

2.2 Reanalysis of Neutrino Scattering Data in Deuterium Bubble Chambers

In Ref. [41], we apply the z expansion axial form factor to data from neutrino scattering in deuterium bubble chambers. Because the z expansion is model-independent, we obtain in this way a realistic estimate of the uncertainty on the axial form factor. Despite the existence of many modern neutrino scattering experiments, the deuterium bubble chamber studies have small nuclear targets and, thus, remain the most theoretically clean samples available to date. The deuterium nucleus is a weakly bound state of two nucleons such that each nucleon can be treated as approximately free, making it a good probe of free nucleon amplitudes. Quasielastic scattering events with sufficient energies in these samples have two protons in the final state, which may both be detected to better constrain the energies of the particles involved in the collisions.

Data from three experiments are used in this analysis: the BNL 7-foot bubble chamber [42], the ANL 12-foot bubble chamber [43–45], and the FNAL 15-foot bubble chamber experiment [46]. We refer to these experiments as BNL1981, ANL1982, and FNAL1983, respectively. The data are taken for energies at around 1 GeV for BNL1981 and ANL1982, and around 10 GeV for FNAL1983, and all three experiments have around one thousand events. Unfortunately, the event-level data for these experiments have been lost, so the data were extracted by digitizing figures in the references. Agreement between the number of digitized events and the number of events reported in the publications was found.

2.2.1 Fitting Procedure and Default Inputs

We fit to the momentum transfer event distributions, $\frac{dN^D}{dQ^2}(Q^2)$, which were presented in the references. The superscript D indicates that this distribution refers to a deuteron target, distinct from the event distribution on a free nucleon target, which will be denoted with a superscript N. The events in these distributions were created by neutrino beams with a

range of energies, described by a flux as a function of the neutrino energy, $\Phi(E_\nu)$. Predictions for the number distribution came from convolving the differential neutrino flux $\frac{d\Phi}{dE_\nu}$ with the differential cross section of the deuteron given by

$$\left(\frac{dN^D}{dQ^2}\right)^{\text{theory}} = \mathcal{N}_{\text{fit}} \int_0^\infty dE_\nu \frac{d\Phi}{dE_\nu}(E_\nu, F_A) \frac{d\sigma^D}{dQ^2}(Q^2, E_\nu, F_A)\,, \tag{2.13}$$

where the differential flux comes from measuring an event distribution in energy,

$$\frac{d\Phi}{dE_\nu}(E_\nu, F_A) = \frac{1}{\sigma(E_\nu, F_A)} \frac{dN}{dE_\nu}(E_\nu)\,. \tag{2.14}$$

We normalize the energy distributions by restricting

$$\int_0^\infty \frac{dN^N}{dE_\nu}(E_\nu, F_A)\, dE_\nu = \mathcal{N} \int_{Q^2_{\text{min}}}^\infty \frac{dN^D}{dQ^2}(Q^2, F_A)\, dQ^2\,, \tag{2.15}$$

where Eq. (2.15) is consistent when we set

$$\mathcal{N} = \frac{\int_0^\infty dQ^2 \frac{dN^N}{dQ^2}}{\int_{Q^2_{\text{min}}}^\infty dQ^2 \frac{dN^D}{dQ^2}}\,. \tag{2.16}$$

To prevent computation of the integrals in Eq. (2.16) during fitting, the normalization factor $\mathcal{N}_{\text{fit}}$ is allowed to float freely and is fit. The resulting $\mathcal{N}_{\text{fit}}$ may be compared with the prediction from Eq. (2.16) to check for consistency.

The deuteron differential cross section was determined by applying a correction, which was assumed to be energy-independent, to the free nucleon differential cross section according to the prescription

$$\frac{d\sigma^D}{dQ^2}(Q^2, E_\nu) = R(Q^2) \frac{d\sigma^N}{dQ^2}(Q^2, E_\nu)\,. \tag{2.17}$$

For our default choice of deuteron correction, $R(Q^2)$ was taken from Ref. [47]. The flux distribution $\frac{d\Phi}{dE_\nu}$ was determined from the event energy distribution reported in the literature

Input	Value	Reference
$g_A = F_A(0)$	-1.2723	[36]
$\mu_p - \mu_n - 1$	3.7058	[36]
F_{Vi}	BBA2005	[48]
F_P	PCAC	Eq. (2.19)
Deuteron correction	Singh	[47]

Table 2.1: Our default inputs used in fits to deuterium bubble chamber data.

normalized by the total cross section,

$$\frac{d\Phi}{dE_\nu}(E_\nu, F_A) \propto \frac{1}{\sigma^N(E_\nu, F_A)} \frac{dN^N}{dE_\nu}(E_\nu)\,. \tag{2.18}$$

To prevent artifacts from discrete jumps in the neutrino flux, the flux was smoothed with a spline smoothing algorithm to bin the flux more finely. The cross section in the denominator was computed with F_A held fixed for a single fit, then the form factor was updated and the fit recomputed. This process is iterated until the result converges.

Our default choice of fit inputs is listed in Table 2.1. We used the nucleon mass $m_N = 0.9389$ GeV, the pion mass $m_\pi = 0.14$ GeV, and the muon mass $m_\mu = 0.1057$ GeV. The value of the form factor normalization g_A is well-known from neutron beta decay experiments and is fixed within the fits [36]. We made use of a soft pion theorem derived from the Partially Conserved Axial Current (PCAC) to describe the pseudoscalar current, given by

$$F_P^{\mathrm{PCAC}}(Q^2) = \frac{2m_N^2 F_A(Q^2)}{m_\pi^2 + Q^2}\,. \tag{2.19}$$

Equation 2.18 holds as $Q^2 \to 0$ and is an ansatz for $Q^2 > 0$. In our mapping to z parameter space in Eq. (2.3), we chose to optimize our form factor parameterization in the $Q^2 < 1.0$ GeV^2 range with $t_0 = -0.28$ GeV$^2 = t_0^{\mathrm{opt}}(1.0\ \mathrm{GeV}^2)$. Over the range of data considered in our fits, this corresponds to $|z|^k_{\mathrm{max}}$ entering at the $20\%, 9\%, 4\%$ level for $k = 2, 3, 4$, respectively.

Input	BNL1981	ANL1982	FNAL1983
Q^2 range	$0.06 - 3\,\mathrm{GeV}^2$	$0.05 - 2.5\,\mathrm{GeV}^2$	$0 - 3\,\mathrm{GeV}^2$
N_{bins}	49	49	30
N_{events}	1236	1792	354
kinematic cut	$Q^2 \geq 0.06\,\mathrm{GeV}^2$	$Q^2 \geq 0.05\,\mathrm{GeV}^2$	$Q^2 \geq 0.10\,\mathrm{GeV}^2$

Table 2.2: Summary of data and cuts from original publications, BNL1981 [42], ANL1982 [45], and FNAL1983 [46]. The default choice for our fits replicates these numbers.

Our fits were done using a binned log-likelihood function, minimizing the quantity

$$-2\log\left[\mathcal{L}(F_A)\right] = 2\sum_i \left[\mu_i(F_A) - n_i + n_i \log\left(\frac{n_i}{\mu_i(F_A)}\right)\right] , \tag{2.20}$$

where n_i is the data in bin i and $\mu_i(F_A)$ is the prediction as a function of our choice of form factor. To indicate goodness of fit, we reported the value of the binned likelihood (with the shorthand -2LL) and the number of data points used in the fits. Our final fit employed a χ^2 function, defined by

$$\chi^2(F_A) = \sum_i \left(\frac{n_i - \mu_i(F_A)}{\sigma_i}\right)^2 , \tag{2.21}$$

where σ_i is the error on bin i.

It was shown in Ref. [49] that the z expansion coefficients fall off as $a_k \sim k^{-4}$ for large k. We use this as a guide for implementing Gaussian priors on z expansion coefficients to prevent them from becoming unphysically large. We chose a milder dependence on k to prevent overconstraining parameters, summarized by the constraints

$$\left|\frac{a_k}{a_0}\right| < \min\left(5, \frac{25}{k}\right) . \tag{2.22}$$

We avoided using the axial mass m_A to compare fits because it is defined only in the context of the dipole model, not as a model-independent quantity. We instead compared fits by computing the slope at some choice of Q^2, which is an observable quantity. This slope at $Q^2 = 0$ is related to the axial radius, which is obtained from Taylor expanding the axial

		Dipole			$N_a = 3$		
Experiment	$N_{\rm bins}$	-2LL	$\mathcal{N}_{\rm fit}$	r_A^2 [fm^2]	-2LL	$\mathcal{N}_{\rm fit}$	r_A^2 [fm^2]
BNL1981	49	70.9	$1.14^{+0.08}_{-0.07}$	0.424(44)	76.1	$1.14^{+0.12}_{-0.11}$	0.36(21)
ANL1982	49	58.6	$1.15^{+0.06}_{-0.06}$	0.444(44)	62.3	$1.15^{+0.10}_{-0.09}$	0.38(19)
FNAL1983	29	38.2	$1.17^{+0.16}_{-0.13}$	0.337(61)	39.1	$1.21^{+0.24}_{-0.20}$	0.61(28)
		$N_a = 4$			$N_a = 5$		
Experiment	$N_{\rm bins}$	-2LL	$\mathcal{N}_{\rm fit}$	r_A^2 [fm^2]	-2LL	$\mathcal{N}_{\rm fit}$	r_A^2 [fm^2]
BNL1981	49	73.4	$1.13^{+0.13}_{-0.11}$	0.25(21)	71.0	$1.13^{+0.13}_{-0.12}$	0.18(21)
ANL1982	49	60.9	$1.14^{+0.10}_{-0.10}$	0.31(19)	59.9	$1.14^{+0.11}_{-0.10}$	0.27(19)
FNAL1983	29	39.1	$1.21^{+0.25}_{-0.21}$	0.60(28)	39.1	$1.20^{+0.26}_{-0.21}$	0.58(32)

Table 2.3: Nominal fits to the dipole and z expansion parametrizations for each of the three data sets. "LL" denotes log likelihood. Errors on z expansion determinations of r_A^2 are determined from the error matrix, all others correspond to $\Delta(-2\text{LL}) = 1$. $N_a = k_{\rm max} - 4$ denotes the number of free expansion coefficients in the z expansion fit (Eq. (2.5)) with sum rule constraints from Eq. (2.11), prior scheme from Eq. (2.22), and Q^2 bounds from Table 2.2. The second column is the number of bins, including bins with zero data. For $N_a = 4$, the resulting fit parameters are displayed in Eq. (2.25).

form factor around $Q^2 = 0$:

$$\frac{1}{F_A(0)} \frac{dF_A(Q^2)}{dQ^2}\bigg|_{Q^2=0} = \frac{1}{6} r_A^2 \,. \tag{2.23}$$

It is also simple to compare the slope at $Q^2 = -t_0$,

$$\frac{dF_A(Q^2)}{dQ^2}\bigg|_{Q^2=-t_0} = \frac{dF_A(z)}{dz}\bigg|_{z=0} = a_1 \,. \tag{2.24}$$

The fit normalizations and axial radius squared (related to the slope at $Q^2 = 0$) for the nominal dipole and z expansion fits are delineated in Table 2.3. We note that the dipole fit purports to give an uncertainty for the radius that is nearly an order of magnitude smaller. The goodness of fit is better for the dipole model than for the z expansion, which is only possible because the dipole violates the requirements of QCD. This indicates a tension between the data and the expectation from analyticity.

The z expansion parameter values for the $N_a = 4$ fit of Table 2.3 are

$$[a_1, a_2, a_3, a_4] = \begin{cases} [2.24(10),\ 0.6(1.0),\ \text{-}5.4(2.4),\ 2.2(2.7)] & \text{(BNL)} \\ [2.25(10),\ 0.2(0.9),\ \text{-}4.9(2.3),\ 2.7(2.7)] & \text{(ANL)} \\ [2.02(14),\ \text{-}1.2(1.5),\ \text{-}0.7(2.9),\ 0.1(2.8)] & \text{(FNAL)} \end{cases} , \tag{2.25}$$

The errors reported here are the allowed variations in the fit parameters within the region described by a change of 1.0 in the -2LL function. We notice that, as expected, the higher-order parameters are less well-constrained than those at lower-order, indicated by the relative error on the parameters at each order.

For further evaluation of the fits, we turn to the differences in the fit parameter a_1, related to the slope by Eq. (2.24). Our nominal set of fits in Table 2.3 give the values

$$[a_1(\text{BNL}),\ a_1(\text{ANL}),\ a_1(\text{FNAL})] = \begin{cases} [2.23(10),\ 2.23(10),\ 2.02(14)\ ], & N_a = 3 \\ [2.24(10),\ 2.25(10),\ 2.02(14)\ ], & N_a = 4 \\ [2.22(10),\ 2.25(10),\ 2.02(14)\ ], & N_a = 5 \end{cases} , \tag{2.26}$$

showing excellent consistency as we increase the number of fit parameters. The inclusion of higher-order expansion terms in the power series has little effect on the fit results, a consequence of the smallness of z^k for increasing k as discussed after Eq. (2.19).

We may compare the resulting fit for $\mathcal{N}_{\text{fit}}$ to the expectation from Eq. (2.16) assuming $E_\nu = 1$ GeV, which yields

$$\begin{aligned} \mathcal{N}(Q^2_{\text{min}} = 0.06\,\text{GeV}^2) &\approx 1.13, \quad \text{(BNL)} \\ \mathcal{N}(Q^2_{\text{min}} = 0.05\,\text{GeV}^2) &\approx 1.11, \quad \text{(ANL)} \\ \mathcal{N}(Q^2_{\text{min}} = 0.10\,\text{GeV}^2) &\approx 1.23 \quad \text{(FNAL)} \end{aligned} , \tag{2.27}$$

well within the uncertainties reported in Table 2.3. Though one may worry that this normalization is sensitive to the energy distribution of the neutrino beam, this turns out not to be the case. The neutrino cross section in the beam energies considered does not change considerably, resulting in mild sensitivity to the energy. The dominant effect in values reported in Eq. (2.27) is the Q^2_{min} cut, which removes data from the domain where the differential cross section is largest.

The best fit differential cross section (left) and total free nucleon cross sections (right) are plotted in Fig. 2.2. Although the dipole and z expansion parametrizations of the differential cross section plots give predictions for the event Q^2 distributions that look identical, they imply total cross sections that differ by as much as 20%. This is best understood by studying the absolutely normalized differential cross sections in Fig. 2.3. In the Q^2 range of the fits (that is, above $Q^2 \gtrsim 0.1$ GeV^2), the difference in the differential cross section between the z expansion and dipole parametrizations can be mostly absorbed into a scale factor. The floating normalization of Eq. (2.13) plays the role of that scale factor. The largest deviations are then imposed by data close to $Q^2 = 0$, where the estimate of acceptance corrections to the bin content is unreliable and the data are consequently thrown away.

2.2.2 Systematics Studies

The uncertainties on results listed in Table 2.3 account only for the statistical errors from data. There are a number of systematic effects that could contribute additional uncertainties in the form factor parametrization. The z expansion parametrization permits the study and quantification of systematic corrections in a model-independent scheme, allowing for realistic assessment of the size of the errors. Strong dependence on systematic effects are an indication of underestimated errors, which are import to quantify and understand with the intention of reducing or removing them. In this section, we delineate the contributions of systematic effects to the form factor extraction and determine uncertainties on observables computed from the form factors.

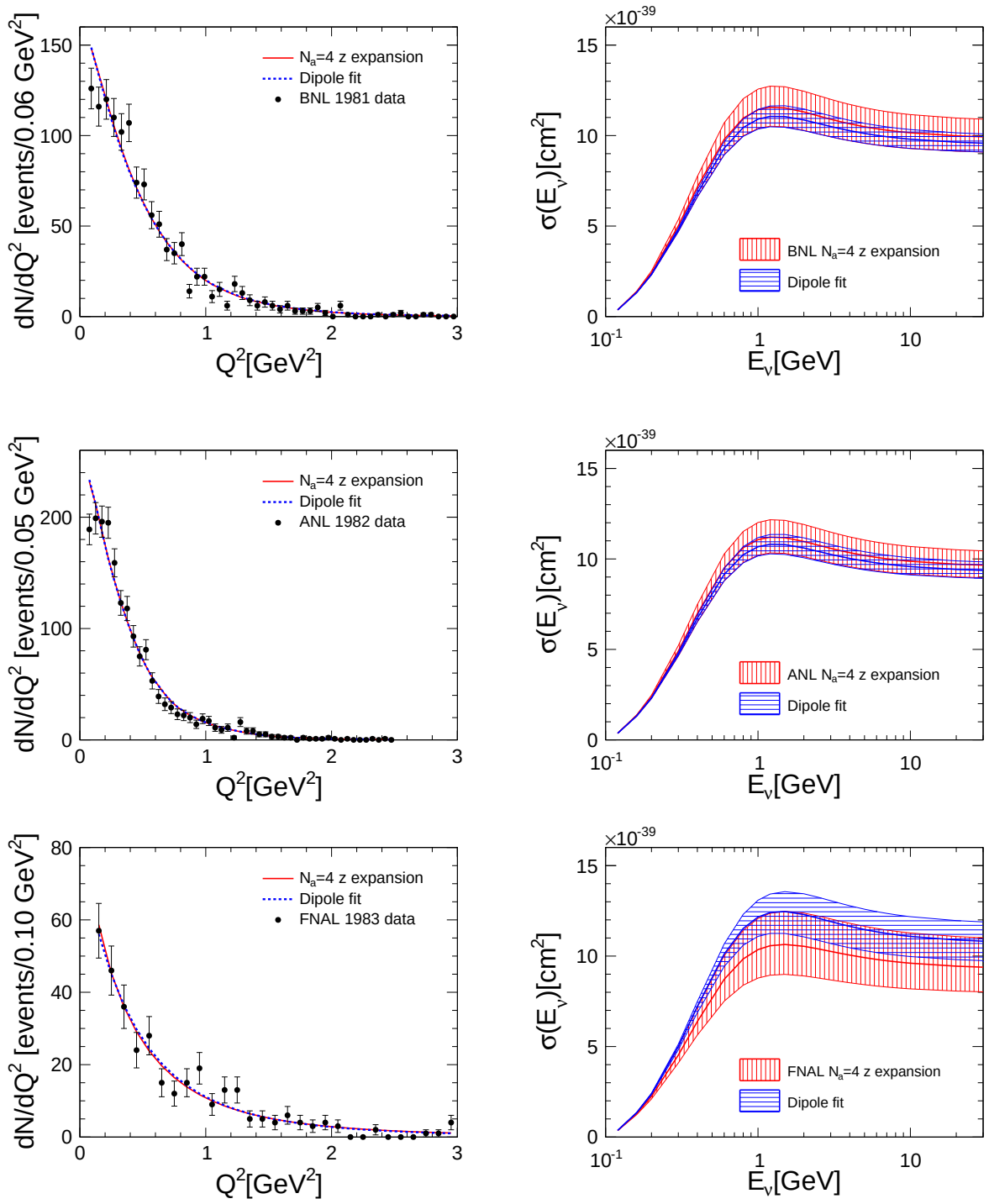

Figure 2.2: Best fit curves and errors for BNL1981 (top row), ANL1982 (middle row), and FNAL1983 (bottom row). The left column is the differential cross section data and best fit curves, and the right column is the free-neutron cross section, with errors propagated from deuterium. Red (solid, vertical stripes) corresponds to $N_a = 4$ z expansion and blue (dotted, horizontal stripes) to dipole in Table 2.3. First appeared in [41].

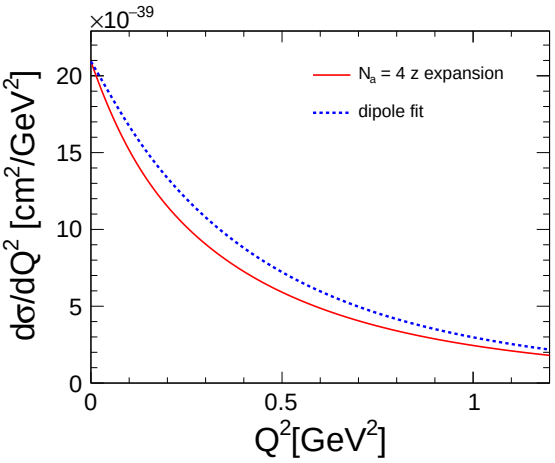

Figure 2.3: Absolutely normalized $d\sigma^N/dQ^2$ at $E_\nu = 10$ GeV. The z expansion (red) and dipole (blue) axial form factor parametrizations are the central values reported in Table 2.3 and are the same values used in the FNAL1983 results of Fig. 2.2. Despite the similarity of the dipole and z expansion parametrizations of the flux-convolved differential cross section in the left plots of Fig. 2.2, the difference in free nucleon cross sections can be attributed to a change in the shape of the form factor.

Choice of Priors

The data were fit with Gaussian priors on the z expansion coefficients to prevent noise from dominating the best fit results. Overly constraining priors have the potential to overpower the data, and weak priors could allow for large variations in fit results that conform with unphysical statistical fluctuations in the data. We validated our choice by fitting with priors

of varying widths, the widest of which we consider overly conservative. We find

$$
\begin{aligned}
&[a_1(\text{BNL}),\, a_1(\text{ANL}),\, a_1(\text{FNAL})] \\
&= \begin{cases}
[2.18(8),\ 2.17(8),\ 2.01(12)], & \left|\dfrac{a_k}{a_0}\right| \leq \min\left(3, \dfrac{15}{k}\right) \\
[2.23(10), 2.25(10), 2.02(14)], & \left|\dfrac{a_k}{a_0}\right| \leq \min\left(5, \dfrac{25}{k}\right) \\
[2.36(15), 2.41(15), 2.02(17)], & \left|\dfrac{a_k}{a_0}\right| \leq \min\left(10, \dfrac{50}{k}\right)
\end{cases} .
\end{aligned} \tag{2.28}
$$

There are no significant differences in the fit results with our default choice and the other prior choices, and the widest prior width increases the parameter uncertainties by up to 50% for the ANL and BNL data sets.

Choice of t_0

The parameter t_0 in the definition of the conformal mapping to z parameter space of Eq. (2.3) is an unphysical quantity and should not affect our fit results. The choice to use $t_0 \neq 0$ reduces the maximum size of $|z|$ in the kinematic range being studied, meaning that the z expansion need not be carried out to such a high order. To evaluate whether our choice of t_0 has any systematic effect, we compare the nominal fit of $t_0 = \bar{t}_0 = -0.28$ GeV^2 with $t_0 = 0$.

Since the definition of a_1 is dependent on our choice of t_0, we instead compare the slope of the form factor at $Q^2 = -\bar{t}_0$, defined by

$$
\bar{a}_1 \equiv a_1\big|_{t_0=\bar{t}_0} \equiv -4\,(t_+ - \bar{t}_0)\,F_A'(\bar{t}_0) \tag{2.29}
$$

with t_+ given by our particle production threshold as in Eq. (2.3). We must additionally increase the number of fit parameters N_a from 4 to 7, to keep consistent with the choice that

$|z|_{\max}^{N_a+1} \approx 0.02$ in the range $0 < Q^2 < 3$ GeV^2. We find

$$[\bar{a}_1(\text{BNL}),\, \bar{a}_1(\text{ANL}),\, \bar{a}_1(\text{FNAL})] = \begin{cases} [2.24(10), 2.25(10), 2.02(14)] & (N_a = 4,\, t_0 = \bar{t}_0) \\ [2.22(9),\ 2.21(10), 2.02(14)] & (N_a = 7,\, t_0 = 0) \end{cases} , \tag{2.30}$$

with little difference between fit schemes.

Flux Uncertainties

We estimated the error from uncertainty in the flux shape by varying the energy distribution provided in the BNL publication within its 1σ statistical error bars. The error was determined by shifting each bin up or down by 1σ and computing the difference from the nominal result. The contributions from each bin were added in quadrature and reported as an error separate from the statistical errors obtained from the Q^2 distribution. The result is

$$\bar{a}_1 = 2.24 \pm 0.10_{\text{stat.}Q^2} \pm 0.04_{\text{stat.}E_\nu} \quad (\text{BNL1981})\,. \tag{2.31}$$

The error from varying the flux was found to be subleading compared to the Q^2 distribution statistical errors. This error will also be small compared to the error from corrections due to acceptance and deuteron corrections, and so will be neglected in the rest of the analysis.

Subsets of Q^2 Range

We performed fits to subsets of the data to check for regions in which statistical fluctuations can have a negative impact on the fits. Neglecting certain regions in the fit ranges allows for isolation of the problem to specific kinematic ranges. We first removed data at high Q^2, fitting instead to the region with $Q^2 < 1$ GeV^2.

In a study analogous to Eq. (2.25), removing the high-Q^2 region gives the parameter values

$$[a_1, a_2, a_3, a_4]\big|_{Q^2 \leq 1\,\mathrm{GeV}^2} = \begin{cases} [1.99(15),\ 0.5(1.1), \text{-}3.6(2.6),\ 1.1(2.7)] & \text{(BNL)} \\ [2.29(14),\ 0.2(0.9), \text{-}5.2(2.5),\ 2.9(2.7)] & \text{(ANL)} \\ [1.88(25), \text{-}0.9(1.6), \text{-}0.3(2.9), \text{-}0.3(2.8)] & \text{(FNAL)} \end{cases} . \tag{2.32}$$

The equivalent to Table 2.3 for this subset of the data is given in Table 2.4. The Q^2 distributions for these fits are shown in Fig. 2.4. We see a 1-2σ shift in the central values of a_1 for the data sets.

A similar study was done using the fit range $Q^2 > 0.2$ GeV^2. The equivalent to Table 2.3 is shown in Table 2.5, and the analogous parameters to Eq. (2.32) are

$$[a_1, a_2, a_3, a_4]\big|_{Q^2 \geq 0.2\,\mathrm{GeV}^2} = \begin{cases} [2.35(10), \text{-}2.0(1.2), \text{-}1.4(2.8), 1.4(2.7)] & \text{(BNL)} \\ [2.34(10), \text{-}3.6(1.2),\ 1.6(2.8), 0.9(2.8)] & \text{(ANL)} \\ [2.04(16), \text{-}1.3(1.6), \text{-}0.5(3.0), 0.1(2.8)] & \text{(FNAL)} \end{cases} . \tag{2.33}$$

We again find a shift in the value of a_1 for different subsets of the data. However, for this subset of the Q^2 range, the computed r_A^2 shifts by more than 2σ. The form factor is no longer required to fit the exceptionally low bins in the low-Q^2 region, so the fit contorts to the bins in the $0.2 < Q^2 < 1.0$ GeV^2 region instead. The result is a larger fit normalization and squared axial radius.

The discrepancies in the fit results for the subsets of the Q^2 range are best understood in Fig. 2.5. This figure shows the residuals when plotting the ratio of the data to a theory

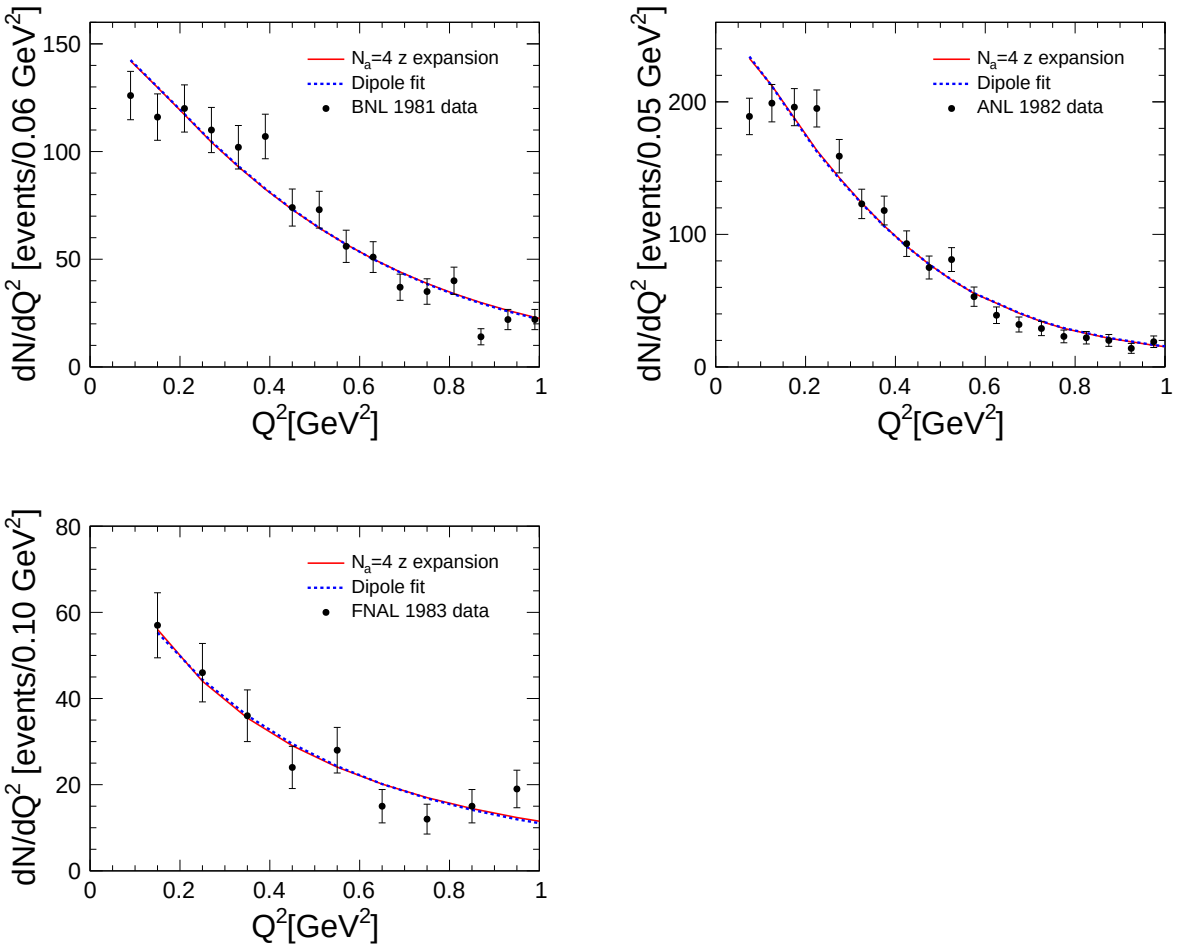

Figure 2.4: Q^2 distributions presented as in Fig. 2.2, except for $Q^2 < 1.0$ GeV^2. Best differential cross sections for BNL1981 (top left), ANL1982 (top right), and FNAL1983 (bottom). Red (solid) corresponds to $N_a = 4$ z expansion and blue (dotted) to dipole in Table 2.4.

		Dipole			$N_a = 3$		
Experiment	N_{bins}	-2LL	$\mathcal{N}_{\text{fit}}$	r_A^2 [fm^2]	-2LL	$\mathcal{N}_{\text{fit}}$	r_A^2 [fm^2]
BNL1981	16	24.7	$1.16^{+0.08}_{-0.08}$	0.348(48)	27.2	$1.17^{+0.14}_{-0.13}$	0.32(22)
ANL1982	19	28.2	$1.14^{+0.07}_{-0.06}$	0.452(52)	31.7	$1.15^{+0.10}_{-0.09}$	0.38(19)
FNAL1983	9	8.3	$1.16^{+0.26}_{-0.18}$	0.33(12)	8.3	$1.22^{+0.29}_{-0.23}$	0.54(31)
		$N_a = 4$			$N_a = 5$		
Experiment	N_{bins}	-2LL	$\mathcal{N}_{\text{fit}}$	r_A^2 [fm^2]	-2LL	$\mathcal{N}_{\text{fit}}$	r_A^2 [fm^2]
BNL1981	16	27.0	$1.17^{+0.14}_{-0.13}$	0.28(22)	26.6	$1.16^{+0.14}_{-0.13}$	0.24(22)
ANL1982	19	30.5	$1.14^{+0.10}_{-0.10}$	0.31(20)	29.2	$1.13^{+0.11}_{-0.10}$	0.24(20)
FNAL1983	9	8.2	$1.23^{+0.29}_{-0.24}$	0.56(29)	8.1	$1.24^{+0.30}_{-0.24}$	0.57(26)

Table 2.4: Same as Table 2.3, but fitting only to data with $Q^2 \leq 1.0$ GeV^2. For $N_a = 4$ the resulting fit parameters are displayed in Eq. (2.32).

		Dipole			$N_a = 3$		
Experiment	N_{bins}	-2LL	$\mathcal{N}_{\text{fit}}$	r_A^2 [fm^2]	-2LL	$\mathcal{N}_{\text{fit}}$	r_A^2 [fm^2]
BNL1981	47	60.7	$1.25^{+0.21}_{-0.14}$	0.61(13)	62.4	$1.28^{+0.20}_{-0.17}$	0.83(24)
ANL1982	46	43.2	$1.40^{+0.25}_{-0.38}$	$1.45^{+0.92}_{-0.49}$	45.8	$1.32^{+0.21}_{-0.18}$	1.04(24)
FNAL1983	28	38.2	$1.16^{+0.22}_{-0.16}$	0.33(7)	39.1	$1.22^{+0.31}_{-0.25}$	0.64(31)
		$N_a = 4$			$N_a = 5$		
Experiment	N_{bins}	-2LL	$\mathcal{N}_{\text{fit}}$	r_A^2 [fm^2]	-2LL	$\mathcal{N}_{\text{fit}}$	r_A^2 [fm^2]
BNL1981	47	61.5	$1.26^{+0.21}_{-0.18}$	0.74(25)	60.9	$1.25^{+0.23}_{-0.19}$	0.67(24)
ANL1982	46	45.8	$1.32^{+0.23}_{-0.20}$	1.03(25)	45.8	$1.32^{+0.25}_{-0.21}$	1.05(24)
FNAL1983	28	39.1	$1.22^{+0.32}_{-0.25}$	0.63(30)	39.0	$1.21^{+0.34}_{-0.26}$	0.60(35)

Table 2.5: Same as Table 2.3, but fitting only to data with $Q^2 \geq 0.2\,\text{GeV}^2$. For $N_a = 4$ the resulting fit parameters are displayed in Eq. (2.33).

prediction from a joint fit to all data sets at once[1]. The data all appear to prefer the same Q^2-dependent shape over the entire range of data available. The distortions are clearly significant if only the low-Q^2 region is considered. We test the data-to-fit ratio against a null hypothesis of a flat distribution over the entire Q^2 range using a χ^2 test, which yields a p-value of 0.12 and is not exceptional. To use the χ^2 fit, we collected the contents of the

1. An equivalent plot with fits to individual datasets exhibits the same behavior, so the joint fit is taken for demonstration.

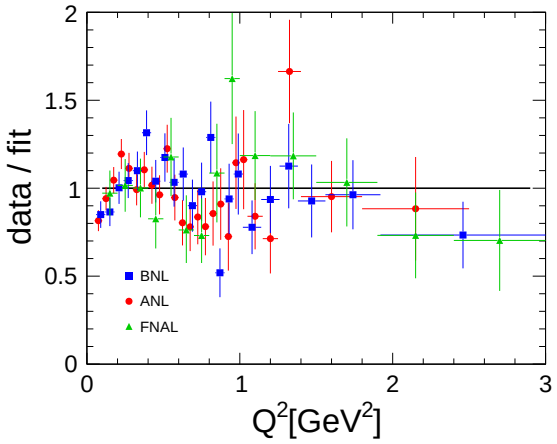

Figure 2.5: Data divided by best fit prediction for the Q^2 distributions displayed in Fig. 2.2 and parameter values in Eq. (2.25), for BNL (blue) ANL (red), and FNAL (green). Calculated $\chi^2/N_{\rm bins}$ are 35.3/22, 41.2/25, and 10.7/14 for BNL, ANL, and FNAL respectively.

high-Q^2 bins into larger bins.

The z expansion, constrained by the analytic structure inherent to quantum field theories such as QCD, cannot describe the localized shape distortions that are visible in Fig. 2.5. As a consequence, the residuals are inconsistent with the any form factors derived from QCD. This discrepancy must be the result of a systematic error in the experimental data resulting from including the effects of bias due to hand scanning or from more advanced deuteron corrections. These effects are explored and quantified in the following sections.

Acceptance Corrections

One of the systematics that must be accounted for is corrections for acceptance of events. The deuterium bubble chamber data was taken on photograph plates and hand scanned by experimenters. A scanning efficiency to estimate the bias introduced in the hand scanning procedure was included in Fig. 1 of ANL1982 [45]. The efficiency ranges from $e = 90 \pm 7\%$ for the range 0.05 GeV^2 $< Q^2 <$ 0.1 GeV^2 to $e = 98 \pm 1\%$ for $Q^2 >$ 0.15 GeV^2. The reduction in efficiency at low-Q^2 is a consequence of the tracks being too short to reliably

measure, and the first bin in each data set has been discarded as a result of this.

The efficiency is included as an enhancement of the differential Q^2 distribution. To test the influence of the efficiency correction, we allow the correction to modify the event Q^2 distributions by a term of the form

$$\frac{dN}{e(Q^2)} \rightarrow \frac{dN}{e(Q^2)+\eta de(Q^2)} = \frac{dN}{e(Q^2)}\left(1+\eta\frac{de(Q^2)}{e(Q^2)}\right)^{-1} \tag{2.34}$$

that includes a correlated shift in the efficiency of each bin. The parameter η is a prefactor that is fit with a Gaussian prior $\eta = 0 \pm 1$. The efficiency correction $e(Q^2)$ is deduced by linearly interpolating between bins in the efficiency estimates from the ANL1982 publication, and $de(Q^2)$ from the statistical errors on those bins. We assume that the BNL1981 and FNAL1983 data sets have corrections of the form in Eq. (2.34) and, for simplicity, that the efficiency $e(Q^2) \pm de(Q^2)$ are the same as those for ANL1982.

Including acceptance corrections and fitting to the region $Q^2 < 1.0$ GeV^2, the best fit parameters and goodness of fit values are

$$\begin{aligned}
\text{BNL}: \quad [\bar{a}_1,\, -2\text{LL}] &= \begin{cases} [1.99(15), 27.0] & \text{(without)} \\ [2.04(15), 26.0] & \text{(with)} \end{cases}, \\
\text{ANL}: \quad [\bar{a}_1,\, -2\text{LL}] &= \begin{cases} [2.29(14), 30.5] & \text{(without)} \\ [2.38(14), 26.3] & \text{(with)} \end{cases}, \\
\text{FNAL}: \quad [\bar{a}_1,\, -2\text{LL}] &= \begin{cases} [1.88(25), 8.2] & \text{(without)} \\ [1.88(25), 8.2] & \text{(with)} \end{cases},
\end{aligned} \tag{2.35}$$

with the parameter η taking the values -1.9, -1.0, and $+0.01$ for ANL1982, BNL1981, and FNAL1983, respectively. The negative values η indicate that the number of events in the low-Q^2 bins are underestimated with respect to the cross section prediction for those bins. However, the efficiency corrections for each data set are not large and the goodness of fit improves only moderately when the correction is included, indicating that the acceptance

correction has only minor impact on the fits.

Deuteron Corrections

The deuteron correction from Singh [47] is also unable to account for the shape distortions in the data seen in Fig. 2.5. This deuteron correction modifies only the low-Q^2 behavior and is unity for $Q^2 > 0.2$ GeV^2.

One may wonder if a modern deuteron correction would be able to better accommodate the data and during fitting. The results of Shen *et al.* [50] is used as a representative for a modern account of deuterium corrections. The nuclear effects of Singh are stronger than the correction of Singh and modifies the event distribution by as much as 20% over a broad range of Q^2. Unlike the correction presented by Singh, the deuteron effects presented by Shen are assumed to be energy dependent and are computed at a few choices of energy. We assume the deuterium correction from Shen is only dependent on Q^2 and use the deuterium correction computed with $E_\nu = 1$ GeV for $R(Q^2)$ in Eq. (2.17). The Shen correction is presented only for the region $Q^2 \lesssim 1.0$ GeV^2, so data above 1.0 GeV^2 are neglected. The relative size of the corrections of Refs. [47, 50] and of the unmodified free nucleon differential cross section are shown in Fig. 2.6.

We compute fits with the deuterium corrections presented by Shen *et al.* and compare to the fits from Eq. (2.32). The fit results are

$$\begin{aligned}
\text{BNL}: \quad [\bar{a}_1,\, -2\text{LL}] &= \begin{cases} [1.99(15), 27.0] & \text{(Singh)} \\ [2.16(14), 25.1] & \text{(Shen et al.)} \end{cases}, \\
\text{ANL}: \quad [\bar{a}_1,\, -2\text{LL}] &= \begin{cases} [2.29(14), 30.5] & \text{(Singh)} \\ [2.46(13), 29.2] & \text{(Shen et al.)} \end{cases}, \\
\text{FNAL}: \quad [\bar{a}_1,\, -2\text{LL}] &= \begin{cases} [1.88(25),\ 8.2] & \text{(Singh)} \\ [2.00(25),\ 9.1] & \text{(Shen et al.)} \end{cases}. \qquad (2.36)
\end{aligned}$$

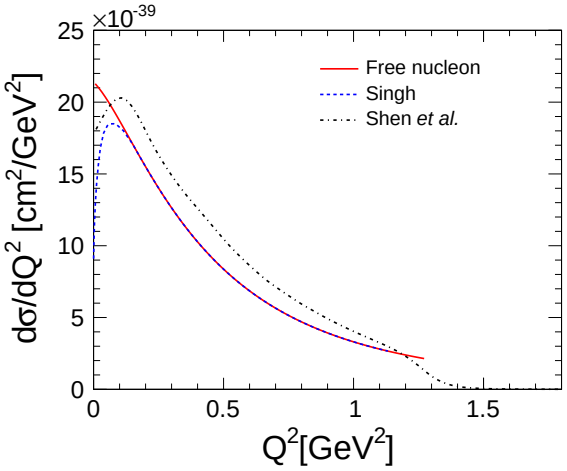

Figure 2.6: Comparison of the free nucleon differential cross section (solid red) to the deuterium cross section predicted by Refs. [47, 50] (blue and black dotted, respectively).

The modified deuterium correction of Ref. [50] only shifts the parameter values by at most 1σ, and again no significant improvement in goodness of fit is found. However, the difference between the corrections of Singh and Shen is not an indicator of the error on estimates of the deuterium correction. This suggests that there is potential for a future study of systematic errors on the deuterium corrections even in the absence of a new deuterium experiment.

2.2.3 Final Results

Applying the knowledge acquired from the systematic tests of the previous section, we perform a joint fit to the three data sets to extract the best estimate of the form factor from deuterium bubble chamber data. We focus on treating the effects of the two most important systematics, the acceptance and deuteron corrections. The Q^2 distributions are fit simultaneously with the same choice of F_A for all three data sets. The fits use our default set of inputs from Table 2.1 along with $t_0 = -0.28$ GeV^2 and $N_a = 4$ free parameters to prevent significant errors due to truncating the z expansion power series prematurely. Each data set is allowed an independent correction parameter η from Eq. (2.34) to allow the acceptance efficiencies to float independently.

We present the parameters and error matrices for two final fits. In the first fit, we implement a χ^2 fit (Eq. (2.21)), which applies the updated Shen deuterium correction and fits only up to $Q^2 < 1.0$ GeV^2. To estimate the effects of deuterium and other residual systematics, we apply an uncorrelated inflation of errors by including 10% of the bin content added in quadrature with the σ_i of Eq. (2.21). As was shown in the previous section, the neglect of data above $Q^2 > 1.0$ GeV^2 had minimal impact on the resulting fits. The second is a binned log-likelihood fit (Eq. (2.20)) that utilizes all of the data up to $Q^2 < 3.0$ GeV^2 and the Singh deuterium correction, neglecting any systematics associated with corrections due to deuterium effects. We advocate the use of the χ^2 fit with a full systematic error budget.

For our χ^2 fit with full treatment of systematic errors, the fit parameters are

$$[a_1, a_2, a_3, a_4] = [2.30(13), -0.6(1.0), -3.8(2.5), 2.3(2.7)]\,, \tag{2.37}$$

with errors computed from $\delta\chi^2 = 1$. The diagonal entries of the error (covariance) matrix, computed from the inverse of the Hessian matrix for $\chi^2(\{a_k\})$, are

$$E_{\text{diag.}} = [0.0154, 1.08, 6.54, 7.40]\,. \tag{2.38}$$

and the four-dimensional correlation matrix is

$$C_{ij} = \begin{pmatrix} 1 & 0.350 & -0.678 & 0.611 \\ 0.350 & 1 & -0.898 & 0.367 \\ -0.678 & -0.898 & 1 & -0.685 \\ 0.611 & 0.367 & -0.685 & 1 \end{pmatrix}. \tag{2.39}$$

For our log-likelihood fit, which neglects deuterium systematic errors, the fit parameters are

$$[a_1, a_2, a_3, a_4] = [2.28(8), 0.25(95), -5.2(2.3), 2.6(2.7)]\,. \tag{2.40}$$

The diagonal entries of the error matrix are

$$E_{\text{diag}} = [0.00635, 0.781, 4.49, 6.87]\,, \tag{2.41}$$

The four-dimensional correlation matrix is

$$C_{ij} = \begin{pmatrix} 1 & 0.321 & -0.677 & 0.761 \\ 0.321 & 1 & -0.889 & 0.313 \\ -0.677 & -0.889 & 1 & -0.689 \\ 0.761 & 0.313 & -0.689 & 1 \end{pmatrix}. \tag{2.42}$$

The error matrix is given by $E_{ij} = \delta a_i \delta a_j C_{ij}$ in both cases. Note that $(E_{\text{diag.}})_i \approx (\delta a_i)^2$, reflecting approximately Gaussian behavior.

Fig. 2.7 shows the form factor F_A as a function of both Q^2 and of z plotted for our preferred fit in Eqs. (2.37)–(2.39). The red (vertical hash) is the central value and error band for the z expansion and the green (horizontal hash) corresponds to the "world-best" dipole from Ref. [51]. The plot illustrates how a model-independent parametrization of the form factor compares with the dipole model extraction on nearly-free nucleon targets. The behavior of the z expansion in z parameter space is nearly linear for $|z| \lesssim 0.2$ GeV^2, reaffirming the assertion that the higher-order parameters in the z expansion are not constrained by the data. This is also reflected by the consistency of a_k with zero for $k \geq 2$ in Eq. (2.37). For the range $z \gtrsim 0.2$ GeV^2, the form factor is outside the region $Q^2 < 1.0$ GeV^2, so the z expansion parameters are no longer strongly constrained by data and the sum rule constraints take over.

Fig. 2.8 shows the total cross section plotted for both ν_μ and $\bar{\nu}_\mu$. The z expansion parametrization is again shown in red and the dipole in green. To quantify the uncertainty in the cross section, we give the cross sections at representative energies of $E_\nu = 1.0$ GeV

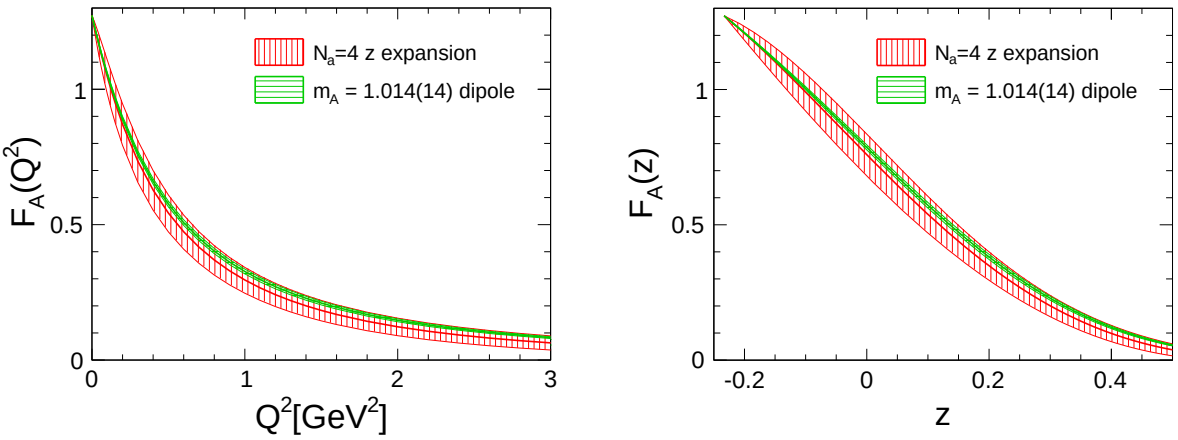

Figure 2.7: Final form factor from Eqs. (2.37)–(2.39). Also shown is the dipole axial form factor with axial mass $m_A = 1.014(14)$ GeV [51].

and $E_\nu = 3.0$ GeV. The z expansion cross sections are

$$\begin{aligned}\sigma_{\nu n\to\mu p}(E_\nu = 1\,\text{GeV}) &= 10.1(0.9)\times 10^{-39}\,\text{cm}^2\,,\\ \sigma_{\nu n\to\mu p}(E_\nu = 3\,\text{GeV}) &= 9.6(0.9)\times 10^{-39}\,\text{cm}^2\,,\end{aligned} \tag{2.43}$$

for neutrinos and

$$\begin{aligned}\sigma_{\bar\nu p\to\mu n}(E_\nu = 1\,\text{GeV}) &= 3.83(23)\times 10^{-39}\,\text{cm}^2\,,\\ \sigma_{\bar\nu p\to\mu n}(E_\nu = 3\,\text{GeV}) &= 6.47(47)\times 10^{-39}\,\text{cm}^2\,,\end{aligned} \tag{2.44}$$

for antineutrinos.

Table 2.6 shows the axial radius (defined in Eq. (2.23)) extracted for $N_a = 3$, 4, and 5 for each individual data set and for a joint fit to all three data sets. The axial radius is useful for comparing to pion electroproduction, where comparison is most robust in the limit as

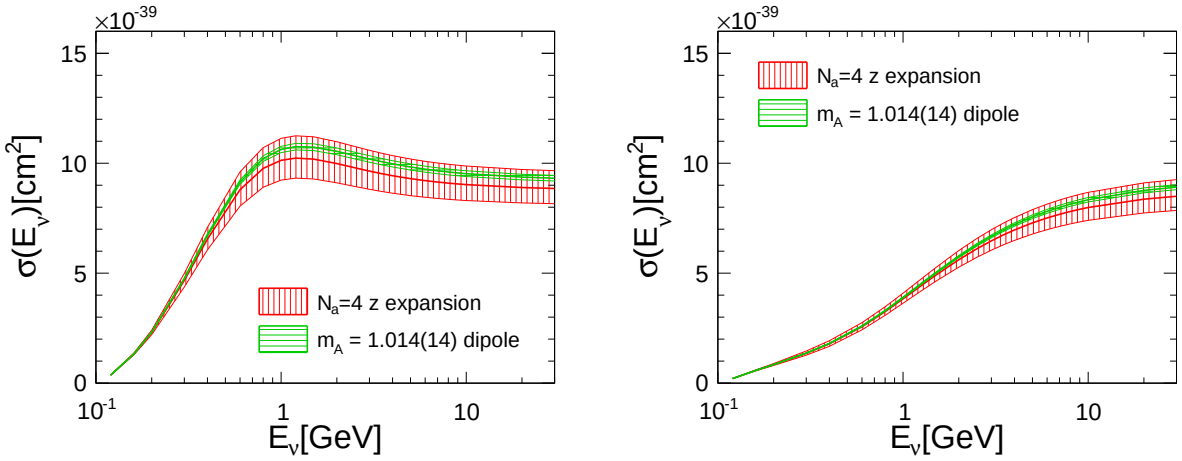

Figure 2.8: Total free-nucleon cross section implied by Eqs. (2.37)–(2.39). The ν_μ cross section is plotted on the left and $\bar{\nu}_\mu$ on the right. Also shown is the total cross section for the dipole axial form factor with axial mass $m_A = 1.014(14)$ GeV [51].

Data set	r_A^2 [fm^2] ($N_a = 3$)	r_A^2 [fm^2] ($N_a = 4$)	r_A^2 [fm^2] ($N_a = 5$)
BNL 1981	0.56(23)	0.52(25)	0.48(26)
ANL 1982	0.69(21)	0.63(23)	0.57(24)
FNAL 1983	0.63(34)	0.64(35)	0.64(35)
Joint Fit	0.54(20)	0.46(22)	0.39(23)

Table 2.6: Axial radius extracted using values from Table 2.1, and default scheme choices as discussed in the text. Note that the joint fit is not an average, but a simultaneous fit to all data sets.

$Q^2 \to 0$. The fit in Eqs. (2.37)–(2.39) gives the best extraction of the axial radius

$$r_A^2 = 0.46(22)\,\text{fm}^2\,. \tag{2.45}$$

An extraction of the axial radius from pion electroproduction data can be found in Ref. [39], where the dipole model also strongly influences the extracted axial radius.

2.2.4 Discussion

As an exercise, the dipole model may be recast in the z expansion parametrization and the coefficients computed as functions of m_A. If this is done, the z expansion coefficients computed from the dipole model increase linearly as $a_k \sim k$, in violation of the unitarity bounds required by QCD in Sec. 2.1. Additionally, the corresponding dipole parametrization of the vector form factor is already known to be inconsistent with experimental measurements from electron-proton scattering. Thus, one should consider the dipole ansatz to be unnatural.

We extracted the axial form factor from deuterium bubble chamber experiment data and have assigned a complete error budget. We provided two alternative extractions of the form factor. The first of these extractions fits to a subset of the data, but contains estimates of systematic errors due to deuterium nuclear model corrections and any residual systematics. The second extraction fits to the full Q^2 range of the data, but uses an old estimate of the effects of deuterium corrections and neglects any systematic corrections to the form factor. These results are presented in Eqs. (2.37)–(2.42). We also report the total free nucleon cross section and axial radius squared in Eqs. (2.43) and (2.45), and find the errors to be an order of magnitude larger than the errors presented in Ref. [51].

In Figs. 2.7 and 2.8, the z expansion error bands are significantly larger than those of the dipole model in both Figs. 2.7 and 2.8. This is an indication that the dipole model contributed its own (mis-)information to the fit. Because of its theoretical shortcomings, continued use of the dipole model runs the risk of introducing unquantifiable systematic errors. This z expansion parametrization study demonstrates that even low-statistics deuterium bubble chamber data are constraining enough for the dipole model to underestimate systematic errors. The comparison of neutrino scattering to electron scattering is especially illuminating in this regard. It is interesting to note that the extractions of the proton charge radius from the corresponding vector form factor has larger relative uncertainties than the axial charge radius from the dipole model, despite how the vector form factors are constrained by data from a monoenergetic beam, a free nucleon target, and orders of magnitude more

statistics [49, 52].

The residuals plot shown in Fig. 2.5 suggests the existence of some unquantified correction to the differential cross section. The discrepancies of the data set residuals from a uniform line hint at a potentially correlated systematic effect across all of the experiments. These variations are strongest for the low-Q^2 region, where the corrections due to acceptance and deuteron models are suspected to be most prominent, but variations appear by eye to be present over the entire Q^2 range.

Fig. 2.9 shows the quasielastic differential cross section for the MINERνA data, plotted as a function of reconstructed Q^2, versus the form factor extraction from Eqs. (2.37)–(2.39) and the dipole model parametrization. If the dipole model is used, then the error bars are small and the discrepancy between the data and the theory appears to be due to nuclear model corrections. However, a realistic uncertainty from the z expansion is large enough to explain the observed data-theory discrepancy, leaving the source of the discrepancy ambiguous. If the goal is to use data such as these to constrain the nuclear models, then the uncertainty on the nucleon form factors must be significantly reduced.

The recent popularity of meson exchange current [54] and short-range correlations as a contribution to explain the larger cross section for MiniBooNE data may indicate stronger binding of nucleons into deuteron-like pairs than previously thought. From our comparison of the effects of the updated deuterium correction of Ref. [50] to the previous estimate from Ref. [47], we found no significant change in the best fit form factor. This is the same argument as discussed at the end of Sec. 2.2.1, but in the context of deuterium corrections. Despite the differences between the Shen and Singh deuterium effects (Fig. 2.6), the differences between the cross sections obtained from applying these corrections are largely absorbed into the floating normalization of Eq. (2.13). The absence of error estimates on the deuterium corrections make it difficult to assess the potential impact of nuclear models. This suggests a possible area for future exploration.

An updated deuterium bubble chamber experiment with increased statistics is an enticing

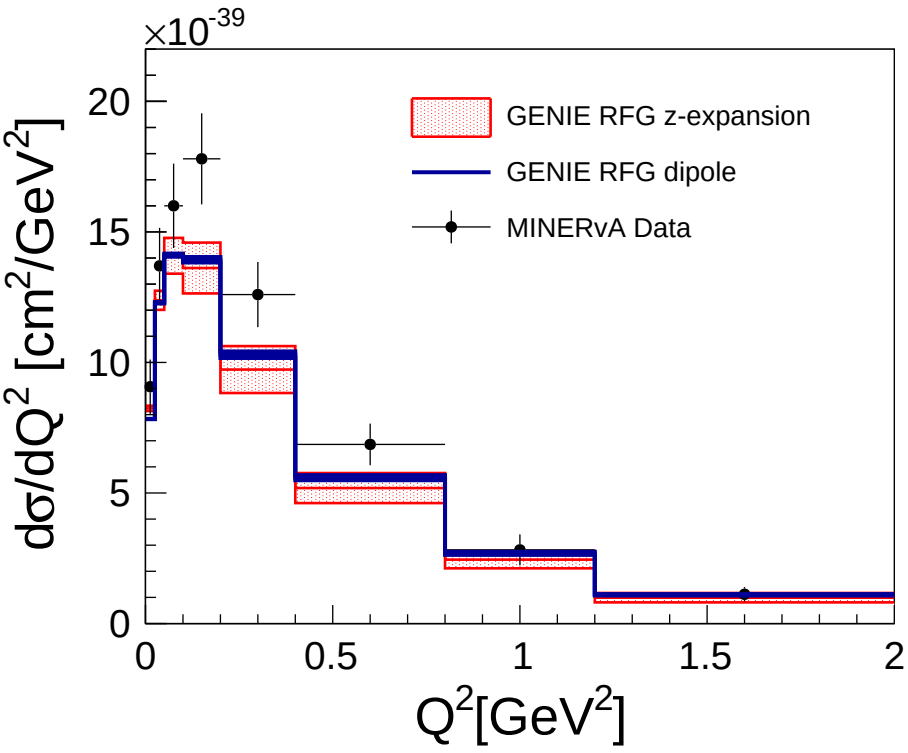

Figure 2.9: Plot of the charged-current quasielastic differential cross section on carbon as a function of reconstructed Q^2 for data from the MINERνA experiment [53] versus the prediction from GENIE with the Relativistic Fermi Gas (RFG) model. Two cross sections from GENIE are shown. The red band uses the form factor parameters from from Eqs. (2.37)–(2.39), while the blue band uses the dipole model with $m_A = 1.014(14)$ GeV [51].

strategy to help reduce uncertainties on the axial form factor. Modern experiments can reach much higher intensities, meaning that more statistics could be collected over a shorter run time. However, safety concerns about large quantities of deuterium contained underground must be addressed. The challenges involved and cost of making the necessary precautions to prevent accidents are at this time the main hurdles that need to be overcome.

As an alternative to an updated deuterium experiment, one could perform a first-principles computation with lattice QCD to extract the axial form factor. Lattice QCD computations are valuable because they can entirely circumvent the systematic uncertainties due to nuclear corrections. In doing so, they offer a way to compute the form factor without appealing to a specific nuclear model and introducing unquantifiably systematic errors. Lattice QCD

computations offer a way to provide a systematically improvable determination of the form factor. This approach is the basis of the remaining chapters, and will be discussed in detail after an interlude on event generators.

2.3 Implementation of z Expansion in GENIE

Neutrino event generators are a necessary tool for studying neutrino scattering data. The event generators allow study the effects of different oscillation observables on a given experimental setup. Realistic descriptions of detector geometries are simulated and predictions of observed events can be made based on an assumed oscillation model. The generators account for descriptions of nuclear matter and interactions of particles with the detector volume to fully characterize the efficiencies of experiments.

Typical Monte Carlo event generators are built with the assumption that the atomic nucleus is a weakly-bound gas of nucleons. The assumption of weakly-bound nucleons means that the nuclear model rely on free-nucleon amplitudes to describe the intranuclear interactions. As a consequence, the neutrino event generators take free-nucleon form factors as input to a sophisticated model, and accurate free-nucleon form factors are vital to their success.

GENIE (Generates Events for Neutrino Interaction Experiments) [55] is one such Monte Carlo event generator. The goal of GENIE is to describe neutrino interactions over a wide expanse of energy regimes, from MeV to PeV. GENIE is made to be modular; there are many nuclear models, form factor parametrizations, and event simulation channels that can be swapped out for others or turned on and off. This makes it a prime candidate for introducing the z expansion parametrization as a form factor module that can be utilized by the neutrino community.

2.3.1 The z Expansion in GENIE

The z expansion parametrization has been implemented into GENIE as a module that can be turned on by the user. This module is a replacement of the dipole form factor model. To accompany the z expansion module, reweighting routines have been written to vary over form factor models with different z expansion parameters. One of the modules, for reweighting with a covariance matrix, is general and may be used with other parameters as well provided that the correlations between parameters are known. These routines have been validated and included into the main release of GENIE.

The z expansion module within GENIE was made to be versatile. The module will accept z expansion parametrizations of the axial form factor with any number of expansion coefficients, t_0, and cutoff t_+. There is also a switch that allows one to turn on and off the sum rule constraints on the z expansion parameters. These parameters are specified in the default parameter file, `UserPhysicsOptions.xml`.

When generating Monte Carlo event samples, it is often necessary to generate many data sets with parameters shifted from their nominal values. Generating a completely new sample with shifted parameters requires computing many cross section integrals as well as the full simulation of a new event sample, which can be costly both in terms of human time and of disk storage. As an alternative, events in an existing Monte Carlo sample can be given weights according to the probability of generating that event in the new parameter scheme. By doing so, one sidesteps the costs of generating a new, independent data set from scratch. This concept is known as event reweighting, and GENIE now by default allows for reweighting of the first four z expansion parameters.

For charged current quasielastic events, computing the weights for the new parameter scheme is simple. Suppose an existing Monte Carlo sample was generated with a monoenergetic distribution in Q^2 governed by a differential cross section $\frac{d\sigma}{dQ^2}(F_A)$, where F_A is some assumed axial form factor. The probability of generating the same event in a world where

the axial form factor is instead F_A' is just the ratio of the cross sections,

$$w_i = \left(\frac{d\sigma}{dQ^2}(F_A', Q_i^2) / \frac{d\sigma}{dQ^2}(F_A, Q_i^2) \right) , \tag{2.46}$$

where the index i denotes the event that is being reweighted. If the events were chosen to reproduce the differential cross section, then we can reweight the fractional number of events in each bin to a new scheme by applying the transformation

$$\begin{aligned} \frac{\Delta Q_k^2}{N_{\text{tot}}} \sum_{i \in k} \left(\frac{dN}{dQ^2} \right)_i &= \frac{\Delta Q_k^2}{\sigma_{\text{tot}}} \sum_{i \in k} \left(\frac{d\sigma}{dQ^2} \right)_i \\ \rightarrow \frac{\Delta Q_k^2}{\sigma_{\text{tot}} \sum_i w_i} \sum_{i \in k} \left(\frac{d\sigma}{dQ^2} \right)_i w_i &= \frac{\Delta Q_k^2}{\sigma'_{\text{tot}}} \sum_{i \in k} \left(\frac{d\sigma'}{dQ^2} \right)_i , \end{aligned} \tag{2.47}$$

where k sums over bins in Q^2, ΔQ_k^2 is the width of bin k, and the sums $i \in k$ are taken only over weights within a single Q^2 bin. The primes in the last line indicate that the cross section is computed with the updated form factor F_A'.

The method for computing weights outlined previously is a specific case of weight generation. In general, the routines generate a weight by perturbing the central value according to the relation

$$\mathcal{O}_i' = \mathcal{O}_i \left(1 + k \frac{\delta \mathcal{O}_i}{\mathcal{O}_i} \right) , \tag{2.48}$$

where k is some systematic parameter (given the name "tweak dial" in GENIE), $\mathcal{O}_i$ is some observable for event i, and $\delta \mathcal{O}_i$ the error on that observable. We may recover Eq. (2.47) if we let $\mathcal{O}_i = \frac{d\sigma}{dQ^2}$, $\delta \mathcal{O}_i = \left(\frac{d\sigma'}{dQ^2} - \frac{d\sigma}{dQ^2} \right)$, and $k = 1$. This more general case is applied to reweight distributions under a wider set of event channels, since not all methods have simple ratios of cross sections like charged current quasielastic scattering. The GENIE reweighting framework is written with Eq. (2.48) in mind and so the CCQE reweighting algorithms are recast to fit this form instead of the form in Eq. (2.47).

2.3.2 Validation of GENIE Reweighting Routines

The GENIE z expansion reweighting packages have been validated against both independent Monte Carlo generation runs and cross section computations from an independent code. The intent is to show that the z expansion module and reweighting software behave as expected.

The first test demonstrates that an event sample can be reweighted from the dipole form factor with some given m_A to a z expansion form factor. To compute the event distributions in Fig. 2.10, we compute a monoenergetic sample of 5×10^4 CCQE events on a carbon target with both the dipole model and the new z expansion module. To make the difference between the two form factors clearly distinguishable by eye, we start with an $m_A = 0.50$ GeV sample. The reweighting routine converts the dipole sample directly to a z expansion sample and can be compared with the independent sample generated with the z expansion.

The reweighting program used to generate the weights used in Fig. 2.10 is named `gRwght1Scan`, which reweights using any generic systematic tweak dial. This reweights by changing the value of the tweak dial named `AxFFCCQEshape`. The default (tweak dial = 0) is a pure dipole form factor, and a tweak dial value of +1 is a pure z expansion form factor. After applying the weights, one ends up with a Monte Carlo sample with the z expansion parameters as they are defined in the default GENIE parameters file, `UserPhysicsOptions.xml`. This is demonstrated in Fig. 2.10. Agreement between the reweighting algorithm and the expectation is demonstrated by the agreement between the blue and red histograms, within statistical errors. The left plot shows the raw event distributions, and the right plot shows the event distributions normalized to the nominal dipole distribution, shown in black.

The next test checks several aspects of the code for consistency. The tests are separated into distinct parts, and then are collected into a single summary figure, Fig. 2.11. The test involves:

- Validating the z expansion cross section and error against an independent code
- Validating reweighting of parameters on a grid against direct reweighting from one

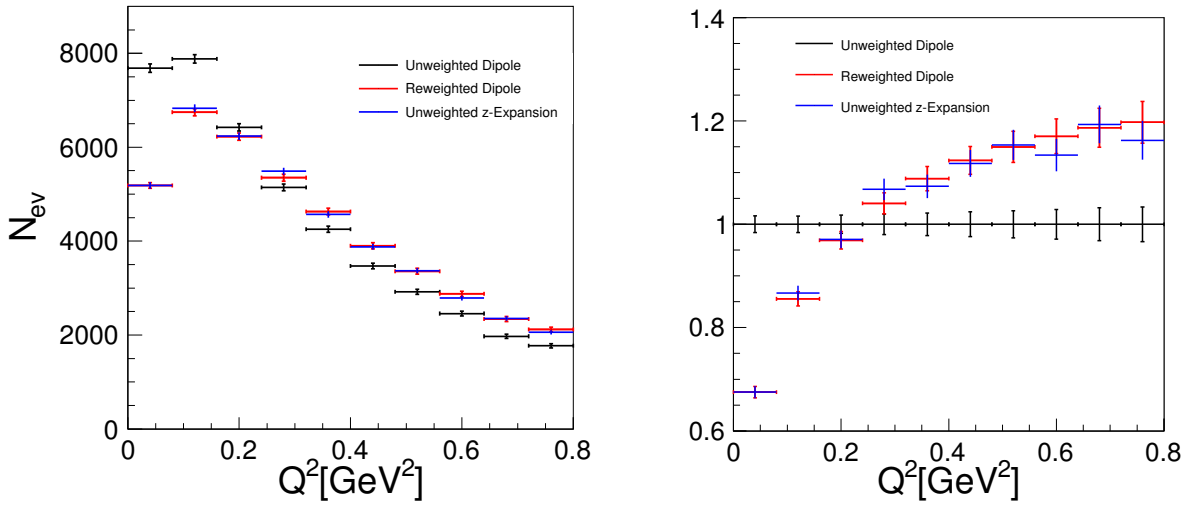

Figure 2.10: Plot of 50k pure CCQE events to demonstrate consistency of reweighting routine for converting dipole distributions into z expansion distributions. A nominal sample of dipole events (black) is modified with reweighting to generate a sample with a new cross section (red). This new sample is compared against an equivalent sample generated from scratch with a z expansion cross section (blue). The blue and red distributions are consistent within error bars. The left plot shows the raw number distribution of $E_\nu = 1$ GeV ν_μ events generated on a carbon-12 target. To make the dipole clearly distinguishable from z expansion, a dipole model with $m_A = 0.5$ GeV was used for the black data. The right shows the same data, but normalized to the nominal dipole sample (black).

parameter set to another

- Validating the covariance reweighting against direct reweighting

This code uses all of the new reweighting utilities, given the names: `grwghtnp`, "N-parameter" reweighting for reweighting with a covariance matrix, `grwghtzexpdirect`, for reweighting for directly from one parameter set to another, and `grwghtzexpaxff`, for reweighting the z expansion parameters on a grid.

There are two methods employed for finding errors on the cross sections. They are referred to as the "Principle Axes" (PA) method and the covariance method. The Principle Axes method uses the Eigenvalues and Eigenvectors of the covariance (error) matrix by adding a displacement vector to the set of best fit coefficients. Given Eigenvalues λ_i and Eigenvectors

$\vec{r}_i$ of a covariance matrix, we can compute a displacement vector along a principle axis $\delta\vec{a}_i$ by choosing

$$\delta\vec{a}_i = \lambda_i^{\frac{1}{2}}\vec{r}_i\,.$$

Choosing displacements along these principle axes results in a set of errors that are uncorrelated. For the set of best fit parameters $\vec{a}$, we can then use these displacements to calculate an uncorrelated error on an observable:

$$\delta\mathcal{O}_i = \left|\mathcal{O}(\vec{a}) - \mathcal{O}(\vec{a} \pm \delta\vec{a}_i)\right|\,.$$

Summing the $\delta\mathcal{O}_i$ in quadrature yields the total error on observable $\mathcal{O}$.

Alternatively, it is often easier to generate random sets of parameters that respect the correlations between the parameters in question. This is what we refer to as the covariance method. With the covariance method, random displacement vectors $\delta\vec{a}_i'$ are drawn. The error on an observable $\mathcal{O}$ is then just the standard deviation of the errors from these randomly generated displacement vectors:

$$\delta\mathcal{O}^2 = \frac{1}{N}\sum_i^N \left(\mathcal{O}(\vec{a}) - \mathcal{O}(\vec{a} \pm \delta\vec{a}_i')\right)^2\,.$$

If the errors are Gaussian, then both the principle axes and the covariance method should give identical answers.

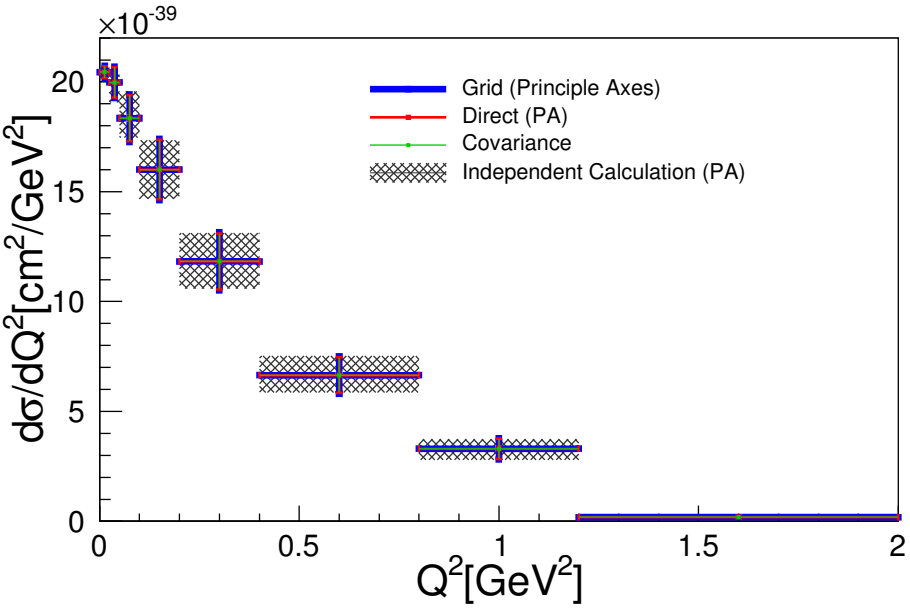

Figure 2.11: Plot to demonstrate consistency of various reweighting routines for determining errors on z expansion. Descriptions of the reweighting routines are given in the text. Plotted are the free-nucleon differential cross section and errors as a function of Q^2. The plot shows consistency between errors computed from varying z expansion parameters on a grid (blue), reweighting directly to the principle axes of the covariance matrix (red), and randomly sampling around a nominal value while respecting correlations between parameters (green). These are compared to an independent calculation (black hash).

CHAPTER 3

STAGGERED QUARKS IN LATTICE QCD

3.1 Staggered Quarks

3.1.1 Notation

In the following, it will be useful to define some notation. We assume that all quantities have been scaled by the lattice spacing a to make them dimensionless. The lattice sites x_μ are confined to a periodic lattice, and we will take x_μ to be integer values in the set

$$x_\mu \in \{0, \ldots, N-1\} \tag{3.1}$$

for $N = L/a$ with lattice box size L. The staggered phases are functions that take the values ± 1 and are conventionally defined by

$$\eta_\mu(x) = (-1)^{\sum_{\nu<\mu} x_\nu}, \quad \zeta_\mu(x) = (-1)^{\sum_{\nu>\mu} x_\nu}, \quad \epsilon(x) = (-1)^{\sum_\nu x_\nu}\,. \tag{3.2}$$

We work with gamma matrices defined to satisfy the commutation relation $\left\{\gamma_\mu, \gamma_\nu\right\} = 2\delta_{\mu\nu}$.

We will often need to use indices that correspond to the corners of a unit cube. In such cases, the indices will be referred to as "taste indices" and are labeled with capital Roman letters. These indices take values in the range $\{0, \ldots 7\}$. It is useful to use these interchangeably with "vectorized" taste indices, which are the binary digits of the taste index A, written as a three-vector. Defined precisely, we may write the vectorized version of taste index A as

$$\vec{A} = (\text{Mod}[A, 2],\, \text{Mod}[\text{Floor}[A/2], 2],\, \text{Floor}[A/4])\ , \tag{3.3}$$

with $\vec{A}_i \in \{0, 1\}$. In four dimensions, the taste indices instead take values in the range

$\{0, \ldots 15\}$ and the vectorized indices are

$$\vec{A} = (\text{Mod}[A, 2],\ \text{Mod}[\text{Floor}[A/2], 2],\ \text{Mod}[\text{Floor}[A/4], 2],\ \text{Floor}[A/8])\ , \tag{3.4}$$

again with $\vec{A}_\mu \in \{0, 1\}$.

3.1.2 Spin-Taste Basis in the Naive Action

It is helpful to understand how the naive quarks are connected to the staggered quarks. The naive quark free-field action on the lattice is

$$S = \sum_{x,y} \overline{\psi}(x) \left[\sum_\mu \gamma_\mu \left(\delta_{x,y-\hat{\mu}} - \delta_{x,y+\hat{\mu}} \right) + m\delta_{x,y} \right] \psi(y)\,. \tag{3.5}$$

This action has the discrete analogues of continuum symmetries (where R_{12}, R_{13}, and R_{23} are taken as generators of the rotation subgroup) [56],

$$\begin{aligned} &\text{Translation } T_\mu\text{:} && \psi(x) \to \psi(x + \hat{\mu}) \\ &\text{Rotation } R_{ij}\text{:} && \psi(x) \to \tfrac{1}{\sqrt{2}} \left(\mathbb{1} + \gamma_i \gamma_j \right) \psi(R_{ij}^{-1} x) \\ &\text{Spatial Inversion } I_s\text{:} && \psi(x) \to \gamma_4 \psi(I_s x)\,, \end{aligned} \tag{3.6}$$

as well as a charge conjugation symmetry, which can be ignored for the work in this thesis. We assume the rotations are about axes that pass through the origin. Because of the fermion doubling, we have additional site-dependent taste symmetries belonging to the discrete Clifford group Γ_4. The representation matrices are [57]

$$B_\mu(x) = \gamma_\mu \gamma_5 (-1)^{x_\mu}, \quad B_5(x) = i\gamma_5 \epsilon(x), \quad B_\mu(x) B_\nu(x), \quad B_\mu(x) B_5(x)\,. \tag{3.7}$$

The presence of these taste symmetries permits diagonalization of the action in spin-taste

space. To demonstrate this, we define the Kawamoto-Smit matrix [58]

$$\Omega(x) = \gamma_1^{x_1}\gamma_2^{x_2}\gamma_3^{x_3}\gamma_4^{x_4} \tag{3.8}$$

and perform a change of variables on our quark field:

$$\Psi(x) = \Omega(x)X(x)\,. \tag{3.9}$$

Under this change of variables, the action becomes diagonal in its spinor indices:

$$S = \sum_{x,y}\overline{X}(x)\left[\sum_{\mu}\eta_\mu(x)\left(\delta_{x,y-\hat{\mu}} - \delta_{x,y+\hat{\mu}}\right) + m\delta_{x,y}\right]X(y)\,. \tag{3.10}$$

In this form, the action leaves the entries of the vector X invariant, meaning that propagation of states under this action cannot mix the four components of the spinors X and $\overline{X}$. The Dirac matrix structure is encoded in the relative signs of neighboring sites through the staggered phase η instead of explicitly permuting the indices of the spinors.

To see how the spin structure of staggered quarks is connected to the naive quark spinors, consider a quark bilinear with some Dirac matrix structure Γ given by

$$\mathcal{V}_\Gamma(x,y) = \sum_{\alpha\beta}\overline{\psi}_\alpha(x)\Gamma_{\alpha\beta}\psi_\beta(y)\,, \tag{3.11}$$

where α and β are spinor indices. This expression may be recast as a trace,

$$\mathcal{V}_\Gamma(x,y) = -\mathrm{Tr}\left[\Gamma_{\alpha\beta}\psi_\beta(y)\overline{\psi}_\alpha(x)\right]\,. \tag{3.12}$$

The spinor combination $\psi_\beta\overline{\psi}_\alpha$ makes up a 4×4 matrix, where the 16 entries are determined by the components of the two spinors. The trace is nonvanishing only when the

spinor components give a term proportional to $\Gamma^\dagger$, because

$$\mathrm{Tr}\left[\Gamma\Gamma'^\dagger\right] = 0 \tag{3.13}$$

when $\Gamma' \neq \Gamma$. This condition motivates a change of basis to

$$\psi(y)\overline{\psi}(x) \to \frac{1}{4}\sum_{AB} \chi_{A+B}(y)\overline{\chi}_A(x)\,\Omega(y)\widehat{\Xi}^\dagger_B\Omega^\dagger(x)\,, \tag{3.14}$$

where the indices A and B take values from 1 to 16. The Kawamoto-Smit Ω matrices have been inserted to make the staggered fermion basis manifest. Despite the appearance of the staggered fields χ and $\overline{\chi}$, this still has as many degrees of freedom as the left side due to the taste index A.

The $\widehat{\Xi}_B$ are the 16 independent combinations of Dirac matrices, related to what is conventionally considered the taste matrix by a permutation of indices that depends on the spin matrix,

$$\widehat{\Xi}_B = \mathcal{O}^\Gamma_{BC}\Xi_C\,. \tag{3.15}$$

The permutation is inserted only to make the definition of Ξ_C consistent for all spin matrices Γ, since the same quark displacement $y-x$ does not always correspond the same taste matrix Ξ. It is simplest to figure out which Ξ will be nonvanishing by first fixing $y-x$ and Γ. The nonvanishing Ξ is then proportional to the combination of gamma matrices obtained from the product

$$\Omega^\dagger(y)\Gamma\Omega(x) \sim \Gamma\Omega(y-x)\,. \tag{3.16}$$

The next task is to remove the redundant spin-taste index A. The way to do this is to define the sites on a coarser grid with lattice spacing $2a$, labeled by $\tilde{x}$, which coincide with every other site throughout the lattice. The sites of the finer lattice are then described by this site on the coarser lattice plus some index within a cube. The taste indices are forced

to coincide with the unit cube index with the relation

$$\vec{A} = x - \tilde{x}\,, \tag{3.17}$$

so that the spin and taste degrees of freedom are mapped onto the sites. This projection is made by the assignment

$$\chi_A(\tilde{x} + \vec{C}) = \chi(\tilde{x} + \vec{A})\delta_{AC} = \chi(x)\,, \tag{3.18}$$

which fixes the 16×16 object $\chi_A(\tilde{x} + \vec{C})$ to be confined to only its 16 diagonal elements. A similar constraint is imposed on y and B such that

$$\vec{B} = y - x\,. \tag{3.19}$$

This removes a factor of 16 degrees of freedom, or a factor of 4 degrees of freedom for each spinor in Eq. (3.14).

With this projection, construction of a spin-taste operator in general requires the use of nonlocal operators. The spin-taste index on the staggered quark operators may be dropped and the quark bilinear becomes

$$\mathcal{V}_\Gamma(x, x + \vec{B}) = \frac{1}{4}\sum_{BC} \overline{\chi}(x)\chi(x + \vec{B})\mathcal{O}^\Gamma_{BC}\mathrm{Tr}\left[\Gamma\,\Omega(x + \vec{B})\Xi^\dagger_C\Omega^\dagger(x)\right]\,. \tag{3.20}$$

with the same trace factor that is obtained from quark bilinears written in the spin-taste basis representation [59–61]. Evaluation of the trace gives back the staggered phase for the desired spin-taste current,

$$\frac{1}{4}\mathrm{Tr}\left[\Gamma\,\Omega(y)\Xi^\dagger_C\Omega^\dagger(x)\right] \equiv \alpha_C^{\Gamma\otimes\Xi}(x)\,. \tag{3.21}$$

3.1.3 Quark Taste Projections

To match the diagonalization of the action in Sec. 3.1.2, we choose a set of symmetry operations that are also diagonal in spinor indices. These operations are a combination of the discrete transformations listed in Eq. (3.6) and the taste transformations in Eq. (3.7). For instance, rather than discrete translations we use shifts defined by

$$\begin{aligned} \psi(x) &\to B_{T_\mu}(x)\psi(x+\hat{\mu}) \\ \implies \Omega(x)X(x) &\to B_{T_\mu}(x)\Omega(x+\hat{\mu})X(x+\hat{\mu}) \\ &= \left[B_{T_\mu}(x)\Omega(x+\hat{\mu})\Omega^{-1}(x)\right]\Omega(x)X(x+\hat{\mu})\,. \end{aligned} \tag{3.22}$$

The quantity in square brackets becomes the identity times some site-dependent phase if we choose

$$B_{T_\mu}(x) = -iB_\mu(x)B_5(x) = \eta_\mu(x)\zeta_\mu(x)\gamma_\mu\,, \tag{3.23}$$

which replaces Eq. (3.22) by the diagonal shift operation

$$X(x) \to \zeta_\mu(x)X(x+\hat{\mu})\,. \tag{3.24}$$

A similar approach for the rotations yields the naive quark transformation

$$\begin{aligned} \psi(x) &\to \frac{1}{\sqrt{2}}B_{R_{ij}}(x)\left(\mathbb{1}+\gamma_i\gamma_j\right)\psi(R_{ij}^{-1}x) \\ \implies \Omega(x)X(x) &\to \frac{1}{\sqrt{2}}B_{R_{ij}}(x)\left(\mathbb{1}+\gamma_i\gamma_j\right)\Omega(R_{ij}^{-1}x)X(R_{ij}^{-1}x) \\ &= \left[\frac{1}{\sqrt{2}}B_{R_{ij}}(x)\left(\mathbb{1}+\gamma_i\gamma_j\right)\Omega(R_{ij}^{-1}x)\Omega^{-1}(x)\right]\Omega(x)X(R_{ij}^{-1}x)\,. \end{aligned} \tag{3.25}$$

Choosing

$$B_{R_{ij}}(x) = \frac{1}{\sqrt{2}}\left[\mathbb{1}+B_i(x)B_j(x)\right] = \frac{1}{\sqrt{2}}\left[\mathbb{1}-(-1)^{x_i+x_j}\gamma_i\gamma_j\right] \tag{3.26}$$

and defining $S_{R_{ij}}(x)$ as the phase found in the expression (with the sign $\pm$ determined by the ordering $(i \lessgtr j)$)

$$\begin{aligned} S_{R_{ij}}(x)\mathbb{1} &= \frac{1}{\sqrt{2}}\left[B_{R_{ij}}(x)\left(\mathbb{1}+\gamma_i\gamma_j\right)\Omega(R_{ij}^{-1}x)\Omega^{-1}(x)\right] \\ &= \frac{1}{2}\left[1+\eta_i(x)\eta_j(x)\zeta_i(x)\zeta_j(x) \pm \left(\zeta_i(x)\zeta_j(x)-\eta_i(x)\eta_j(x)\right)\right]\mathbb{1} \end{aligned} \tag{3.27}$$

gives the staggered rotation symmetry transformation

$$X(x) \to S_{R_{ij}}(x)X(R_{ij}^{-1}x)\,. \tag{3.28}$$

S_R in Eq. (3.27) matches the rotation factor derived from the action in Ref. [62].

At this point, a digression is in order. In a continuum theory with no doublers, the expectation is that fermions that undergo a 2π rotation will transform back to themselves with a relative factor of -1, indicating that they are in representations of the double cover of the rotation group. This may be easily checked by applying the rotations from Eq. (3.6), which gives the gamma factor

$$\frac{1}{4}\left(\mathbb{1}+\gamma_i\gamma_j\right)^4 = -\mathbb{1}\,. \tag{3.29}$$

In contrast, application of the staggered rotation four times gives

$$S_{R_{ij}}(x)S_{R_{ij}}(R_{ij}^{-1}x)S_{R_{ij}}(R_{ij}^{-2}x)S_{R_{ij}}(R_{ij}^{-3}x) = 1\,. \tag{3.30}$$

This apparent contradiction is the result of the simultaneous taste and rotation transformations. The continuum $\frac{1}{\sqrt{2}}\left(\mathbb{1}+\gamma_i\gamma_j\right)$ factor is always paired with a factor of $B_{R_{ij}}(x) \sim \frac{1}{\sqrt{2}}\left(\mathbb{1}\pm\gamma_i\gamma_j\right)$, either cancelling or squaring the gamma rotation factor. We say that the double cover has been absorbed by the fermion taste transformations, and is expressed by the shifts through their anticommutation:

$$\left\{S_\mu, S_\nu\right\} = 0 \quad (\mu \neq \nu)\,. \tag{3.31}$$

With the choice of symmetry operators outlined in this section, the four components of the spinor $X(x)$ are connected only by pure taste transformations and are redundant. The pure taste symmetry transformations are removed by projecting out all but one spinor component. This simplification is applied for practical purposes, since removing the redundant degrees of freedom reduces the computing time needed to perform calculations of observables.

3.1.4 Staggered Quark Group Theory

Though the symmetry group of the full lattice includes four spacetime dimensions, this is not practical computations of observables in lattice QCD. Extending operators over multiple timeslices introduces unwanted contact terms and the operator has a more complicated behavior under the Hamiltonian time evolution. Instead, the operators are restricted to a single timeslice in a spatial subgroup of the full spacetime symmetry group. This is similar to the reduction of the continuum Lorentz group to only its non-relativistic spatial translation and rotation subgroup.

With three spacetime dimensions, the staggered quarks transform under the "Geometric Timeslice" (GTS) group, given by

$$\mathrm{GTS} = (((\mathcal{T}_M \times \mathbb{Q}_8) \rtimes W_3) \times D_4)/\mathbb{Z}_2\,, \tag{3.32}$$

where the definitions of the factors are given below. This is the same group that appears in Refs. [56, 63], but with the additional observation that SW_4 can be represented as the semi-direct product $\mathcal{Q}_8 \rtimes SW_3$. Since the rotations and taste changes each belong to subgroups that only intersect for the identity element, proving this semi-direct product amounts only to showing that there exists a group homomorphism defined by

$$\phi : SW_3 \to \mathrm{Aut}(\mathcal{Q}_8) \tag{3.33}$$

and that $\mathcal{Q}_8$ is a normal subgroup of SW_4. Apart from the elements in the center of $\mathcal{Q}_8$,

$$R_i^{-1}\left(\pm\mathbb{1}\right)R_i = \pm\mathbb{1}\,, \tag{3.34}$$

both requirements are satisfied by the equation

$$R_i^{-1}\left(\pm\Xi_{jk}\right)R_i = \pm\epsilon_{jkm}\Xi_{km} \pm \delta_{ij}\Xi_{jk}\,,\ (i\neq k, j\neq k)\,. \tag{3.35}$$

Eqs. (3.34)–(3.35) together give a mapping $\mathcal{Q}_8 \to \mathcal{Q}_8$ defining an automorphism and showing that the elements of $\mathcal{Q}_8$ form a normal subgroup. We can then define the homomorphism

$$\phi_R(\Xi) \equiv R^{-1}\Xi R \tag{3.36}$$

that preserves the group structure:

$$\phi_{R_1}(\phi_{R_2}(\Xi)) = R_2^{-1}R_1^{-1}\Xi R_1 R_2 = \phi_{R_1R_2}(\Xi)\,. \tag{3.37}$$

The factors in the GTS group may be understood as follows:

$\mathcal{T}_M$: (Abelian $(\mathbb{Z}_N)^3$) Lattice translation symmetry,

$\mathbb{Q}_8$: (Order 8 Quarternions) Discrete taste transformations Ξ_{ij},

W_3 : (Order 24 Octahedral) Lattice rotational symmetry and spatial inversion,

$\mathbb{D}_4$: (Order 8 Dihedral) Discrete taste transformations Ξ_4, Ξ_{123}.

The only effect of the $\mathbb{Z}_2$ quotient is to equate the negative identity element from both group factors ($\mathbb{Q}_8 \rtimes W_3$ and D_4), which forbids irreducible representations that are the product of a fermionic and bosonic representation.

The order of this group is in fact larger than the true lattice symmetry group by a factor of 8. The reason for this is that we have double counted the momenta from the corners

of the Brillouin zone by separating the single site translations T_i from the discrete taste transformations Ξ_i. One could try to carefully treat the shift symmetries, in which case the lattice symmetry group is formally an extension[1] of the zero momentum group by $(\mathbb{Z}_N)^3$. The irreps one gets from a proper treatment of the shift symmetries are nearly identical to the irreps one gets from the enlarged, tractable group if one neglects the irreps that have more than half the maximum lattice momentum. The only exception is in how the irreps with half the maximum momentum are handled, which are not necessary for understanding lattice computations with small momenta (in lattice units).

The irreps of the semidirect product in this group can be determined by applying Wigner's little group analysis for the discrete groups. The process can be summarized as follows:

1. Compute the irreducible representations of the group $\mathbb{Q}_8$.
2. Organize the irreps of $\mathbb{Q}_8$ into orbits under action of W_3.
3. Compute the subset of group transformations that leave the irrep of $\mathbb{Q}_8$ invariant. This is known as the little group.
4. Compute the irreps of the little group.

We may then classify the irreducible representations of the semidirect product group by their representations under the subgroups. The dimension of the irrep is then the product of the dimensions of the irreps of the subgroups times the size of the orbit implied in step 2. For nonzero momentum, the translation subgroup must also be included in the semidirect product. This construction is presented in detail in Appendix A.

Baryon wavefunctions in the continuum theory must have overall antisymmetric wavefunctions because they are fermions. The part of the wavefunction corresponding to color is

1. Extension groups are in general difficult to determine, but methods exist for computing the irreducible representations of certain extension groups. The lattice shift symmetry group that appears as a result of extension depends on the prime factors of the lattice dimensions and must be treated separately for several distinct cases. For the simplest case (a 4^3 lattice), the resulting group is nontrivial and has no conventional name.

purely asymmetric because it must be an $SU(3)$ color singlet constructed from three quarks, and antisymmetrization with the Levi-Civita epsilon tensor is the only construction that satisfies these requirements. As a consequence, creating an overall antisymmetric wavefunction amounts to finding an overall symmetric wavefunction in every quantum number except color.

To determine the symmetric part of the baryon wavefunctions, it helps to embed the lattice subgroup into a larger subgroup that is more tractable. In the continuum, the embedding is the $SU(6)$ quark model that symmetrizes over flavor and spin:

$$SU(2)_S \times SU(3)_F \subset SU(6)_{SF} \tag{3.38}$$

where S and F stand for spin and flavor, respectively. For the GTS group, there is an additional taste symmetry that must be included. Each of the factors $\mathbb{Q}_8$, SW_3 (rotations without spatial inversion), and D_4 may be separately embedded in an $SU(2)$ group, simplifying the interpretation of restoration of symmetry in the continuum limit by the embedding

$$[D_4 \times (\mathbb{Q}_8 \rtimes SW_3)] \subset [SU(2)_{T1} \times SU(2)_{T2} \times SU(2)_S] \subset [SU(4)_T \times SU(2)_S] \,, \tag{3.39}$$

where T stands for taste. The quark flavor may also be symmetrized, meaning that the full embedding is

$$SU(2)_S \times SU(3)_F \times SU(4)_T \subset SU(24)_{SFT} \,. \tag{3.40}$$

By studying how the embedding group breaks down to various subgroups, one can deduce the particle content of the lattice irreducible representations. This procedure was carried out in Ref. [64] and will be summarized here.

The quark objects transform under the fundamental representation of the symmetry group. Here, they transform under the 24 representation of $SU(24)$. Finding a symmetric representation of three quarks in $SU(24)$ amounts to symmetrizing over the indices of three

quarks, which yields the 2600_S of $SU(24)$, where 2600 is the dimension of the irreducible representation and the subscript S denotes that the representation is overall symmetric. The representations that map onto nucleon states and Δ states have different spins, so the first step is to decompose the $SU(24)$ irreps under the spin $\times$ flavor-taste subgroup:

$$\begin{aligned} SU(24)_{SFT} &\to SU(2)_S \times SU(12)_{FT}\,, \\ 2600_S &\to (4_S \otimes 364_S) \oplus (2_M \otimes 572_M)\,, \end{aligned} \tag{3.41}$$

where again the numbers denote the dimensions of the irreps and the subscript M denotes a representation of mixed symmetry. The symmetric representations here correspond to states whose masses and matrix elements tend, in the continuum limit, to those of the Δ baryon, and the mixed representations correspond to those states that tend to the nucleon mass.

Next, the $SU(12)_{FT}$ group must be decomposed into its subgroups. The $SU(12)_{FT}$ subgroup is reduced to $SU(8)_{ud} \times SU(4)_s$, allowing study the decomposition of the irreps into representations with different strangeness. In nature, the strange quark has a mass that is approximately 27 times the average mass of the up and down quarks. The decomposition is completed by separating the $SU(8)_{ud}$ subgroup into taste and isospin (strangeness), leading to $SU(4)_{ud} \times SU(4)_s \times SU(2)_I$, and then taking the diagonal taste subgroup $SU(4)_{ud} \times SU(4)_s \to SU(4)_T \times U(1)_s$.

Representations transforming under the overall symmetric 20_S representation of this $SU(4)_T$ factor will have the same spin-flavor structure in the continuum limit as the physical baryons, and are expected to reproduce the physical baryon spectrum. Since the continuum limit restores the symmetry group to $SU(8) \times SU(4)$, the representations of $SU(2)_I \times SU(4)_T$ that result from decomposing $SU(8) \times SU(4)$ representation will have identical masses in the continuum limit. It is possible to use this observation to identify the expected continuum

masses and matrix elements of the representations. The result of this procedure gives

$$\begin{aligned} SU(12)_{FT} &\to SU(8)_{ud} \times SU(4)_s \,, \\ 364_S &\to (120_S \otimes 1)_0 \oplus (36_S \otimes 4)_{-1} \oplus (8 \otimes 10_S)_{-2} \oplus (1 \otimes 20_S)_{-3} \,, \\ 572_M &\to (168_M \otimes 1)_0 \oplus (36_S \otimes 4)_{-1} \oplus (28_A \otimes 4)_{-1} \\ &\quad \oplus (8 \otimes 6_A)_{-2} \oplus (8 \otimes 10_S)_{-2} \oplus (1 \otimes 20_M)_{-3} \,, \end{aligned} \tag{3.42}$$

where the subscript on the representations denotes the strangeness.

For the purposes of this project, we are interested only in the operators that have zero strangeness, that is, only the operators that create nucleons. Continuing the decomposition to completion for these representations,

$$\begin{aligned} SU(8)_{ud} \times SU(4)_s &\to SU(2)_I \times SU(4)_T \times U(1)_s \,, \\ (120_S \otimes 1)_0 &\to (4_S \otimes 20_S)_0 \oplus (2_M \otimes 20_M)_0 \,, \\ (168_M \otimes 1)_0 &\to (4_S \otimes 20_M)_0 \oplus (2_M \otimes 20_S)_0 \oplus (2_M \otimes 20_M)_0 \oplus (2_M \otimes 4_A)_0 \,. \end{aligned} \tag{3.43}$$

Both representations contain a 20_S of $SU(4)_T$, indicating that all operators transforming under either representation in Eq. (3.43) will generate baryons with physical masses in the continuum limit. The former irrep in Eq. (3.43), the $(120_S \otimes 1)_0$, was found by decomposing the symmetric representation of $SU(12)_{FT}$. Since the symmetric representation is paired with the spin $\frac{3}{2}$ representation of $SU(2)_S$ in Eq. (3.41), all operators that transform under the $(120_S \otimes 1)_0$ will form spin $\frac{3}{2}$ baryons, or Δ baryons. However, unlike the physical world, Eq. (3.43) indicates that baryons transforming with spin $\frac{3}{2}$ and isospin $\frac{1}{2}$ may be formed in addition to baryons with spin $\frac{3}{2}$ and isospin $\frac{3}{2}$. This is a consequence of allowing the operators to be symmetrized over taste as well as spin and isospin. For this reason, the operators transforming under the spin $\frac{3}{2}$ representation of $SU(2)_S$ are all referred to as Δ-like. A similar argument may be made for the latter irrep in Eq. (3.43), the $(168_M \otimes 1)_0$

irrep, which transforms under the spin $\frac{1}{2}$ and creates states that are referred to as N-like.

From here, the lattice operators may be deduced by applying Eq. (3.39) in reverse. The simplest way to determine the multiplicities of the lattice irreducible representations is to break $SU(4)_T$ to $SU(2)_{T1} \times SU(2)_{T2}$ first, giving

$$\begin{aligned} SU(4)_T &\to SU(2)_{T1} \times SU(2)_{T2}\,, \\ 20_S &\to (4_S \otimes 4_S) \oplus (2_M \otimes 2_M)\,, \\ 20_M &\to (4_S \otimes 2_M) \oplus (2_M \otimes 4_S) \oplus (2_M \otimes 2_M)\,, \\ 4_A &\to (2_M \otimes 2_M)\,. \end{aligned} \tag{3.44}$$

The representations must be subduced down to the discrete lattice subgroups to complete the analysis. There exist shortcuts that allow determination of the irreducible representations without going to great lengths. Because of the $\mathbb{Z}_2$ quotient factor in the GTS group, Eq. (3.32), baryonic operators may only be constructed from fermionic representations of D_4. This means that there is only one possible irreducible representation for the representations to subduce to, namely a two-dimensional representation:

$$\begin{aligned} SU(2)_{T1} &\to D_4\,, \\ 4_S &\to 2 \oplus 2\,, \\ 2_M &\to 2\,. \end{aligned} \tag{3.45}$$

Any irreducible representation that transforms in the 4_S irrep of $SU(2)_{T1}$ simply gives two copies of the same representations as the 2_M irrep.

The semi-direct product of Eq. (3.32) complicates the subduction of $SU(2)_{T2} \times SU(2)_S$, but not too much. It helps to note the tautology that when restricting to the subgroup $\mathbb{Q}_8 \rtimes SW_3 \to SW_3$, the orbits of the representations of $\mathbb{Q}_8$ transform as representations of SW_3. This means that the restriction to the SW_3 subgroup of $\mathbb{Q}_8 \rtimes SW_3$ yields irreps in a diagonal

subgroup, $[SW_3]_{\text{diag}}$. The continuum group $SU(2)_{T2} \times SU(2)_S$ equivalently restricts to $[SU(2)]_{\text{diag}}$. It is simpler to compute the subduction from $[SU(2)]_{\text{diag}}$ to $[SW_3]_{\text{diag}}$ and the restriction from $\mathbb{Q}_8 \rtimes SW_3$ to $[SW_3]_{\text{diag}}$ than it is to subduce directly from $SU(2)_{T2} \times SU(2)_S$ to $\mathbb{Q}_8 \rtimes SW_3$.

There are three fermionic representations of $\mathbb{Q}_8 \rtimes SW_3$, which restrict to

$$\begin{aligned} \mathbb{Q}_8 \rtimes SW_3 &\to [SW_3]_{\text{diag}} \,, \\ 2 \otimes 2 &\to A_1 \oplus T_1 \,, \\ 2 \otimes \bar{2} &\to A_2 \oplus T_2 \,, \\ 2 \otimes 4 &\to E \oplus T_1 \oplus T_2 \,. \end{aligned} \tag{3.46}$$

Forming $D_4 \times (\mathbb{Q}_8 \rtimes SW_3)$ in the GTS group, one obtains the 8, $8'$, and 16 representations, respectively. The subduction from $SU(2)_{T2} \times SU(2)_S$ to $[SW_3]_{\text{diag}}$ gives

$$\begin{aligned} SU(2)_{T2} \times SU(2)_S &\to [SU(2)]_{\text{diag}} \,, \\ 2 \otimes 2 &\to 3 \oplus 1 \,, \\ 2 \otimes 4 &\to 5 \oplus 3 \,, \\ 4 \otimes 4 &\to 7 \oplus 5 \oplus 3 \oplus 1 \end{aligned} \tag{3.47}$$

and we may deduce from computing the product tables of all of the representations that [56]

$$\begin{aligned} [SU(2)]_{\text{diag}} &\to [SW_3]_{\text{diag}} \,, \\ 1 &\to A_1 \,, \\ 3 &\to T_1 \,, \\ 5 &\to E \oplus T_2 \,, \\ 7 &\to (A_2 \oplus T_1 \oplus T_2) \,. \end{aligned} \tag{3.48}$$

$SU(2)_S \times SU(4)_T$	GTS
$4_S \otimes 20_S$	$2 \cdot 8 \oplus 2 \cdot 8' \oplus 3 \cdot 16$
$4_S \otimes 20_M$	$1 \cdot 8 \oplus 1 \cdot 8' \oplus 4 \cdot 16$
$4_S \otimes 4_A$	$0 \cdot 8 \oplus 0 \cdot 8' \oplus 1 \cdot 16$
$2_M \otimes 20_S$	$1 \cdot 8 \oplus 0 \cdot 8' \oplus 2 \cdot 16$
$2_M \otimes 20_M$	$3 \cdot 8 \oplus 0 \cdot 8' \oplus 1 \cdot 16$
$2_M \otimes 4_A$	$1 \cdot 8 \oplus 0 \cdot 8' \oplus 0 \cdot 16$

Table 3.1: Summary of subduction of irreducible representations from the continuum group to GTS [64]. All of the 4_S representations of $SU(2)_S$ correspond to Δ-like baryons, and all of the 2_M representations correspond to N-like baryons. Note that the flavor (isospin) symmetry group is not considered in this table.

GTS	$I = \frac{3}{2}$	$I = \frac{1}{2}$
8	$3N + 2\Delta$	$5N + 1\Delta$
$8'$	$0N + 2\Delta$	$0N + 1\Delta$
16	$1N + 3\Delta$	$3N + 4\Delta$

Table 3.2: Summary of the multiplicities of taste states in the irreducible representations of $SU(2)_I \times$ GTS [64]. These states belong to the lowest-order multiplet. Each excitation of a physical nucleon and delta will also have its own multiplet of baryon taste states.

The combination of all of these decompositions is summarized in Table 3.1.

The irreps must be classified by which representation of $SU(2)_I \times$ GTS they belong to, corresponding to either isospin $\frac{3}{2}$ or $\frac{1}{2}$. Furthermore, the states that belong to the $(120_S \otimes 1)_0$ irrep all give Δ-like baryon states, and the states that belong to the $(168_M \otimes 1)_0$ irrep give N-like states. By revisiting Eq. (3.43), we can use Table 3.1 to compute the multiplicity of the baryon tastes of each particle type in each irrep. These taste multiplicities are listed in Table 3.2.

3.2 Staggered Quark Operators

3.2.1 Staggered Quark Propagator

The baryon operators are tied up by computing propagators, formed from contracting a quark and an antiquark operator into

$$\overbrace{\chi^a(y)\overline{\chi}^b}(z) = \Big[G^{ab}(y,z)\Big]^{-1} \,. \tag{3.49}$$

Solving for the free-field staggered quark propagator is not as straightforward as for the continuum propagator. The solution requires special treatment of the phases to deal with the site dependence of the taste components. The quark propagators are the inverse of the action,

$$S = \sum_{x,y} \overline{\chi}(x) \left[\frac{1}{2} \sum_{\mu} \eta_\mu(x) \left(\delta_{x,y-\hat{\mu}} - \delta_{x,y+\hat{\mu}} \right) + ma\, \delta_{x,y} \right] \chi(y) \,. \tag{3.50}$$

determined by solving for the Green's function

$$\sum_y \left(\not{D} + m \right)_{x,y} G(y,z) = \delta_{x,z} \,, \tag{3.51}$$

where x, y, and z are lattice sites and the color indices have been dropped.

Fourier transforming Eq. (3.51) gives

$$\begin{aligned} e^{-ik\cdot z} &= \sum_{xy} \left[\frac{1}{2} \sum_{\mu} \eta_\mu(x) \left(\delta_{x,y-\hat{\mu}} - \delta_{x,y+\hat{\mu}} \right) + ma\, \delta_{x,y} \right] e^{-ik\cdot x} G(y,z) \\ &= \sum_y e^{-ik\cdot y} \left[\frac{1}{2} \sum_{\mu} \eta_\mu(y) \left(e^{+ik_\mu a} - e^{-ik_\mu a} \right) + ma \right] G(y,z) \\ &= \sum_y e^{-ik\cdot y} \left[i \sum_{\mu} \eta_\mu(y) \sin(k_\mu a) + ma \right] G(y,z) \,, \end{aligned} \tag{3.52}$$

with $-\pi/2 \leq k_\mu < 3\pi/2$.

It is easier to solve for the propagator if the staggered phases and the unit cube sites are

factored out the momenta and sites. To do this, define the Brillouin zone momenta

$$(\Pi_B)_\nu = \begin{cases} \pi/a & B_\nu = 1 \\ 0 & B_\nu = 0 \end{cases}, \tag{3.53}$$

where B is a taste index in four dimensions, and

$$\left(\Pi_{\eta_\mu}\right)_\nu = \begin{cases} \pi/a & \nu < \mu \\ 0 & \nu \geq \mu \end{cases}. \tag{3.54}$$

Then define tilde variables such that $k_\mu = \tilde{k}_\mu + (\Pi_B)_\mu$ and $y = \tilde{y} + \vec{A}$. When this is done, the staggered phase can be written as a momentum contribution by replacing

$$\eta_\mu(\tilde{y} + \vec{A}) = e^{-i\Pi_{\eta\mu}\cdot\vec{A}}, \tag{3.55}$$

and the sine function may be written

$$\sin(k_\mu a) = \sin(\tilde{k}_\mu a + (\Pi_B)_\mu a) = (-1)^{B_\mu}\sin(\tilde{k}_\mu a) \tag{3.56}$$

where the tilde denotes that $-\pi/2 \leq \tilde{k}_\mu < \pi/2$. The last change to make is to replace G with its Fourier transform

$$G(y,z) = \frac{1}{V^2}\sum_{\tilde{p}\tilde{p}'} e^{+i(\tilde{p}+\Pi_C)\cdot(\tilde{y}+\vec{A})} e^{+i(\tilde{p}'+\Pi_{C'})\cdot(\tilde{z}+\vec{D})} G^{CC'}(\tilde{p},\tilde{p}') \tag{3.57}$$

Applying these changes, Eq. (3.57) takes the form

$$
\begin{aligned}
&e^{-i(\tilde{k}+\Pi_B)\cdot z} \\
&= \frac{1}{V^2} \sum_{\tilde{y}\tilde{p}\tilde{p}'} \sum_{ACC'} \Bigg[i \sum_{\mu} e^{-i(\tilde{k}-\tilde{p})\cdot(\tilde{y}+\vec{A})} e^{-i(\Pi_B+\Pi_C+\Pi_{\eta\mu})\cdot\vec{A}} (-1)^{B_\mu} \sin(\tilde{k}_\mu a) \\
&+ e^{-i(\tilde{k}-\tilde{p})\cdot(\tilde{y}+\vec{A})} e^{-i(\Pi_B+\Pi_C)\cdot\vec{A}}\, ma \Bigg] \\
&\times e^{+i(\tilde{p}'+\Pi_{C'})\cdot(\tilde{z}+\vec{D})} G^{CC'}(\tilde{p},\tilde{p}')\,.
\end{aligned}
\tag{3.58}
$$

The terms have been grouped by how they combine together. The first reduction that can be done is to complete the sum over $\tilde{y}$, which reduces one of the exponentials to

$$
\sum_{\tilde{y}} e^{-i(\tilde{k}-\tilde{p})\cdot(\tilde{y}+\vec{A})} = \frac{V}{16}\, \delta_{\tilde{k}\tilde{p}} e^{-i(\tilde{k}-\tilde{p})\cdot\vec{A}}\,. \tag{3.59}
$$

After evaluating the δ function, the remaining exponential becomes unity, so the term will be dropped. The next exponentials to reduce are the taste terms

$$
\sum_{A} e^{-i(\Pi_B+\Pi_C+\Pi_{\eta\mu})\cdot\vec{A}} = 16\, \delta_{B,C+\eta_\mu} \tag{3.60}
$$

where the shorthand $\eta_\mu = \frac{a}{\pi}\Pi_{\eta_\mu} \in \{0,1\}$. At this point, Eq. (3.58) may be reduced to

$$
\begin{aligned}
&e^{-i(\tilde{k}+\Pi_B)\cdot(\tilde{z}+\vec{D})} \\
&= \frac{1}{V} \sum_{\tilde{p}'} \sum_{CC'} \left[i \sum_{\mu} \delta_{B,C+\eta_\mu} (-1)^{B_\mu} \sin(\tilde{k}_\mu a) + \delta_{B,C}\, ma \right] \\
&\times e^{+i(\tilde{p}'+\Pi_{C'})\cdot(\tilde{z}+\vec{D})} G^{CC'}(\tilde{k},\tilde{p}')\,.
\end{aligned}
\tag{3.61}
$$

The factor in square brackets should be reminiscent of the four-component spinor factor

$\not{k} + m$. Indeed, this factor is easily inverted by multiplying

$$\left[-i \sum_{\nu} \delta_{A,B+\eta_\nu} (-1)^{A_\nu} \sin(\tilde{k}_\nu a) + \delta_{A,B}\, ma \right] . \tag{3.62}$$

The cross terms involving one factor of ma immediately cancel because of the relative sign on the first term. Likewise, for the terms proportional to $\sin(\tilde{k}a)$, only the $\mu = \nu$ terms survive. This is the result of the relation

$$\sum_{B} \delta_{A,B+\eta_\nu} \delta_{B,C+\eta_\mu} (-1)^{A_\nu + B_\mu} = \delta_{A,C+\eta_\mu+\eta_\nu} (-1)^{A_\nu + C_\mu + (\eta_\mu)_\mu} \tag{3.63}$$

which, when summed over C, gives the sign $(-1)^{A_\mu + A_\nu + (\eta_\nu)_\mu}$. Under the replacement $\mu \leftrightarrow \nu$, the factor

$$(-1)^{(\eta_\nu)_\mu} \to (-1)^{(\eta_\mu)_\nu} = -(-1)^{(\eta_\nu)_\mu} , \tag{3.64}$$

so the cross terms will always cancel. Carrying out the product gives

$$\begin{aligned} &\left[-i \sum_{\nu} \delta_{A,B+\eta_\nu} (-1)^{A_\nu} \sin(\tilde{k}_\nu a) + \delta_{A,B}\, ma \right] \times \left[+i \sum_{\mu} \delta_{B,C+\eta_\mu} (-1)^{B_\mu} \sin(\tilde{k}_\nu a) + \delta_{B,C}\, ma \right] \\ &= \left[\sum_{\mu} \sin^2(\tilde{k}_\mu a) + (ma)^2 \right] \delta_{A,C} . \end{aligned} \tag{3.65}$$

Dividing out the prefactor and applying another Fourier transform reduces Eq. (3.61) to

$$\begin{aligned} G(x,z) &= \frac{1}{V^2} \sum_{\tilde{k}\tilde{p}'} \sum_{AC'} e^{+i(\tilde{k}+\Pi_A)\cdot(\tilde{x}+\vec{E})} e^{+i(\tilde{p}'+\Pi_{C'})\cdot(\tilde{z}+\vec{D})} G^{AC'}(\tilde{k},\tilde{p}') \\ &= \frac{1}{V} \sum_{\tilde{k}} \sum_{AB} \frac{-i \sum_\nu \delta_{A,B+\eta_\nu} (-1)^{A_\nu} \sin(\tilde{k}_\nu a) + \delta_{A,B}\, ma}{\sum_\mu \sin^2(\tilde{k}_\mu a) + (ma)^2} e^{+i(\tilde{k}+\Pi_A)\cdot(\tilde{x}+\vec{E})} e^{-i(\tilde{k}+\Pi_B)\cdot(\tilde{z}+\vec{D})} \\ &= \frac{1}{V} \sum_{k} \frac{-i \sum_\nu \eta_\nu(z) \sin(k_\nu a) + ma}{\sum_\mu \sin^2(k_\mu a) + (ma)^2} e^{-ik\cdot(z-x)} , \end{aligned} \tag{3.66}$$

completing the computation of the staggered propagator.

3.2.2 Computational Solution for a Quark Propagator

In practice, it is computationally prohibitive on the lattice to solve $G(y,z)$ in Eq. (3.51) for all y and z. This would require enough memory to store the number of sites squared complex numbers. To circumvent this issue, the propagator is convolved with a source object specification $\xi^{cd}(z)$ that solves

$$\sum_{b,c,y,z} \left(\not{D}+m\right)^{ab}_{x,y} G^{bc}(y,z)\xi^{cd}(\vec{z};t) \equiv \sum_{b,y} \left(\not{D}+m\right)^{ab}_{x,y} \widetilde{G}^{bd}(y;t) = \xi^{ad}(\vec{x},t)\,, \tag{3.67}$$

which has replaced the delta function that usually appears in the Green's function with a source object.

Sources constructed in this way do not necessarily preserve gauge invariance for all terms in the sum. This is seen by looking at two simple sources combined together to give a propagator. Consider two sources tied together with

$$\xi^{cd}(\vec{z},t) = \delta^{cd}\delta(\vec{z}\bmod 2, 0)\,, \tag{3.68}$$

which has non-zero support on every other lattice site throughout a timeslice. Then a two-point correlation function can be constructed by squaring the Green's function to give a pion propagator,

$$\begin{aligned} C_{(2)}(t) &= \sum_{b,d,y} \left[\widetilde{G}^{db\,*}(y;t)\right]^{-1} \left[\widetilde{G}^{bd}(y;t)\right]^{-1} \\ &= \sum_{b,d,y,z,z'} \left[G^{db\,*}(y,z)\right]^{-1} \left[G^{bd}(y,z')\right]^{-1} \delta(\vec{z}\bmod 2,0)\delta(\vec{z}'\bmod 2,0)\,. \end{aligned} \tag{3.69}$$

The non-gauge invariant contributions come from pieces in which $\vec{z} \neq \vec{z}'$. In the ensemble average, the gauge-variant pieces will average to zero, but contribute noise.

The noise contributions can be partially mitigated by fixing to a particular gauge. When the gauge is fixed, the quark operators change to include some gauge link "cloud" around

the operator, summarized as

$$\chi(x) \to \sum_y V(y,x)\chi(x)\,. \tag{3.70}$$

The matrix $V(y,x)$ can be thought of as a weighted average of gauge link paths connecting site y to site x. Gauge links also get connecting matrices, of the form

$$U_\mu(x) \to \sum_{y,y'} V(y,x)U_\mu(x)V^\dagger(x+\mu,y')\,. \tag{3.71}$$

Operators that may have vanished in the ensemble average before contribute a nonzero amount after gauge fixing, for instance

$$\begin{aligned} &\langle\overline{\chi}(x)\chi(x')\rangle = 0 \quad (\vec{x}\neq\vec{x}') \\ \to &\sum_{y,y'}\langle\overline{\chi}(x)V^\dagger(x,y)V(y',x')\chi(x')\rangle = \sum_y \langle\overline{\chi}(x)V^\dagger(x,y)V(y,x')\chi(x')\rangle \neq 0\,. \end{aligned} \tag{3.72}$$

In the staggered baryon code, two types of quark propagators are used. The first is the "corner wall" source, namely Eq. (3.68). The second source used in constructing staggered baryon correlation functions is the random wall source, with a similar construction given by

$$\sum_z \left(\not{D}+m\right)^{ab}_{x,y}\widehat{G}^{bc}_A(y;t) = \widehat{\xi}^{ad}(\vec{x})\delta(\vec{x}\bmod 2,\vec{A}) \tag{3.73}$$

where $\widehat{\xi}^{ad}$ is Gaussian random noise generated in vectors that satisfy the condition

$$\langle\left(\widehat{\xi}^{ab}(\vec{x})\right)^*\widehat{\xi}^{bc}(\vec{y})\rangle = \delta^{ac}\delta(\vec{x},\vec{y})\,. \tag{3.74}$$

In principle, baryon correlators could also be constructed with "baryon random wall" noise sources, which share Eq. (3.73) but with noise that instead satisfies

$$\langle\epsilon^{a'b'c'}\widehat{\xi}^{a'a}(\vec{x})\widehat{\xi}^{b'b}(\vec{y})\widehat{\xi}^{c'c}(\vec{z})\rangle = \epsilon^{abc}\delta(\vec{x},\vec{y})\delta(\vec{y},\vec{z})\,. \tag{3.75}$$

These noise sources allow for the construction of point baryon sources, but the numerics of this computation make them not practical. The reason is that these operators suffer from an unfavorable signal-to-noise scaling. Due to the condition on the random noise vectors in Eq. (3.75), the only terms that contribute to the signal are those for which $\vec{x} = \vec{y} = \vec{z}$. This occurs only once for every site within a timeslice. However, terms with $\vec{x} \neq \vec{y}$ or $\vec{y} \neq \vec{z}$ will contribute to the noise, for which this happens $\sim V^3$ times for the volume V. So the signal-to-noise scaling goes as

$$S/N \propto \frac{V}{\sqrt{V^3}} = V^{-\frac{1}{2}}\,, \tag{3.76}$$

decreasing with the square root of the volume. This is not the case for the mesonic noise in Eq. (3.74), for which

$$S/N \propto \frac{V}{\sqrt{V^2}} \sim \text{const}\,. \tag{3.77}$$

In practical situations, the scaling will be slightly better than these estimates because the contribution to the signal or noise exponentially falls off with distance, but the baryon random walls performed poorly already for the smallest volume they were tested on.

3.2.3 Meson Operators

Most simple observables involving baryons are constructed from an equal number of baryon and antibaryon operators. When these two operators are tied together, one obtains an object transforming under the tensor product of the baryon and antibaryon representations, no matter what the temporal separation of the baryon-antibaryon pair. Rather than worrying about the details of the baryon operators, it is often easier to treat the baryon-antibaryon pair as a quark-antiquark pair instead. The group theory product rules for the resulting mesonic operators are both easier to work out and conceptually easier to grasp. The only complication is for the 16 representation, in which the operators transform like two-vectors at each site. Special care is needed for these operators, but the analogy with a meson presented here still holds.

As was discussed in the previous section, baryon operators transform under the three fermionic lattice irreps, named according to their dimensions: the 8, $8'$, and 16. The factors of eight in the dimensions stem from the eight sites on the unit cube. This "taste" index is explained in more detail in Sec. 3.1.1. Projecting a quark field to zero momentum, we may represent the fundamental quark field, which transforms in the 8 representation, solely by its taste index as

$$\chi_A = \sum_{\vec{y}} \chi(2\vec{y} + \vec{A}) \,, \tag{3.78}$$

where the sum over $\vec{y}$ picks out every other site on a single timeslice.

For the rest of this section, color indices play no role and will be omitted. Meson operators are constructed by stitching together a quark-antiquark pair with a phase, of the general form

$$\phi^{\Gamma\otimes\Xi}_{A\bar{A},B} = \omega^{\Gamma\otimes\Xi}_{B}(A)\overline{\chi}_{\bar{A}}\chi_A\delta_{A,\bar{A}+B} \,, \tag{3.79}$$

where Γ and Ξ denote the spin and taste structure, respectively, of the operator, and B is fixed depending on the current being considered. Here, $\omega^{\Gamma\otimes\Xi}$ denotes a phase that takes the values ± 1, and depends on the lattice site A and the spin and taste Γ and Ξ, respectively.

The spatial structure of the operators in Eq. (3.79), corresponding to the spin and taste of an equivalent naive quark operator, are encoded into into the phases and the relative displacement B. It is easy to see that a nonlocal ($B \neq 0$) operator can change orientation under rotations. To illustrate the spatial structure of the phases, consider the local spatial-axial current, $\phi^{\mathcal{A}_i\otimes\mathcal{A}_i}_{B=0}$. This operator has the form

$$\phi^{\mathcal{A}_i\otimes\mathcal{A}_i}_{A\bar{A},0} = (-1)^{\vec{A}_i}\overline{\chi}_{\bar{A}}\chi_A \,. \tag{3.80}$$

Under a rotation R_{ij}, the phases swap sites, bringing

$$(-1)^{\vec{A}_i} \to (-1)^{\vec{A}_j} \,. \tag{3.81}$$

This operator still transforms as though it had a direction dependence, since the direction dependence is encoded into the relative signs of the sites.

Non-vanishing correlation functions at zero momentum are those that have trivial transformations under the lattice timeslice symmetries. For all zero momentum irreducible representations of the lattice timeslice group (both bosonic and fermionic), the only way to construct an operator in the trivial representation is to trace over the square of the operator:

$$\phi^{\mathcal{S}\otimes\mathcal{S}} = \mathrm{Tr}[\overline{R}\otimes R] = \sum_{\alpha} \overline{R}^{\alpha} R_{\alpha} \tag{3.82}$$

for any irrep R and components α. If we replace R by any meson operator, we end up with a meson two-point function

$$C(t) = \langle \phi^{\Gamma\otimes\Xi}(t)\phi^{*\Gamma\otimes\Xi}(0)\rangle\,. \tag{3.83}$$

At nonzero momentum, this condition is relaxed to allow for correlation functions that are proportional to the momentum, for instance the continuum (trivial taste) matrix element

$$\langle \mathcal{A}_{\mu}(t)\mathcal{P}(0)\rangle \propto p_{\mu}\,. \tag{3.84}$$

Despite this, the tensor product of all operators in the expectation value must transform trivially under the taste symmetry.

Often, it is beneficial to shortcut the sum in Eq. (3.82) by computing a sum over only one of the terms. In this case, the operator is put into a reducible representation that is made

up of the sum of all of the operators. For example, the restriction to a corner wall source

$$\begin{aligned}\sum_{\alpha} \overline{R}^{\alpha} R_{\beta} =& \sum_{A'} \phi^{\Gamma\otimes\Xi} \times \overline{\chi}_{A'} \chi_{A'} \delta_{A',0} \\ =& \phi^{\Gamma\otimes\Xi} \times \sum_{A'} \left[\frac{1}{8} \left(1 + (-1)^{\vec{A}'_1} + (-1)^{\vec{A}'_2} + \dots \right) \overline{\chi}_{A'} \chi_{A'} \right] \\ =& \phi^{\Gamma\otimes\Xi} \times \frac{1}{8} \left[\phi^{\mathcal{S}\otimes\mathcal{S}} + \phi^{\mathcal{S}\otimes\mathcal{V}_i} + \phi^{\mathcal{S}\otimes\mathcal{V}_j} + \dots \right] \end{aligned} \tag{3.85}$$

for which only the appropriate trace term will be nonvanishing.

3.2.4 Baryon Operators

Consider a quark trilinear object with all of the quarks on the same timeslice,

$$\mathcal{T}^{ijk,abc}_{ABC} = \chi^{i,a}_{A} \chi^{j,b}_{B} \chi^{k,c}_{C} \,, \tag{3.86}$$

where a, b, and c are color indices, i, j, and k are flavor indices, and A, B, C, are taste indices. It is worth noting that the group theory dictates that these operators behave similar to a lone quark at a site $D = A + B + C$, with the exception of how treatment of the two-vector in the 16 representation is handled and the sign under rotations for the $8'$ representation. This is immediately apparent for the shift symmetry, where

$$\mathcal{T}^{ijk,abc}_{ABC} \to \zeta_{\mu}(A)\zeta_{\mu}(B)\zeta_{\mu}(C) \mathcal{T}^{ijk,abc}_{A+\mu,B+\mu,C+\mu} = \zeta_{\mu}(A+B+C) \mathcal{T}^{ijk,abc}_{A+\mu,B+\mu,C+\mu} \,, \tag{3.87}$$

noting that under the sum modulo 2,

$$(A+\mu) + (B+\mu) + (C+\mu) = A + B + C + \mu = D + \mu \,. \tag{3.88}$$

It is only for the transformations under rotations that the behavior may differ from a single quark.

We can define a tensor that corresponds to an operator in an irreducible representation of the lattice spacetime group by $\mathcal{O}^{ijk,r}_{ABC,D}$, where r is meant to represent the specific construction of the operator within the irreducible representation. The different rs come about from selecting different sites on a unit cube for each quark in the baryon trilinear. There are many ways of choosing these combinations, and the choices were classified in Ref. [56]. We adopt the same convention for organizing operators into classes. It turns out that for each taste state in Eq. (3.2), there exists an operator that transforms in that irreducible representation.

We note that the tensor $\mathcal{O}^r$ is symmetric under simultaneous exchange of flavor and taste:

$$\mathcal{O}^{ijk,r}_{ABC,D} = \mathcal{O}^{jik,r}_{BAC,D} = \mathcal{O}^{ikj,r}_{ACB,D}\,. \tag{3.89}$$

The details of the structure of how the tensor $\mathcal{O}^r$ are constructed for specific irreps are given in Ref. [64] and not written out in detail here. The baryon operator is then

$$\mathcal{B}^r_D = \sum_{abc}\sum_{ijk}\sum_{ABC} \mathcal{O}^{ijk,r}_{ABC,D}\chi^{i,a}_A \chi^{j,b}_B \chi^{k,c}_C \epsilon^{abc}\,, \tag{3.90}$$

where ϵ^{abc} is the Levi-Civita antisymmetric tensor. The antibaryon operator is created by complex conjugating $\mathcal{B}^r_D$ and replacing $\chi \to \overline{\chi}$. To construct a two-point correlation function, all of the quark operators within the baryon and antibaryon operators are contracted into propagators, and the appropriate trace over baryon source and sink locations is taken. The correlation function then takes the form (assuming the antibaryon operator starts at $t = 0$)

$$\begin{aligned} C^{r\bar{r}}_{(2)}(t,0) =& \sum_D \langle \mathcal{B}^r_D(t)\overline{\mathcal{B}}^{\bar{r}}_D(0)\rangle \\ =& \sum_{abc\bar{a}\bar{b}\bar{c}}\sum_{ijk\bar{i}\bar{j}\bar{k}}\sum_{ABC\bar{A}\bar{B}\bar{C}}\sum_D \epsilon^{abc}\epsilon^{\bar{a}\bar{b}\bar{c}} \left(\mathcal{O}^{\bar{i}\bar{j}\bar{k},\bar{r}}_{\bar{A}\bar{B}\bar{C},D}\right)^* \mathcal{O}^{ijk,r}_{ABC,D} \\ & \times \left[G^{i\bar{i},a\bar{a}}_{A\bar{A}}(t,0)\right]^{-1} \left[G^{j\bar{j},b\bar{b}}_{B\bar{B}}(t,0)\right]^{-1} \left[G^{k\bar{k},c\bar{c}}_{C\bar{C}}(t,0)\right]^{-1}\,. \end{aligned} \tag{3.91}$$

Since there are multiple baryon operators that transform in the irreducible representations of the lattice symmetry group, one can construct a large operator basis simply by varying r and $\bar{r}$ over the many different operator constructions of Ref. [64].

The baryon operators with a three-point current insertion included must use another propagator to represent the daughter quark from the current insertion to the sink operator. In this case, it makes sense to tie up the two spectator quarks separately from the leg with the current insertion. The spectator object contracts over two quarks, giving

$$\left[\widetilde{G}^{i\bar{i},a\bar{a},r\bar{r}}_{A\bar{A},D\bar{D}}(t,0)\right]^{-1} = \sum_{bc\bar{b}\bar{c}} \sum_{jk\bar{j}\bar{k}} \sum_{BC\bar{B}\bar{C}} \epsilon^{abc}\epsilon^{\bar{a}\bar{b}\bar{c}} \left(\mathcal{O}^{\bar{i}\bar{j}\bar{k},\bar{r}}_{\bar{A}\bar{B}\bar{C},\bar{D}}\right)^* \mathcal{O}^{ijk,r}_{ABC,D} \times \left[G^{j\bar{j},b\bar{b}}_{B\bar{B}}(t,0)\right]^{-1} \left[G^{k\bar{k},c\bar{c}}_{C\bar{C}}(t,0)\right]^{-1} . \tag{3.92}$$

This spectator contribution behaves in much the same way that an antiquark propagator would in a meson operator.

The interacting quark leg itself looks like a quark propagator, and is constructed as

$$\left[\widehat{G}^{i\bar{i},a\bar{a},\Gamma\otimes\Xi}_{A\bar{A},E}(t,\tau,0)\right]^{-1} = \sum_{i'A'e\bar{e}} \left[G^{\bar{i}i',a\bar{e}}_{A,(A'+E)}(t,\tau)\right]^{-1} \left[\omega^{\Gamma\otimes\Xi,\bar{e}e}_{E}(A')\right] \left[G^{i'i,e\bar{a}}_{A'\bar{A}}(\tau,0)\right]^{-1} , \tag{3.93}$$

where $\omega^{\Gamma\otimes\Xi}_{E}$ is defined in Eq. (3.79) with the color indices reintroduced here. Combining the two expressions for the spectator and interaction legs of the three-point function, we find the correlation function

$$\begin{aligned} C^{\Gamma\otimes\Xi,r\bar{r}}_{(3),E}(t,\tau,0) &= \sum_{D} \langle \mathcal{B}^{r}_{D+E}(t)| \, \phi^{\Gamma\otimes\Xi}_{E} \, |\overline{\mathcal{B}}^{\bar{r}}_{D}(0)\rangle \\ &= \sum_{D} \sum_{i\bar{i}a\bar{a}A\bar{A}} \left[\widetilde{G}^{i\bar{i},a\bar{a},r\bar{r}}_{A\bar{A},D,(D+E)}(t,0)\right]^{-1} \left[\widehat{G}^{i\bar{i},a\bar{a},\Gamma\otimes\Xi}_{A\bar{A},E}(t,\tau,0)\right]^{-1} . \end{aligned} \tag{3.94}$$

3.2.5 Code Implementation

Producing a baryon correlation function of the form in Eq. (3.94) depends on the operators r and $\bar{r}$ being considered. Most operators reuse large subsets of index combinations, but the number of possible index combinations in Eqs. (3.92) and (3.93) is huge[2]. This means that the code is especially amenable to reuse of quark operator tie-ups. The code is designed in such a way that tie-ups are only done once, then saved to memory. Memory constraints are a challenge, but can be circumvented by using a memory map to increase the storage capacity.

The first ingredient that is computed and stored is the parallel-transported the quark propagators. Parallel transport [56] indicates that paths are averaged to take all possible shortest-link paths in both positive and negative directions. If we define

$$\overleftrightarrow{U}_i(x,x') = \frac{1}{2}\left(U_i(x)\delta_{x,x'-\hat{i}} + U_i^\dagger(x-\hat{i})\delta_{x,x'+\hat{i}}\right) , \tag{3.95}$$

then the parallel transport dressing with links is

$$V_B^{bc}(x,y) = \begin{cases} \delta_{x,y} & : \sum_\ell \vec{B}_\ell = 0 \\ \overleftrightarrow{U}_i(x,y) & : \sum_\ell \vec{B}_\ell = 1 \\ \frac{1}{2}\sum_{x',i,j} \overleftrightarrow{U}_i(x,x')\overleftrightarrow{U}_j(x',y) & : \sum_\ell \vec{B}_\ell = 2 \\ \frac{1}{6}\sum_{x',x'',i,j,k} \overleftrightarrow{U}_i(x,x')\overleftrightarrow{U}_j(x',x'')\overleftrightarrow{U}_k(x'',y) & : \sum_\ell \vec{B}_\ell = 3 \end{cases} , \tag{3.96}$$

where the sums are implicitly taken over $i \neq j \neq k \neq i$ and only for the directions that $\vec{B}_\ell = 1$. Defining the corner wall propagator $\left[\widetilde{G}_A^{bc}(y;t)\right]^{-1}$ as the solution to the Green's function in Eq. (3.51) with source Eq. (3.68), are dressed with the gauge links on the sink to form

$$\left[\widetilde{H}_{AB}^{ac}(y;t)\right]^{-1} = \sum_{x,b}\left[\widetilde{G}_A^{ab}(x;t)\right]^{-1} V_B^{bc}(x,y) . \tag{3.97}$$

2. For Eq. (3.92), the number of combinations of tie-ups in the code that are saved is $8^6 \times 3^2 = 2359296$. See Eq. (3.99) for the actual implementation.

This is done for three sets of eight propagators, corresponding to the three quarks that make up the baryon operator and the eight unit cube sites from which they can originate. The taste index A denotes the corner that the corner wall started from, and index B is the point-splitting at the sink.

For the two-point functions, there is no need to save any more than this. The correlation function is tied up as

$$C_{(2)}^{r\bar{r}}(t,0) = \sum_{abc\bar{a}\bar{b}\bar{c}} \sum_{ijk\bar{i}\bar{j}\bar{k}} \sum_{ABC\bar{A}\bar{B}\bar{C}} \sum_{D} \epsilon^{abc}\epsilon^{\bar{a}\bar{b}\bar{c}} \left(\mathcal{O}^{\bar{i}\bar{j}\bar{k},\bar{r}}_{\bar{A}\bar{B}\bar{C},D}\right)^* \mathcal{O}^{ijk,r}_{ABC,D} \times \delta^{i\bar{i}}\delta^{j\bar{j}}\delta^{k\bar{k}} \left[\widetilde{H}^{a\bar{a}}_{A\bar{A}}(t,0)\right]^{-1} \left[\widetilde{H}^{b\bar{b}}_{B\bar{B}}(t,0)\right]^{-1} \left[\widetilde{H}^{c\bar{c}}_{C\bar{C}}(t,0)\right]^{-1}, \tag{3.98}$$

equivalent to Eq. (3.91). Since we fix to Coulomb gauge, the absence of links at the source is irrelevant. It is possible to put links at the source, but this would introduce the complication of which site those links tie up to and increase the number of inversions to account for all possible combinations of link displacement versus corner A, B, and C. For these reasons, the gauge links are not put in.

For the three-point correlation function tie-ups, further improvement in computing time is made by saving more data for reuse. The next piece to tie up is the spectator quark contribution, for use in completing the construction delineated in Eq. (3.92). After tying together the two spectator quarks into a pair, parallel transport links are applied again and random wall noise is multiplied to prepare the contributions for attaching the interaction leg. The code saves spectator contributions of the form

$$\left[\widetilde{H}^{j\bar{j}k\bar{k},\hat{a}\bar{a}}_{AB\bar{B}C\bar{C},D}(t,0)\right]^{-1} = \sum_{abca'\bar{b}\bar{c}} \sum_{xy} \epsilon^{abc}\epsilon^{\bar{a}\bar{b}\bar{c}}\,\delta^{j\bar{j}}\delta^{k\bar{k}}\widehat{\xi}^{\hat{a}a'}_{A}(x) \left(V_A^{a'a}(x,y)\right)^{\dagger} \times \delta(y \bmod 2, \vec{D}) \left[\widetilde{H}^{b\bar{b}}_{B\bar{B}}(y;t)\right]^{-1} \left[\widetilde{H}^{c\bar{c}}_{C\bar{C}}(y;t)\right]^{-1}, \tag{3.99}$$

where the noise vectors $\widehat{\xi}(x)$ satisfy the requirement in Eq. (3.74) and t is fixed by the

timeslice on which $\widehat{\xi}(x)$ is defined.

The last piece to be saved is the quark leg with the current interaction, which is tied up as

$$\left[\widehat{H}^{i\bar{i},a\bar{a},\Gamma\otimes\Xi}_{A\bar{A},E}(t,\tau,0)\right]^{-1} = \sum_{i'i''A'e\bar{e}} \delta^{ii'}\delta^{i''\bar{i}}\mathcal{O}^{i'i''}\left[\widehat{H}^{ae,\Gamma\otimes\Xi}_{AA',E}(x;t,\tau)\right]^{-1}\left[\widetilde{H}^{e\bar{a}}_{A'\bar{A}}(x;\tau)\right]^{-1}, \tag{3.100}$$

where we have contracted the daughter quark propagator eminating from the sink together with the three-point interaction current to give

$$\left[\widehat{H}^{ae,\Gamma\otimes\Xi}_{AA',E}(x;t,\tau)\right]^{-1} = \sum_{y}\epsilon(y+\vec{A})\delta(A',A+E)\left[\widehat{G}^{ab}_{A}(y;t,\tau)\right]^{*-1}\left[\widehat{V}^{be,\Gamma\otimes\Xi}_{E}(y,x)\right]^{\dagger}, \tag{3.101}$$

with $\widehat{G}$ defined in Eq. (3.73) as a random wall propagator generated with the same noise as was used in Eq. (3.99). Again, t is held fixed, but τ is allowed to vary over all the timeslices. The operator $\mathcal{O}^{i'i''}$ is a stand-in operator to indicate that the interaction current may change the flavor of the quark. $\widehat{V}$ is defined similarly to V in Eq. (3.96), except that the links are applied with the signs from performing shifts and a phase to make the current have the desired spin and taste:

$$\widehat{V}^{\Gamma\otimes\Xi}_{E}(x,y) = \omega^{\Gamma\otimes\Xi}_{E}(y) \times \begin{cases} \delta_{x,y} & : \sum_\ell \vec{E}_\ell = 0 \\ \overleftrightarrow{U}_i(x,y)\zeta_i(x) & : \sum_\ell \vec{E}_\ell = 1 \\ \frac{1}{2}\sum_{x',i,j}\overleftrightarrow{U}_i(x,x')\overleftrightarrow{U}_j(x',y)\zeta_i(x)\zeta_j(x') & : \sum_\ell \vec{E}_\ell = 2 \\ \frac{1}{6}\sum_{x',x'',i,j,k}\overleftrightarrow{U}_i(x,x')\overleftrightarrow{U}_j(x',x'')\overleftrightarrow{U}_k(x'',y)\zeta_i(x)\zeta_j(x')\zeta_k(x'') & : \sum_\ell \vec{E}_\ell = 3 \end{cases}. \tag{3.102}$$

CHAPTER 4

STAGGERED BARYON SPECTRUM CALCULATION

4.1 Introduction

4.1.1 Lattice Baryons

Baryons are difficult to simulate with the Monte Carlo methods of lattice QCD. Baryon correlation functions are subject to a signal-to-noise degradation that makes simulation of baryonic observables more challenging than the equivalent meson matrix elements [65]. Baryonic correlation functions are expectation values of three quark and three antiquark operators, where the signal falls off like a nucleon propagator

$$S \sim \langle \mathcal{O} \rangle = \langle \chi^3(t) \bar{\chi}^3(0) \rangle \sim e^{-M_N t} \,. \tag{4.1}$$

The square of the noise is given by the expectation value of the operator squared, which gets contributions from a three pion propagator

$$N^2 \sim \langle \mathcal{O}\mathcal{O}^\dagger \rangle = \langle \chi^3(t) \bar{\chi}^3(t) \bar{\chi}^3(0) \chi^3(0) \rangle \sim e^{-3M_\pi t} \,. \tag{4.2}$$

Taking the signal-to-noise of the correlation function, we find that

$$S/N \sim e^{-(M_N - \frac{3}{2}M_\pi)t} \,. \tag{4.3}$$

Since the pion mass is substantially lower than the nucleon mass, the signal-to-noise ratio exponentially falls off as the time separation between the source and sink increases. With baryon correlation functions, it is not possible in practice to take $t \to \infty$, as with meson correlation functions. As a result, fits to baryon correlation functions are often restricted to a lower t range. Efforts to increase the time range by fitting to lower t can then make fits

susceptible to contamination from excited states.

Baryons are larger than mesons and are more affected by finite size corrections. Periodic boundary conditions are used to prevent edge effects caused by the finite box size of the lattice, which means that particles can self-interact via exchange of pions that loop around the lattice. As a consequence, lattice box sizes larger than the size of the baryon are necessary to realistically simulate the physics of the system, with Refs. [66–68] suggesting that a box size of $M_\pi L \gtrsim 4$ could be necessary. These finite size contributions at least as strong as $e^{-M_\pi L}$ [34, 69–71], meaning that the contributions become more significant at lower pion mass and smaller box sizes. Both smaller quark masses and larger box sizes contribute to longer computation times, making the calculations more difficult.

In this chapter, we compute the staggered baryon mass spectrum using the Highly Improved Staggered Quark (HISQ) action. This computation is a prerequisite for the computation of the axial charge and precise calculations of the baryon masses is important to have confidence in our results from studies of three-point correlation functions. We will estimate the size of taste splittings from the baryon sector and compare with the taste splittings from the meson sector. The N-like and Δ-like masses are extracted on a single lattice ensemble with statistical errors only. A computation of the spectrum with the asqtad action [72] appeared in Ref. [73], and some preliminary results for this computation appeared in Ref. [74].

4.1.2 Ensemble Data

As detailed in Sec. 1.2.2, there are many quark actions that may be used for computing lattice matrix elements. Some choices confer specific advantages that are useful for the problem at hand. In the computations presented here, we choose to compute the N-like and Δ-like spectrum as well as the axial charge using the HISQ action for both the valence and sea quarks.

We chose to compute the nucleon spectrum and axial form factor with staggered quarks because they present many characteristics that are favorable to this project. First, staggered

quarks are much faster to compute than other quark formulations due to the reduction in the number of degrees of freedom by a factor of four. This speedup in computing time allows us to compute observables with physical pion masses on several lattice spacings and to quickly compute many statistics on the ensembles we have. Computing directly at physical quark masses allows us to use different box sizes and chiral perturbation theory to estimate the effect of the finite spatial extent on our measurements. The HISQ action is chiral, meaning it is possible to compute absolutely normalized quantities with ratios of matrix elements.

Simulating with the same action in the valence and sea sector means that there will be no exceptional configurations, a problem that shows up for mixed action calculations. The exceptional configurations manifest themselves as near zero eigenvalues in the propagator, which means that the computation of quark propagators on those gauge configurations never converges.

The gauge ensembles have been generated by the MILC Collaboration with the HISQ action for the sea quarks and a one-loop Symanzik-improved gauge action for the gluons, shown in Fig. 4.1. The $a = 0.15$ fm ensemble was generated with tuned sea quark masses and is given in Ref. [75]. The other MILC ensembles are listed in Ref. [76]. The masses are computed on a single ensemble and only statistical errors are reported. The Lattice spacing is 0.15 fm with $N_S^3 \times N_T = 32^3 \times 48$ lattice sites. Correlation functions are computed with physical quark masses to eliminate the need for extrapolation to the physical point. Instead, extrapolate to the infinite volume limit by studying the dependence of results on the physical size of the box. Our ensemble has a box size of $M_\pi L = 3.5$, which is competitive with other lattice computations at physical masses. The two-point correlation functions in this chapter are computed with around 6000 measurements.

4.2 Details of Computation

The spectrum of N-like and Δ-like taste states comes from computing matrix elements constructed from quark trilinears that are temporally separated, as discussed above. The

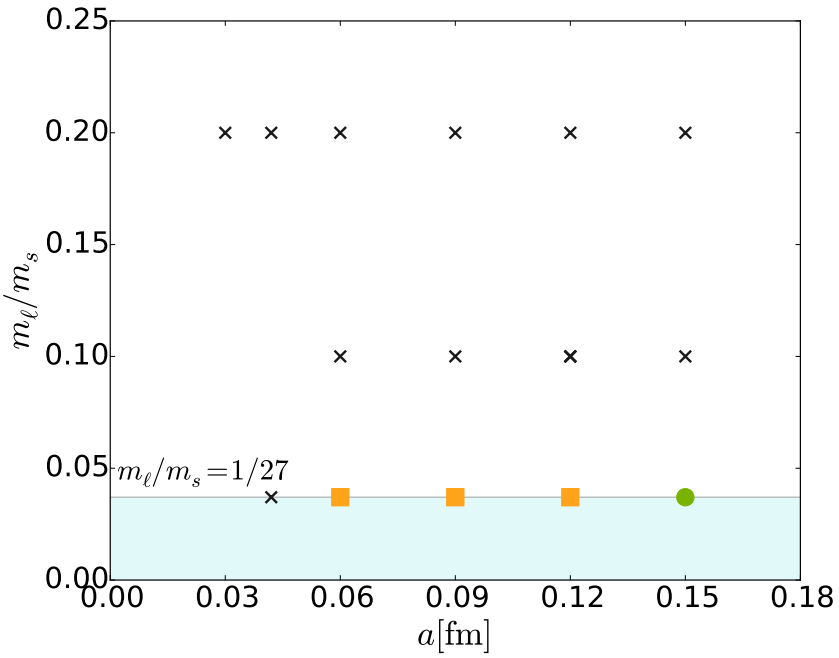

Figure 4.1: Plot of the lattice spacing versus quark masses for the MILC ensembles. The black crosses are the existing MILC ensembles. The green circle designates the ensemble for which was used for the current work. The orange squares are ensembles that will be used for future extensions of the work presented in this dissertation. The $a = 0.15$ fm ensemble uses a tuned ensemble from Ref. [75], and the other ensembles are listed in Ref. [76].

matrix elements are computed using Hamiltonian time evolution of the action and take the form

$$\begin{aligned} C_{ij}(t) &= \langle \mathcal{O}_i(t)\mathcal{O}_j^\dagger(0)\rangle = \mathrm{Tr}\left[e^{-HT}\mathcal{O}_i(t)\mathcal{O}_j^\dagger(0)\right]/\mathrm{Tr}\left[e^{-HT}\right] \\ &\underset{T\to\infty}{\to} \sum_{n^\pm} \langle\Omega|\mathcal{O}_i|n^+\rangle\,\langle n^+|\mathcal{O}_j^\dagger|\Omega\rangle\,(e^{-M_{n^+}t} - (-1)^t e^{-M_{n^+}(T-t)}) \\ &- \langle\Omega|\mathcal{O}_i|n^-\rangle\,\langle n^-|\mathcal{O}_j^\dagger|\Omega\rangle\,(e^{-M_{n^-}(T-t)} - (-1)^t e^{-M_{n^-}t})\,, \end{aligned} \tag{4.4}$$

where $n^\pm$ corresponds to a particle excitation level with parity $\pm$, Ω is the vacuum, and the sign is determined by whether the state n is bosonic or fermionic. The exponent $M_n^\pm$ is the mass of the state $n^\pm$, and takes the form of an exponential decay because of the Wick rotation to imaginary time. The exponentials $e^{-M_n^\pm(T-t)}$ come from the state propagating

through the periodic boundary condition. The states in the third line come from charge conjugating the operators, or equivalently applying parity inversion and time reversal. Since the charge conjugation operator anticommutes with the transfer matrix, each timeslice in the separation between the source and sink operators gives a factor of -1 resulting in the $(-1)^t$ factors (which are characteristic of staggered fermions).

Fits of the N-like and Δ-like baryon masses apply the techniques of constrained curve fitting [77], fitting parameters with Bayesian priors implemented as Gaussian penalty terms added to the χ^2 function. Since many states contribute to the correlation functions, the fit function must include multiple exponentials to fit the states. However, multi-exponential fits are typically ill-conditioned. Adding priors for the parameters introduces the minimal amount of extra information necessary to stabilize the fits. It is then possible to extract closely-spaced masses from fits to correlation functions.

With priors added to the fit functions, many more exponentials in the sum of Eq. (4.4) can be accommodated. The parameters that correspond to the low-lying states, in which we are most interested here, will be constrained by the data, while the other parameters will result in fit posteriors that are the same as the priors. The fitter used for this analysis was built on Lepage's "Corrfitter" codebase [78–80]. Corrfitter was modified to use Eq. (4.4) as a fit function, rather than the corresponding formula for meson two-point functions. As in the meson case, with priors on both the overlap factors and the mass splittings are employed.

The extra baryon tastes in the staggered formalism means that many states must be fit. Each of these states requires a parameter for its mass and an overlap parameter for each source and sink construction. These requirements quickly lead to fits that include hundreds of parameters. Furthermore, the signs of many of these parameters are unknown *a priori*, so priors must not unnecessarily favor overlap factors of a particular sign.

Assigning priors for every parameter in the fits is impractical. Priors for this project are assigned with heuristics. The prior central values of the lowest-mass taste states in each taste multiplet are motivated by undergraduate-level knowledge of the baryon masses, with

sufficiently large prior widths such that the priors do not drive the fit. Mass splittings for other taste states in the multiplets are estimated from the meson mass splittings in Ref. [76]. For the excited state multiplets, only the prior for the lowest state is included unless the fit shows a preference for more than one state. Including too many states can lead to instability due to a large degeneracy of many closely-spaced states. The priors on the overlap factors on the lowest-lying multiplet are all assumed to be 0 ± 10, and the excited state multiplet overlap factors are $0 \pm \frac{10}{3}$. An exception is made for one of the operators in each fit, as is discussed in the next paragraph.

When computing fits, it is often advantageous to fit to the log of the mass splitting rather than the mass splitting itself to ensure that the fitted splittings are all positive. There is another degeneracy introduced by the overlap factors since the same fit can be achieved by flipping the sign of all of the overlap factors for any excitation level n. The degeneracy could be removed by restricting to fit the log of the overlap factors. However, the computation of posterior widths with log variables is only approximately correct if those widths are small. For the typical sizes of the posterior widths on the overlap factors, the log variables are a poor approximation of the widths and the nonlinearity introduced makes the fitter unstable. Instead, this degeneracy is removed by setting the source overlap factors for one operator class to be $x \pm \frac{x}{2}$, where x is 10 for the lowest-lying multiplet and $\frac{10}{3}$ for the excited states, in agreement with the previous paragraph. So long as only one operator class is treated in this way, it should not matter which operator gets positive priors. For consistency, the first operator (i.e. the operator with the lowest class number) is fixed with positive priors.

To improve the estimates of the baryon masses from fits, we employ a chained fitting strategy. This strategy works by using posteriors from fits to independent but correlated data to inform the priors of the next fit. The fits are naturally separated into the irreducible representations of the lattice group. Computing the masses of the states in one irreducible representation may be used to inform the priors on the masses of the other irreps. The mass spectrum is first computed for the $8'$ representation, which has only Δ-like baryon states, to

estimate the Δ-like mass and the taste splitting on the lattice ensemble. These fit posteriors are taken as priors for the fit to the first two Δ-like states in the 16 representation, with widths inflated by a factor of 2 to account for further taste splittings between Δ-like states in the $8'$ and 16 representations. The fit to the 16 representation then yields precise masses for the N-like state. In the continuum limit, the mass of this state will yield our nucleon mass.

Fits are computed on a matrix of correlation functions, taking all possible combinations of the eight quark propagators that respect the group symmetries. We compute each choice of i and j for correlation functions in Eq. (4.4). All of the correlators are fit simultaneously, taking into account correlations between the different choices of source and sink operators. Fitting all of the operators simultaneously employs the same principle as a variational method, where the information from a set of similar computations is used to extract information about orthogonal components in the fits. The variational method taken at face value only allows determination of the lowest N eigenstates, where N is the size of the correlation function basis. For this reason, the simultaneous fit is preferred here.

The correlations between data are estimated when computing the statistical errors on the data. Since the gauge configurations are generated by iteratively updating previously computed gauge configurations, there is some concern that the statistical samples computed on consecutive gauge trajectories may not be completely independent. When the entries are not independent, the statistical errors computed with the standard deviation may underestimate the true errors of the data. This is corrected by blocking the data, creating new samples $\tilde{x}_\alpha$ from the original samples x_i by averaging them together with

$$\tilde{x}_\alpha = \frac{1}{n} \sum_{i=\alpha\cdot n}^{(\alpha+1)\cdot n-1} x_i \tag{4.5}$$

for a block size of n. Since the blocked data samples $\tilde{x}_\alpha$ contain information over a longer Monte-Carlo time range, the malicious sample-to-sample correlations in Monte Carlo time

will be suppressed.

4.3 Computation Results

In this section, a computation of the light baryon masses using staggered lattice QCD is presented. Computations are carried out only for the isospin $\frac{3}{2}$ (symmetric isospin) operators, since they are considerably easier to code and debug. Future studies could use the (mixed symmetry) $I = \frac{1}{2}$ operators, but there are many more operators for this irreducible representation so it remains to be seen if computing these operators is cost-effective and whether the many baryon tastes can be disentangled. However, experience on the symmetric-isospin operators suggests that computing the $I = \frac{1}{2}$ operators for the 8 or 16 representations may be advantageous if high enough statistics are available to ensure a well-conditioned correlation matrix. These operators are highly correlated, and fits that include the effects of these correlations are better able to distinguish the effects of each taste state than the irreps with fewer operators and fewer states.

4.3.1 $8'$ Representation

The first set of fits are to the $8'$ representation, which has no N-like states, but two Δ-like states. The posteriors of these fits are used to get estimates of the Δ-like mass and taste splittings. These more well-motivated estimates of the masses are used to motivate priors for the fits to later representations with N-like states.

There are two possible constructions of the sources and sinks in the $8'$ representation. These are the class 4 and 7 operators, in the terminology of Golterman [56]. The full 2×2 matrix of correlation functions is computed and fit to extract the lowest Δ-like mass, the taste splitting, and splittings to higher excited states. If the computation of the correlation functions is done in the free theory, only the "diagonal" elements, meaning those with the same source and sink operator, would be non-zero. This tells us that the correlation functions

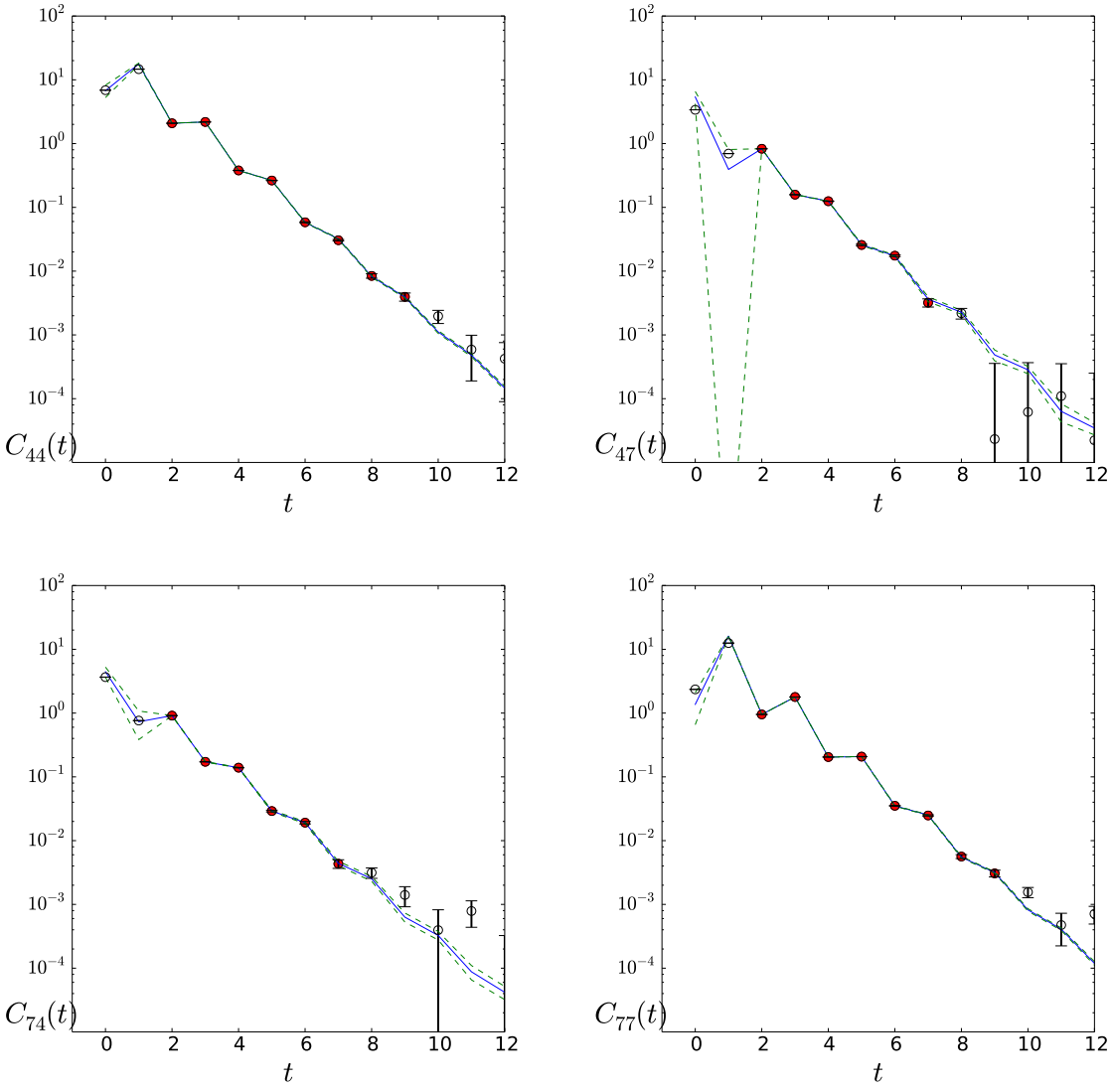

Figure 4.2: Plots of the raw correlation function data for the $8'$ representation, on a log scale. All of the plots in a row have a common source operator, and all of the plots in a column have a common sink operator. The presence of wrong-parity oscillating states is clearly visible in the correlation functions. The data that were used in the fits are shown in red, and the resulting fit is shown as a blue line. The error band on the fit is shown as a green dashed line to make it more visible. The correlation functions fall off roughly as an exponential decay at large times. The loss of the signal-to-noise is visible at large times, and larger source-sink separations are left off the plot.

will have larger overlap when the same source and sink operator are paired than with the "off-diagonal" correlation functions. We fit to a longer time range on the diagonal correlation functions as a result. The raw correlators are plotted in Fig. 4.2.

The relatively small number of states in the $8'$ representation correlation functions make them considerably easier to fit than the 8 and 16 representations. However, the contamination from excited states is still clearly visible from the correlation function data. One way to visualize the data is to plot an effective mass. Assuming that there is only one state present in the correlation function and neglecting boundary condition effects, the correlation function should fall off as an exponential decay with time,

$$C(t) \sim Ae^{-Mt}\,. \tag{4.6}$$

It is possible to isolate the mass of the state by taking a ratio of the correlation function at different times. This is

$$M = \frac{1}{\tau}\log\left[\frac{C(t)}{C(t+\tau)}\right]\,, \tag{4.7}$$

where τ is some fixed time time separation between the two correlation function measurements. The time separation τ can be picked for convenience, but a long separation will shorten the range over which the effective mass can be computed. In the following, $\tau = 2$ will be used because the oscillating opposite parity terms at the times t and $t+\tau$ will have the same sign, and so the effective mass will be less sensitive to the separation.

The data for the $8'$ representation are noisier because they only include Δ-like states, so are fit to a shorter time range than the fits with the 16 representation, shown below. Because there are fewer states within the $8'$ representation, the fits are easier to interpret and less sensitive to systematic effects. One way to verify the stability of the fits is to change the number of states used in the fit. This is shown in Figs. 4.4 and 4.5. Moving from left to right, the number of states is incremented until the central values stop moving and the errors saturate. This happens quickly for the $8'$ representation, where not many states are needed to reach stability. The fit has stabilized when 4 even and 3 odd states are included in the fit.

To further test the stability of the fits, we subject the fits to a number of systematic

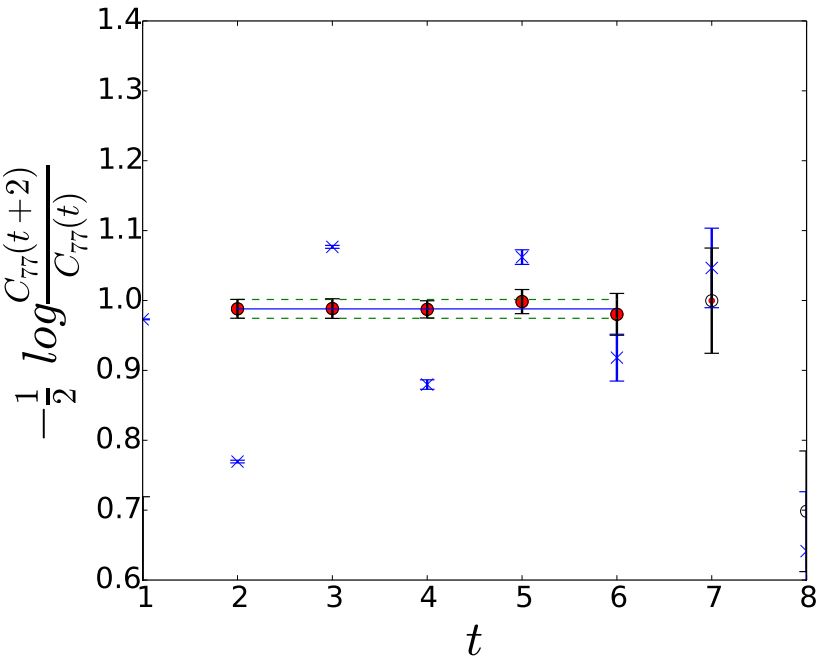

Figure 4.3: A plot of the effective mass for a correlation function in the $8'$ representation. The source and sink operator are both the class 7 operator. The blue $\times$s are the "raw" effective mass, taken as written in Eq. (4.7). The circles are again the effective mass, except the contributions to the correlation function from the excited states have been subtracted out of the data first, leaving the contribution to the data that should come from only the lowest-mass state. The blue line and green dashed errors are the mass for the lowest-mass state in the fit. A significant contribution from an excited oscillating state is visible in the raw effective mass.

checks. The checks are used to estimate the size of systematic uncertainties from fitting the correlation functions. These are compared to the nominal fit, which uses a set of default values. The nominal fit parameters are given in Table 4.1. The fit posteriors are very stable under most of the stability checks presented here. These checks are shown in Fig. 4.6 and include:

- Nominal: the default fit.
- $+1E$ state: the fit with 5 even and 3 odd states, from Fig. 4.5
- $+1O$ state: the fit with 4 even and 4 odd states, from Fig. 4.4
- $+1E + 1O$ state: the fit with 5 even and 4 odd states

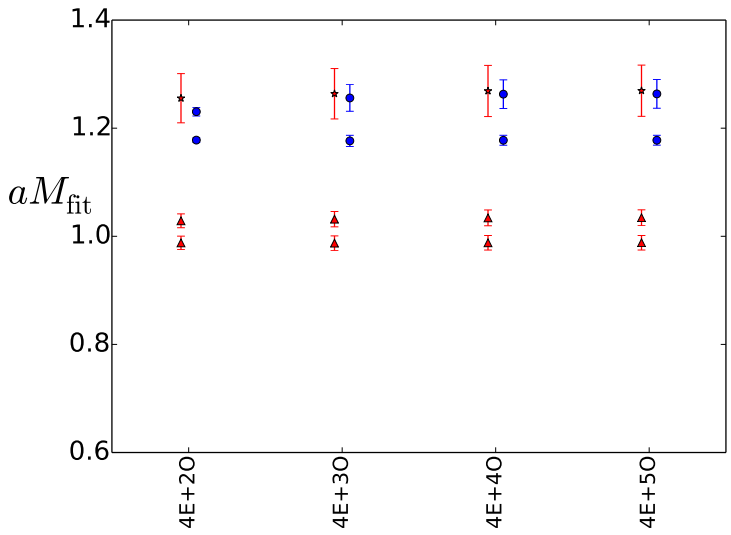

Figure 4.4: Stability plot for increasing number of states for the $8'$ representation, which has only 2 Δ-like states in the lowest-order taste multiplet. The number of even (non-oscillating in time) states is held fixed at 4 and the number of odd (oscillating) states is incremented going left to right. The vertical axis shows the extracted fit masses, in "lattice units" of the energy times the lattice spacing. Shown are the first three even states in red (offset slightly left) and the first two odd states in blue (offset slightly right). The Δ-like states are shown as triangles and the excited N-like states are shown as circles. The stars represent states with undetermined particle content.

- $t_{\text{min}} + 1$ diag: the diagonal correlation functions, i.e. those with the same source and sink operators, are fit starting from timeslice 3
- $t_{\text{min}} + 1$ offdiag: the off-diagonal correlation functions, i.e. those with different source and sink operators, are fit starting from timeslice 3
- $t_{\text{min}} + 1$ both: all correlation functions are fit starting from timeslice 3
- $t_{\text{max}} - 1$ diag: the diagonal correlation functions are fit up to timeslice 7
- $t_{\text{max}} - 1$ offdiag: the off-diagonal correlation functions are fit up to timeslice 5
- $t_{\text{max}} - 1$ both: the diagonal correlation functions are all fit to a time range that is one timeslice shorter than the nominal
- $t_{\text{max}} + 1$ diag: the diagonal correlation functions are fit up to timeslice 9

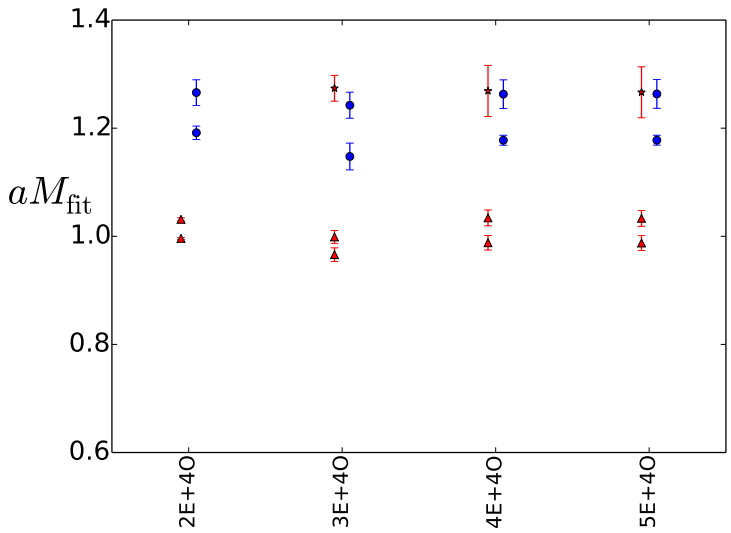

Figure 4.5: Same as Fig. 4.4, except with the number of odd states fixed and an increasing number of even states, moving from left to right.

parameter	$8'$	16
even states	4	6
odd states	3	5
diagonal time range	$[2, 9]$	$[2, 9]$
off-diagonal time range	$[2, 7]$	$[2, 7]$
taste splitting prior	0.050(25)	0.046(30)
correlator matrix size	2×2	3×3

Table 4.1: Description of nominal fit parameters for the $8'$ and 16 representations. The number of states used for the nominal fit is large enough to saturate the errors in the stability plots of Figs. 4.4 and 4.5, but the number of states that are constrained by the data is less than the number used. Time ranges are inclusive.

- $t_{\text{max}} + 1$ offdiag: the off-diagonal correlation functions are fit up to timeslice 8
- $t_{\text{max}} + 1$ both: both diagonal and off-diagonal correlation functions are fit to an additional timeslice at large times
- M_E prior $\times 1.5$: the prior widths for all of the masses of the even states are multiplied by a factor of 1.5.
- M_O prior $\times 1.5$: the prior widths for all of the masses of the odd states are multiplied by a factor of 1.5.

- source prior $\times 2.0$: the prior widths for the overlap factors for all of the source operators are multiplied by a factor of 2.0.

- sink prior $\times 2.0$: the prior widths for the overlap factors for all of the sink operators are multiplied by a factor of 2.0.

For the fits with different numbers of fit states, the states are not expected to change much. The optimal set of states for the nominal fit were chosen by examining the stability fits to find where the posterior central values and widths saturate. Adding additional states that cannot be constrained by the data with prior values centered at 0 are expected to return the prior values and contribute nothing to the fits. These checks are included to give an idea of the relative size of the shifts from Figs. 4.4 and 4.5 and to show that they are small.

Fits increasing t_{min} test the effect of low-t data, which constrain the excited states. Thus, this check is expected to change the posterior width of the higher-mass excited states and leave the lower-mass states relatively unaffected. However, if the changes are too dramatic, the higher-mass states may be subsumed into the lower-mass states. This will raise the posterior mass of the lower-mass states and the posterior of the higher-mass state will reproduce the prior information.

Fits changing t_{max} test the effect of high-t data, where the statistical errors can be quite large and possibly underestimated. If the errors have been underestimated, they could pull the fit away from the best estimates of the parameters. However, the low-t data still constrain the low-mass states, so a reduced fit range should not cause the low-mass states to become unconstrained. These checks instead test whether the data at high-t are introducing a systematic correction to the low-mass states and to quantify the size of this correction.

The fits with widened priors are meant to test the sensitivity of the fit posteriors to the priors used in the fits. If the posterior is strongly influenced by the prior, then widened priors can result in a corresponding widening of the posterior widths or significant shifts in the posterior central values. The fits with widened prior central values on the mass spectra are more sensitive to the widening because of the taste splittings. Prior widths that overlap

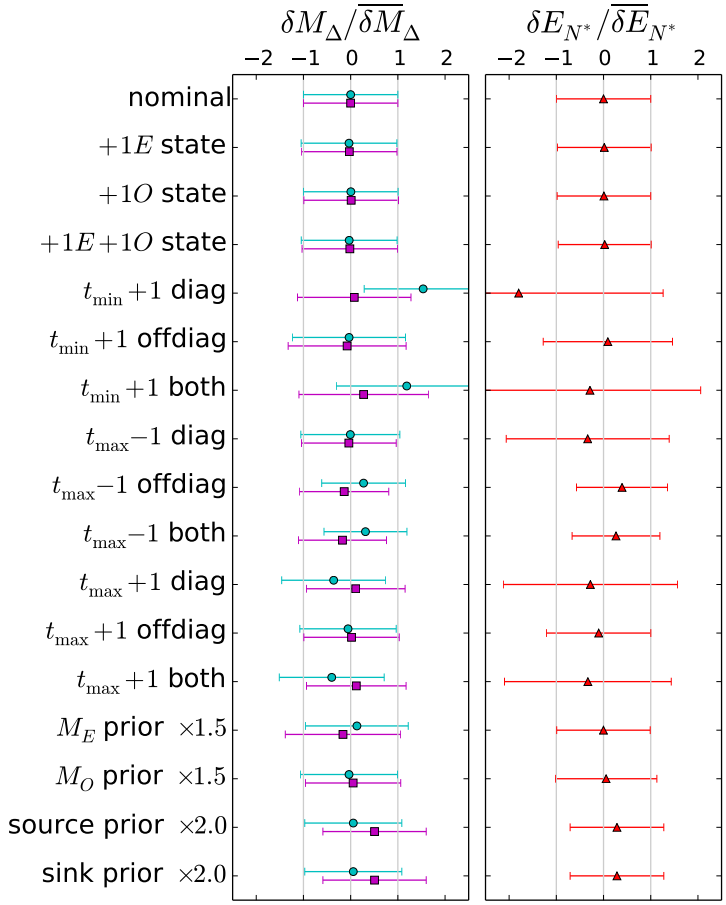

Figure 4.6: Plot of the changes relative to the central values and posteriors of the masses of the $8'$ representation states under various systematic checks. See text for the details of the checks. The data plotted are the fit posteriors for the mass splittings of the states. The nominal sample is the default sample that is being used to make the comparisons. All data have had the nominal posterior central value subtracted out and have been scaled by the nominal posterior width. These transformations scale the value and errors such that the nominal sample has central value and statistical error 0 ± 1. Masses with similar particle content in the states are grouped in the same column, where each symbol and color combination represents a different state. On the left, under the δM_Δ column, the upper (cyan) circle gives the scaled mass for the lowest Δ-like state, and the lower (purple) square is the scaled mass difference between the lowest- and second-lowest Δ-like states. On the right, under the δE_{N*} column, the (red) triangles correspond to the scaled mass of the excited N-like state. The N^* state is the lowest-lying odd parity state, which corresponds to a mass of around 1500 MeV.

too much can result in fit posteriors on the mass splittings that are tiny because both fit states are being used to describe the same physical state. Furthermore, the logarithm of the mass splittings are fit instead of the mass splittings to enforce an ordering on the states.

The logarithms introduce nonlinearities to the Hessian matrix used to compute the widths during the fitting process, and the nonlinearity is more severe when the widths are large. These nonlinearities can destabilize the fits. Widening the priors on the source and sink overlap factors are not subject to these same restrictions, so the systematic check there uses a larger inflation factor.

4.3.2 16 Representation

The next representation to fit is the 16-dimensional representation, which has one N-like state and three Δ-like states. There are four operators for this representation, which constructed with point splittings in four operator classes. The full matrix of correlation functions is shown in Fig. 4.7.

One of these operators, specifically the class 3 operator, is considerably noisier than the rest. Presumably this noise is due to small overlap of the operator with the low-mass states (and especially the N-like state) that transform in the 16 representation. The nearly vanishing correlation function constructed from the combination of a class 3 and class 4 operator indicates that the two operators have a nearly orthogonal set of overlap factors. Steeper descent into noise means that the correlation functions involving the class 3 operators will become too noisy to fit within the acceptable fit range used on the other operator classes. A shorter fit range could be applied to the class 3 operators so that they may also be included in the fits, but then care must be taken that the much less precisely determined overlap factors for the class 3 operators do not introduce a systematic shift to the fit posteriors. For simplicity, the class 3 operators are omitted from the fits.

The posterior masses for the first two even and first odd states of the $8'$ representation are taken to inform the priors of the 16 representation. The first even state, which corresponds to a Δ-like state, informs the prior of the second state of the 16 representation spectrum, the first Δ-like state. The difference between the first and second mass in the $8'$ representation is taken as a taste splitting, which is used to inform the taste splittings of all three Δ-like

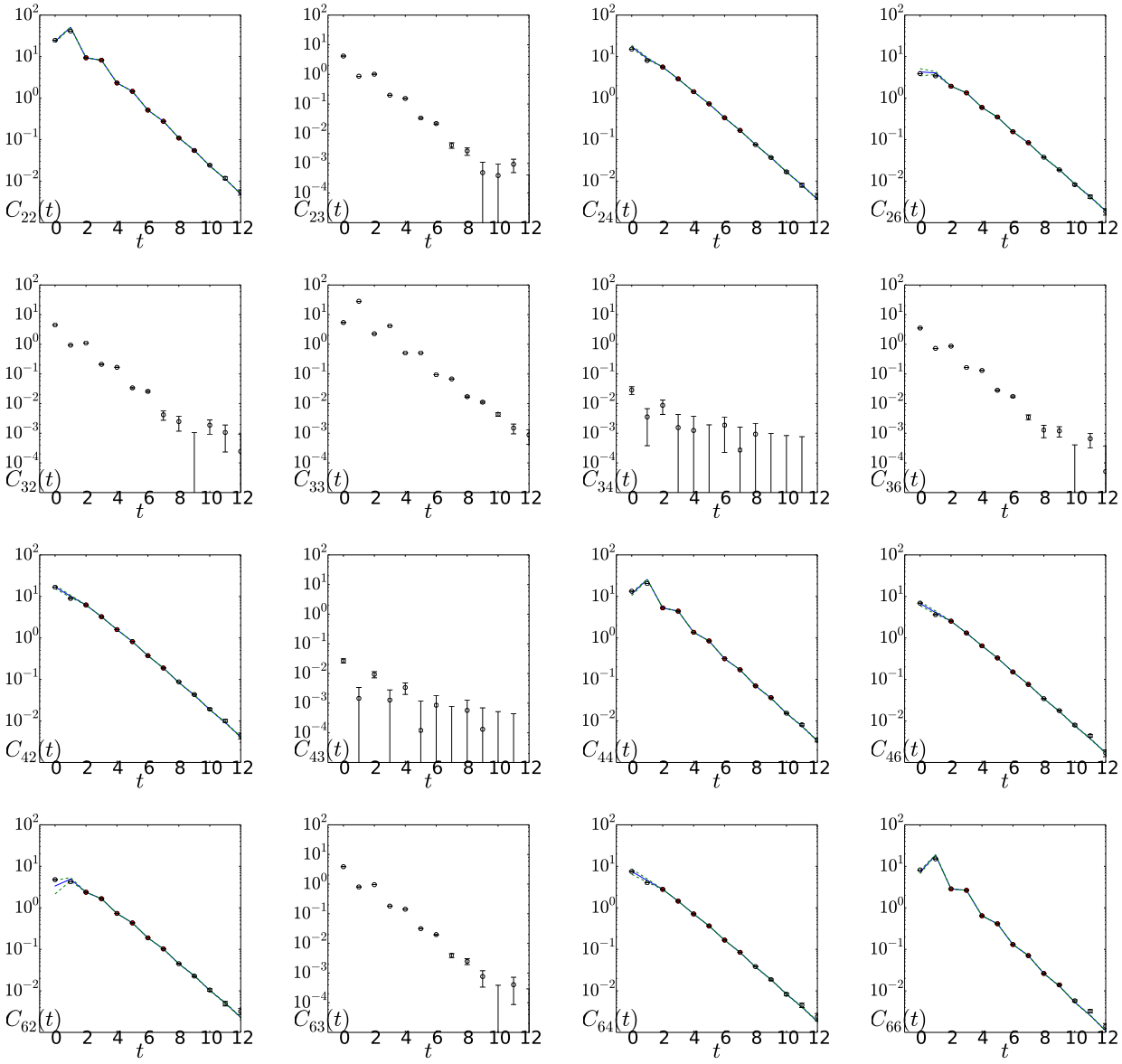

Figure 4.7: Plots of the raw correlation function data for the 16 representation, on a log scale. This set of figures is organized in the same way as Fig. 4.2. The class 3 operators (second row and column) are considerably noisier than the other operators and require special treatment. They are plotted on a different scale than the other correlation functions. For simplicity, the class 3 operators are omitted from the fits and no fit functions are plotted with the data.

states in the 16 spectrum. The prior on the lowest N-like state is taken to be the continuum nucleon mass plus the taste splitting, for better agreement with the posterior mass of the lowest state. The prior mass of the lowest odd state, the N-π state, is the sum of the axial-taste pion from Ref. [76], the continuum nucleon mass, and a taste splitting for consistency

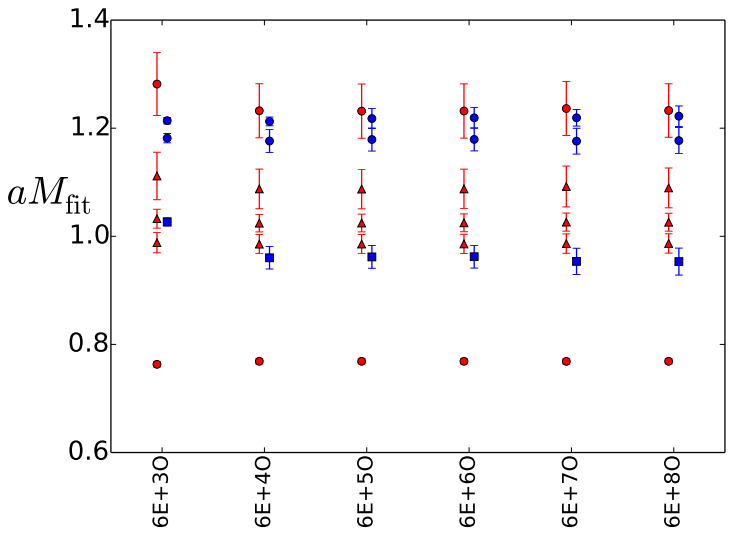

Figure 4.8: Stability plot for the 16 representation with the number of even states held fixed at six and the number of odd states increasing from left to right. The spectrum includes one N-like state and three Δ-like states, which correspond to the lowest four red data points in each column. The lowest blue odd state has a mass that is consistent with an N-π scattering state.

with the lowest even state. Both the pion and the nucleon states are assumed to have zero momentum. The second odd state mass prior is chosen from the lowest odd state posterior in the fit to the $8'$ fit. The values of priors for the lowest-lying states are listed in Sec. 4.3.3 in Table 4.3, along with the fit posteriors.

The stability plots for the spectrum of the 16 representation are shown in Figs. 4.8 and 4.9. As stated previously, the posteriors of the N-like state are higher than the physical nucleon mass. This is not a worry because discretization effects change the masses at nonzero lattice spacing. There is an upward shift in the Δ-like masses relative to the $8'$ representation too.

An interesting surprise is that the lowest odd state, suspected to be an N-π scattering state, is so well determined. The state appears as a posterior regardless of whether or not a prior for the state is included in the fit. This statement holds even when the prior width for the lowest odd state is taken to be unrealistically small, for instance smaller than the expected taste splitting. This posterior state has a mass that is too low to be consistent with an excitation of the baryon states, appearing nearly 300 MeV below the expected $N^*(1520)$

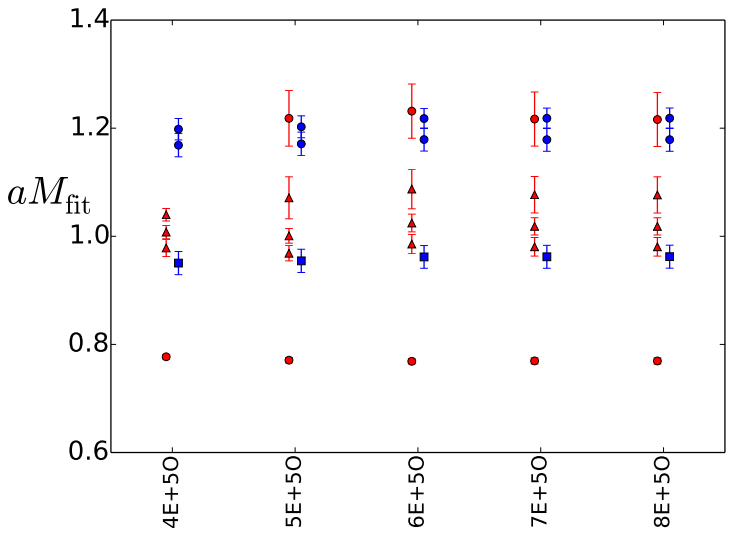

Figure 4.9: The same as Fig. 4.8, except with odd states fixed and increasing number of even states.

excitation of the nucleon. The mass is consistent with an N-π state with both the N-like baryon and the pion at rest, although it is not possible to determine precisely which taste is represented: it is consistent with the sum of the same N-like state that appears as the ground state of the non-oscillating spectrum and an axial-taste pion. The axial-taste pion can be generated from a quark-antiquark operator with $A_4 \otimes A_4$ axial spin-taste, the parity partner operator to the $S \otimes S$ singlet current. This operator construction is local, meaning that the pion would appear from a virtual quark loop that originates at the same site as the nucleon operator. The operator at the sink is constructed with a sum over the site where the baryon is tied up,

$$O_i(x) = \sum_D \sum_{abc} \epsilon^{abc} \mathcal{O}_{i,D}^{r,ABC} \chi^a_{A+D}(\tilde{x}) \chi^b_{B+D}(\tilde{x}) \chi^c_{C+D}(\tilde{x}) \,, \tag{4.8}$$

so it is expected that any virtual quark-antiquark operator that gets a nontrivial sign under shifts will have different quantum numbers. This means that any pion tastes other than the axial or scalar tastes will have vanishing matrix elements with the operator construction used here. The scalar taste pion vanishes because the scalar-taste $S \otimes S$ operator construction

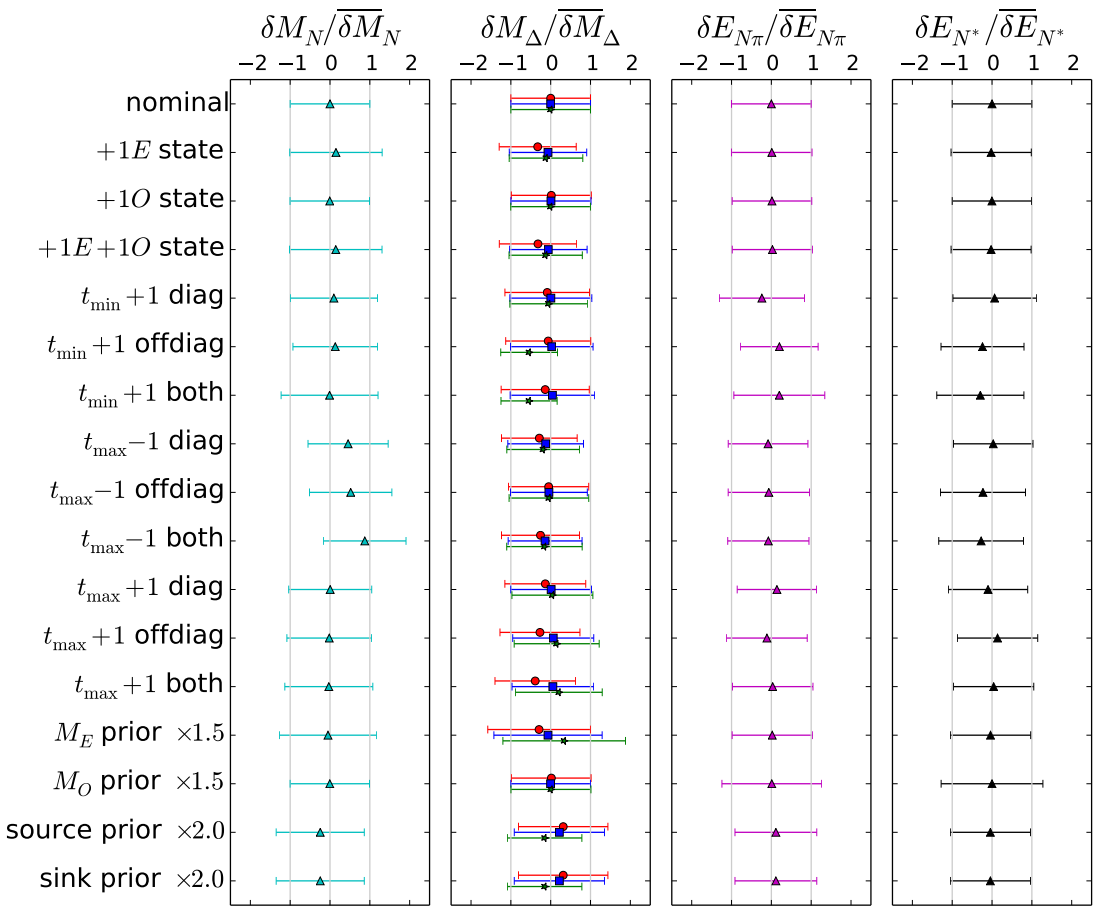

Figure 4.10: Plot of the changes relative to the central values and posteriors of the masses of the 16 representation states under various systematic checks. Figure is constructed in the same way as Fig. 4.6. The first two columns are for even-parity states, and the right two columns are for odd-parity states. The first column, under the δM_N heading, gives the scaled mass for the lowest even state, the N-like state. The second column, under the δM_Δ heading, gives the scaled mass splittings for the three even Δ-like states. The third column, under the $\delta E_{N\pi}$ heading, gives the scaled mass for the lowest odd-parity state, which corresponds to an N-π scattering state. The last column, under the δM_{N^*} heading, gives the scaled mass splitting for the second-lowest odd-parity state, which corresponds to an excited N-like state. This excited N-like state has a similar mass to the N^* state in the $8'$ representation, with about 1500 MeV.

does not have the correct parity to generate a pion.

The systematics checks for the 16 representation are shown in Fig. 4.10. These are the same set of checks that are done for the $8'$ representation, so the descriptions from Sec. 4.3.1 apply to these checks as well. The fits here are even less sensitive to the systematics checks that are applied, which indicates that the posterior spectrum is not strongly influenced by

State		Parity	Prior $[\delta M]$ [GeV]	Posterior $[\delta M]$ [GeV]
Δ	[0]	+	1.22(13) [−]	1.289(18) [−]
Δ	[1]	+	1.29(13) [0.065(33)]	1.349(16) [0.060(19)]
N^*		−	1.51(20) [−]	1.536(12) [−]

Table 4.2: List of fit priors and posteriors for the $8'$ representation. Only the states that are likely to be constrained are presented here. The results presented here give both the mass splittings (which are fit) and the absolute masses those splittings imply, accounting for correlations in the posteriors. The Δ states are both even parity states and the N^* excitation is an odd parity state. For the lowest-mass state in each parity channel, no mass splitting is reported because the absolute mass is used as the fit parameter. All of the Δ-like taste states are reported, and a number is assigned to each. Results have been converted to physical masses using the lattice spacing listed for the physical $a = 0.151$ fm ensemble in Ref. [75] without regard for the lattice spacing errors.

State		Parity	Prior $[\delta M]$ [GeV]	Posterior $[\delta M]$ [GeV]
N		+	0.994(65) [−]	1.003(6) [−]
Δ	[0]	+	1.289(74) [0.295(34)]	1.286(22) [0.283(23)]
Δ	[1]	+	1.349(80) [0.060(31)]	1.337(21) [0.051(21)]
Δ	[2]	+	1.409(89) [0.060(39)]	1.419(48) [0.082(48)]
$N\pi$		−	1.252(65) [−]	1.255(27) [−]
N^*		−	1.537(76) [0.284(39)]	1.538(13) [0.283(28)]

Table 4.3: Same as Table 4.2, but for the 16 representation. Note that the statistical precision reported here for the lowest N-like state is smaller than the statistical precision of the lattice spacing determination.

the systematics tested here.

4.3.3 Summary of Fit Posteriors

A summary of fit posteriors is given in Tables 4.2 and 4.3. Since the (log of) the mass splittings are the fit parameters, the mass splittings are listed as well as the absolute masses. The values have been converted to physical units, using $a = 0.1509$ fm from Ref. [75].

Since the posteriors are expected to reproduce the priors when the data do not constrain the values, the priors are listed next to the posteriors. The relative size of the widths on the priors and the posteriors gives an indication of how strongly the state is constrained. For the $8'$ representation, the posteriors on the absolute masses have a width that is about an order of magnitude smaller than the priors.

The posteriors for the $8'$ fit are used as priors to the 16 representation fit. The masses of the two lowest Δ-like states are informed directly from the absolute masses of the Δ-like states in the $8'$ fit, and the third Δ-like state comes from reusing the mass splitting between the two Δ-like states. Since the mass splittings are not expected to be the same in both representations, the prior widths in the 16 representation are slightly inflated from the posteriors of the $8'$ representation. The resulting mass for the N-like state in the 16 representation is very well constrained by the data, giving a sub-percent error on the mass.

CHAPTER 5

THE NUCLEON AXIAL CHARGE WITH STAGGERED BARYONS

5.1 Computation Strategy

5.1.1 The Axial Ward Identity and Axial Form Factor

The two currents of interest here are the axial and pseudoscalar currents. Assuming a two-flavor theory, the currents are

$$\begin{aligned} A^a_\mu(x) &= \sum_{ij} \overline{\psi}_i(x)\gamma_\mu\gamma_5\frac{t^a_{ij}}{2}\psi_j(x) \\ P^a(x) &= \sum_{ij} \overline{\psi}_i(x)i\gamma_5\frac{t^a_{ij}}{2}\psi_j(x)\,, \end{aligned} \tag{5.1}$$

where ψ_i is a spinor with a flavor index, assuming 2 flavors. The matrices t^a are the Pauli spin matrices and act in the flavor space over a spinors in the vector

$$\psi = \begin{bmatrix} \psi_1 \\ \psi_2 \end{bmatrix}\,. \tag{5.2}$$

The masses of the fermions may be different and are assigned to the diagonal of a mass matrix $M = \mathrm{diag}\,[m_1, m_2]$.

The divergence of the axial current can be used to derive the relation between the axial

and pseudoscalar current,

$$\begin{aligned}\partial^\mu \left(\overline{\psi}(x)\gamma_\mu\gamma_5\frac{t^a}{2}\psi(x)\right) &= \left(\partial^\mu\overline{\psi}(x)\right)\gamma_\mu\gamma_5\frac{t^a}{2}\psi(x) + \overline{\psi}(x)\gamma_\mu\gamma_5\frac{t^a}{2}\left(\partial^\mu\psi(x)\right) \\ &= \left(\not{\partial}\overline{\psi}(x)\right)\gamma_5\frac{t^a}{2}\psi(x) - \overline{\psi}(x)\gamma_5\frac{t^a}{2}\left(\not{\partial}\psi(x)\right) \\ &= \overline{\psi}(x)i\gamma_5\left\{\frac{t^a}{2}, M\right\}\psi(x)\,, \end{aligned} \tag{5.3}$$

where the curly braces denote an anticommutator. This relation is known as the axial Ward identity. The last line made use of the equations of motion for the spinors,

$$\begin{aligned}\left(\not{p} - m_i\right)\psi_i(p) &= 0 \\ \overline{\psi}_i(p)\left(\not{p} + m_i\right) &= 0 \end{aligned} \tag{5.4}$$

For $t^a = \sigma_1 \pm i\sigma_2$, the divergence trivially reduces to

$$\partial^\mu A^a_\mu(x) = (m_1 + m_2)\,\overline{\psi}(x)i\gamma_5\frac{t^a}{2}\psi(x) = (m_1 + m_2)\,P^a(x)\,. \tag{5.5}$$

For $t^a = \sigma^3$, the relation must be reduced further:

$$\begin{aligned}\partial^\mu A^3_\mu(x) &= m_1\left(\overline{\psi}_1(x)i\gamma_5\psi_1(x)\right) - m_2\left(\overline{\psi}_2(x)i\gamma_5\psi_2(x)\right) \\ &= (m_1 + m_2)\,\overline{\psi}(x)i\gamma_5\frac{t^3}{2}\psi(x) + (m_1 - m_2)\,\overline{\psi}(x)i\gamma_5\frac{\mathbb{1}}{2}\psi(x)\,. \end{aligned} \tag{5.6}$$

Taking the isospin-symmetric approximation ($m_1 = m_2 \equiv \hat{m}$), this equation reduces to the form of equation 5.5.

5.1.2 Isolating the Axial Form Factor

The coupling of nucleon states to an isovector axial current are given in terms of the axial and induced pseudoscalar form factors, represented by the forms F_A and F'_P in

$$\langle N'(p')|\, A^a_\mu \,|N(p)\rangle \,\big|_{x=0} = \bar{u}_{N'}(p') \left[\gamma_\mu\gamma_5 F_A(q^2) + \frac{q_\mu}{2M_N}\gamma_5 F'_P(q^2)\right] \frac{t^a}{2} u_N(p)\,, \tag{5.7}$$

with the momentum $q_\mu = (p' - p)_\mu$. Similarly, the isovector pseudoscalar current is related to the pseudoscalar form factor F_P by

$$\langle N'(p')|\, 2\hat{m}P^a(x) \,|N(p)\rangle \,\big|_{x=0} = \bar{u}_{N'}(p') \left[i\gamma_5 M_N F_P(q^2)\right] \frac{t^a}{2} u_N(p)\,. \tag{5.8}$$

The axial Ward identity in Eq. (5.5), here written as

$$\partial_\mu \langle A^{a\mu}(x)\rangle = 2\hat{m}\,\langle P^a(x)\rangle\ , \tag{5.9}$$

may be used to isolate the axial form factor. Applying the derivatives and a Fourier transform gives

$$\begin{aligned} iq^\mu \langle N'(p')|\, A^a_\mu \,|N(p)\rangle &= \bar{u}_{N'}(p') \left[\not{q} i\gamma_5 F_A(q^2) + \frac{q^2}{2M_N} i\gamma_5 F'_P(q^2)\right] \frac{t^a}{2} u_N(p) \\ &= \left[2M_N F_A(q^2) + \frac{q^2}{2M_N} F'_P(q^2)\right] \bar{u}_{N'}(p') i\gamma_5 \frac{t^a}{2} u_N(p) \\ &= M_N F_P(q^2)\, \bar{u}_{N'}(p') i\gamma_5 \frac{t^a}{2} u_N(p) \end{aligned} \tag{5.10}$$

where the common spinor factor has been factored out. This equation is solved for $F'_P(q^2)$ to get the expression

$$F'_P(q^2) = \frac{2M_N^2}{q^2}\left[F_P(q^2) - 2F_A(q^2)\right]\,. \tag{5.11}$$

At $q^2 = 0$, the induced pseudoscalar term vanishes and the relation becomes

$$F_P(0) = 2F_A(0)\,. \tag{5.12}$$

Substituting Eq. (5.11) into Eq. (5.7) gives the axial current matrix element

$$\langle N'|\, A^a_\mu \,|N\rangle = \bar{u}_{N'}(p') \left[\left(\gamma_\mu\gamma_5 - \frac{2M_N q_\mu}{q^2}\gamma_5 \right) F_A(q^2) + \frac{M_N q_\mu}{q^2}\gamma_5 F_P(q^2) \right] \frac{t^a}{2} u_N(p) \tag{5.13}$$

At general q^μ with $q^2 \neq 0$, the term proportional to $F_A(q^2)$ cancels when contracting Eq. (5.13) with both q^μ and $(p' + p)^\mu$. To isolate the axial form factor portion, the term proportional to the pseudoscalar form factor must be removed. The term is subtracted out by contracting with q^μ to get

$$q^\mu \,\langle N'|\, A^a_\mu \,|N\rangle = M_N F_P(q^2)\, \bar{u}_{N'}(p')\gamma_5 \frac{t^a}{2} u_N(p)\,. \tag{5.14}$$

This is used to define a pseudoscalar-subtracted axial current

$$A^{a\mu}_\perp = A^{a\mu} - 2\frac{q^\mu}{q^2} q\cdot A^a\,, \tag{5.15}$$

which when used in place of the axial current in Eq. (5.13) gives

$$\langle N'|\, A^a_{\perp\,\mu} \,|N\rangle = F_A(q^2)\, \bar{u}_{N'}(p') \left[\gamma_\mu\gamma_5 - \frac{2M_N q_\mu}{q^2}\gamma_5 \right] \frac{t^a}{2} u_N(p) \tag{5.16}$$

Up to some spinor algebra, the expression for general q_μ has been reduced to a form containing only the axial form factor.

5.1.3 Absolutely Normalizing the Axial Form Factor

With a lattice UV regulator, quantum effects can change the value of the axial form factor in Eq. (5.16) and the computation must be renormalized to reconcile the theory and experiment.

Eq. (5.16) is fixed by introducing the renormalization Z_A and making the replacement $A^{a\mu} \to Z_A A^{a\mu}$. If the lattice QCD action does not explicitly break chiral symmetry, then the normalization factors from quantum effects may be explicitly cancelled by computing similar matrix elements. This is the case for the staggered lattice QCD action. The nucleon axial form factor matrix element may be absolutely normalized by computing a ratio with an axial current matrix element creating a pion state.

The pion decay constant f_π is defined as a multiplicative factor on the axial current matrix element creating a pion state,

$$\langle \Omega | \, A^{a\mu}(x) \, | \pi^b(p) \rangle = -ip^\mu f_\pi \delta^{ab} e^{-ip\cdot x} \, . \tag{5.17}$$

In this convention, the continuum $f_\pi = 130$ MeV. The axial Ward identity in Eq. (5.5) relates the axial matrix element to the pseudoscalar matrix element through the equation

$$-ip_\mu \langle \Omega | \, A^{a\mu}(x) \, | \pi^b(p) \rangle = 2\hat{m} \langle \Omega | \, P^a(x) \, | \pi^b(p) \rangle = -p^2 f_\pi \delta^{ab} e^{-ip\cdot x} \, , \tag{5.18}$$

and may also be used to compute the pion decay constant. This property will be used later to cancel out the pion decay constant that is introduced when the ratio with the pion axial matrix element is computed.

The lattice action exhibits a softly broken $U(1)_A$ symmetry. As a result, the renormalization effects will explicitly cancel if matrix elements with the appropriate symmetry properties are computed. The combination $\hat{m}P^a(x)$, using the bare quark masses for $\hat{m}$, is the combination that gives a renormalization-free computation of the pion decay constant. For the nucleon axial current, we use the local construction of the axial form factor, which is expected to be less noisy because it does not involve gauge links. This current has a renormalization factor, but the renormalization factor is cancelled when using the same axial current to obtain the pion matrix element.

Putting these together, the renormalization factor may be computed with the ratio

$$Z_A = \frac{1}{\langle\Omega|\, A_0^a(x)\,|\pi^a(p)\rangle} \frac{\langle\Omega|\, 2i\hat{m}P^a(x)\,|\pi^a(p)\rangle}{M_\pi}\bigg|_{x=0,p=0} \tag{5.19}$$

The full relation for the form factor with the renormalization factors, up to some spinor algebra, becomes:

$$F_A(q^2) = \frac{\langle N'|\, Z_A A^a_{\perp\,\mu}(q^2)\,|N\rangle}{\langle\Omega|\, Z_A A_0^a(0)\,|\pi^a\rangle} \frac{\langle\Omega|\, 2i\hat{m}P^a(0)\,|\pi^a\rangle}{M_\pi} \times (\text{spinor factor})\,. \tag{5.20}$$

The spinor factor is worked out below with normalization conditions for states and spinors suited to finite-volume lattice-QCD calculations.

As we can see, the axial current renormalization Z_A cancels out from this choice of dimensionless ratios. If we can extract the axial charge and the excited states cleanly, we should be able to calculate the form factor.

5.1.4 Normalizing Lattice QCD to the Continuum

The lattice QCD computation must be normalized to ensure that the conventions used on the lattice agree with the conventions of the continuum parameter that is being extracted. This matters for two of the elements being extracted, specifically the pion two-point function axial current matrix element and the nucleon three-point function matrix element. The overlap factors for the nucleon are fit in the two-point functions, and so any normalization conventions will cancel in the final result automatically.

First, the pion two-point function used in the ratio must be properly normalized so the matrix element gives back only f_π in lattice units. The matrix element in question is the temporal axial current creation of a pion state, which is given in Refs. [63, 81] and in

Euclidean space reads

$$\sqrt{\frac{M_\pi V_3}{N_f}}\,\langle \pi^a(\vec{p}=0)|\, A_4^b(\vec{x},t)\,|\Omega\rangle = -\frac{M_\pi f_\pi}{Z_A}\delta^{ab}e^{-M_\pi t}\,. \tag{5.21}$$

where $N_f = 4$ is the number of tastes, V_3 is the spatial volume, and the axial current

$$A_4^b(\vec{x},t) = (-1)^t\overline{\chi}(\vec{x})\frac{t^b}{2}\chi(\vec{x})\,. \tag{5.22}$$

In this convention, the dimensionful parameters are explicitly written as a prefactor and the states satisfy

$$\langle \pi^a(\vec{p})|\pi^b(\vec{k})\rangle = \delta^{ab}\delta_{\vec{p}\vec{k}}\,. \tag{5.23}$$

The lattice computation uses an operator that is summed over all sites $\vec{x}$, so the full conversion factor reads

$$\sum_{\vec{x}}\langle \pi^a(0)|\, A_4^b(\vec{x},t)\,|\Omega\rangle = \langle \pi^a(0)|\, A_4^b(\vec{q}=0,t)\,|\Omega\rangle = -\frac{f_\pi}{Z_A}\sqrt{N_f M_\pi V_3}\,\delta^{ab}e^{-M_\pi t}\,. \tag{5.24}$$

The other matrix element that needs to be properly normalized is the axial current matrix element between the nucleon states. This uses the spatial axial current operator normalized in the same fashion. If the spinor factors are conventionally normalized by

$$\overline{u}^r(p)u^s(p) = 2M_N\delta^{rs}\,, \tag{5.25}$$

or alternatively

$$\sum_s u^s(p)\overline{u}^s(p) = i\sum_\mu \gamma_\mu \mathrm{sin}p_\mu - M_N\,, \tag{5.26}$$

then the axial charge is then defined by the relation

$$\sum_{\vec{x}}\langle N(0)|\, A_\mu^a(\vec{x},t)\,|N'(0)\rangle = \langle N(0)|\, A_\mu^a(\vec{q}=0,t)\,|N'(0)\rangle = \frac{g_A}{Z_A}\overline{u}(0)\gamma_\mu\gamma_5\frac{t^a}{2}u(0)\,. \tag{5.27}$$

The spinor factor is then easily computed for $\mu = 1, 2$, or 3, which gives

$$\overline{u}^r(0)\gamma_i\gamma_5 u^s(0) = 2M_N\, \xi^{r\,\dagger}\sigma_i\xi^s \tag{5.28}$$

with

$$\xi^1 = \begin{pmatrix} 1 \\ 0 \end{pmatrix}, \quad \xi^2 = \begin{pmatrix} 0 \\ 1 \end{pmatrix}. \tag{5.29}$$

With staggered lattice QCD, the product of spinors and gamma matrices is replaced with a staggered spinor that depends on the phase from the spin and taste. Since the propagator is normalized by the restriction of Eq. (5.26), which is related to the action, the product of the spinors remains the same. The choice of indices equivalent to r and s in Eq. (5.26) correspond to the placement of the quarks in the baryons at the source and sink. For a local current insertion, it is sufficient to have the baryons at the same unit cube site to obtain a nonzero Kronecker delta. The form of the spinors is therefore not relevant for Eq. (5.28). Combining these results, the matrix element of Eq. (5.20) is properly normalized by the choice

$$\frac{g_A}{f_\pi} = \frac{\langle N'|\, A_i^a(0)\,|N\rangle}{\langle 0|\, A_4^a(0)\,|\pi^a\rangle}\frac{\sqrt{N_f M_\pi V_3}}{2M_N}. \tag{5.30}$$

5.1.5 Fitting Strategy

Like the two-point functions, the three-point functions are simultaneously fit, taking into account the correlations among all data. Neglecting the terms due to the finite temporal

extent, the three-point data are fit to

$$
\begin{aligned}
C_{ij}(\tau,t) &= \langle \mathcal{O}_i(t)\mathcal{A}_\mu(\tau)\mathcal{O}_j^\dagger(0)\rangle \\
&\underset{T\to\infty}{\to} \sum_{m^\pm n^\pm} \langle\Omega|\mathcal{O}_i|m^+\rangle \langle m^+|\mathcal{A}_\mu|n^+\rangle \langle n^+|\mathcal{O}_j^\dagger|\Omega\rangle\, e^{-M_m^+\tau} e^{-M_n^+(t-\tau)} \\
&+ \langle\Omega|\mathcal{O}_i|m^-\rangle \langle m^-|\mathcal{A}_\mu|n^+\rangle \langle n^+|\mathcal{O}_j^\dagger|\Omega\rangle\, (-1)^\tau e^{-M_m^-\tau} e^{-M_n^+(t-\tau)} \\
&+ \langle\Omega|\mathcal{O}_i|m^+\rangle \langle m^+|\mathcal{A}_\mu|n^-\rangle \langle n^-|\mathcal{O}_j^\dagger|\Omega\rangle\, (-1)^{(t-\tau)} e^{-M_m^+\tau} e^{-M_n^-(t-\tau)} \\
&+ \langle\Omega|\mathcal{O}_i|m^-\rangle \langle m^-|\mathcal{A}_\mu|n^-\rangle \langle n^-|\mathcal{O}_j^\dagger|\Omega\rangle\, (-1)^t e^{-M_m^-\tau} e^{-M_n^-(t-\tau)}\,. \qquad (5.31)
\end{aligned}
$$

The priors on the amplitudes are set with the same heuristics as the overlap factors. Rather than setting priors for all of the amplitudes individually, the priors are assigned to be $0 \pm x$, where x is approximately $g_A/f_\pi a$. The only exception is the prior on the transition amplitude from the N-like state to itself, the amplitude that gives the matrix element proportional to g_A, which is set to the PDG value of $g_A/f_\pi a$ with a 100% prior width.

The value of g_A is well-known from experiments measuring neutron beta decay [1]. However, until recently, lattice QCD computations have had difficulties reproducing the experimental value, often being $10-20\%$ too low. To prevent bias toward the physical value of g_A, the data have been blinded with blinding factor β. This is done with a constant prefactor that is multiplied by the correlation function data, such that the three point function computes $\beta g_A/f_\pi a$. The key to unblind the data is held by only a few collaboration members, and the value of the blinding is currently unknown. The Fermilab Lattice and MILC collaboration will reveal β once results on three lattice-spacings are in hand, with a complete uncertainty analysis.

5.2 Computation Results

For the computation of the axial charge, many choices of axial current are possible to use. The local axial current is expected to be the least noisy and can be easily renormalized by

the ratio method described in Sec 3.2.3. The current insertion is given by the local operator

$$A^a_\mu(x) = (-1)^{x_\mu}\overline{\chi}(x)\chi(x)\,, \tag{5.32}$$

which has a phase that oscillates only in one direction. The temporal component is proportional to q_μ and vanishes for the axial charge, so the spatial axial currents are used. To improve the signal, the axial currents in each direction are averaged together.

The source and sink operators used here are slightly different than were used for the two-point functions in the previous chapter, in that they were constructed with a different point-splitting at the source side only. One consequence is that fewer statistics are included here. The number of measurements here is about 3000 for both the two- and three-point functions. The fit range for the diagonal operators was reduced to $t \in [2, 8]$ inclusive to account for the increased size of the statistical error bars. The previous analysis was redone for the new operators with the same set of priors, and the results differ only marginally. Fig. 5.1 shows the systematics checks on the new set of correlation functions.

The three-point functions will vanish due to symmetry arguments if the source, sink, and current operators, taken as a whole, do not form a singlet under all of the lattice symmetries. For the two-point functions, constructing a singlet operator is automatic if the source and sink are at the same unit cube site, regardless of what unit cube site is used. For the three-point correlation functions, the current amplitude introduces a nontrivial taste phase, which must be matched by the source and sink operators. The simple picture is to consider the source and sink as their own bilinear, and the taste of the current insertion must be the same as the source-sink bilinear, as detailed in Sec. 3.2.4 For the 16 representation, there is the added complication that the operators transform like a 2-vector at each of the eight unit cube sites. The resolution is that a dot product over the 2-vectors may be taken at each unit cube site.

The most common procedure for constructing a three-point function is to carry out the

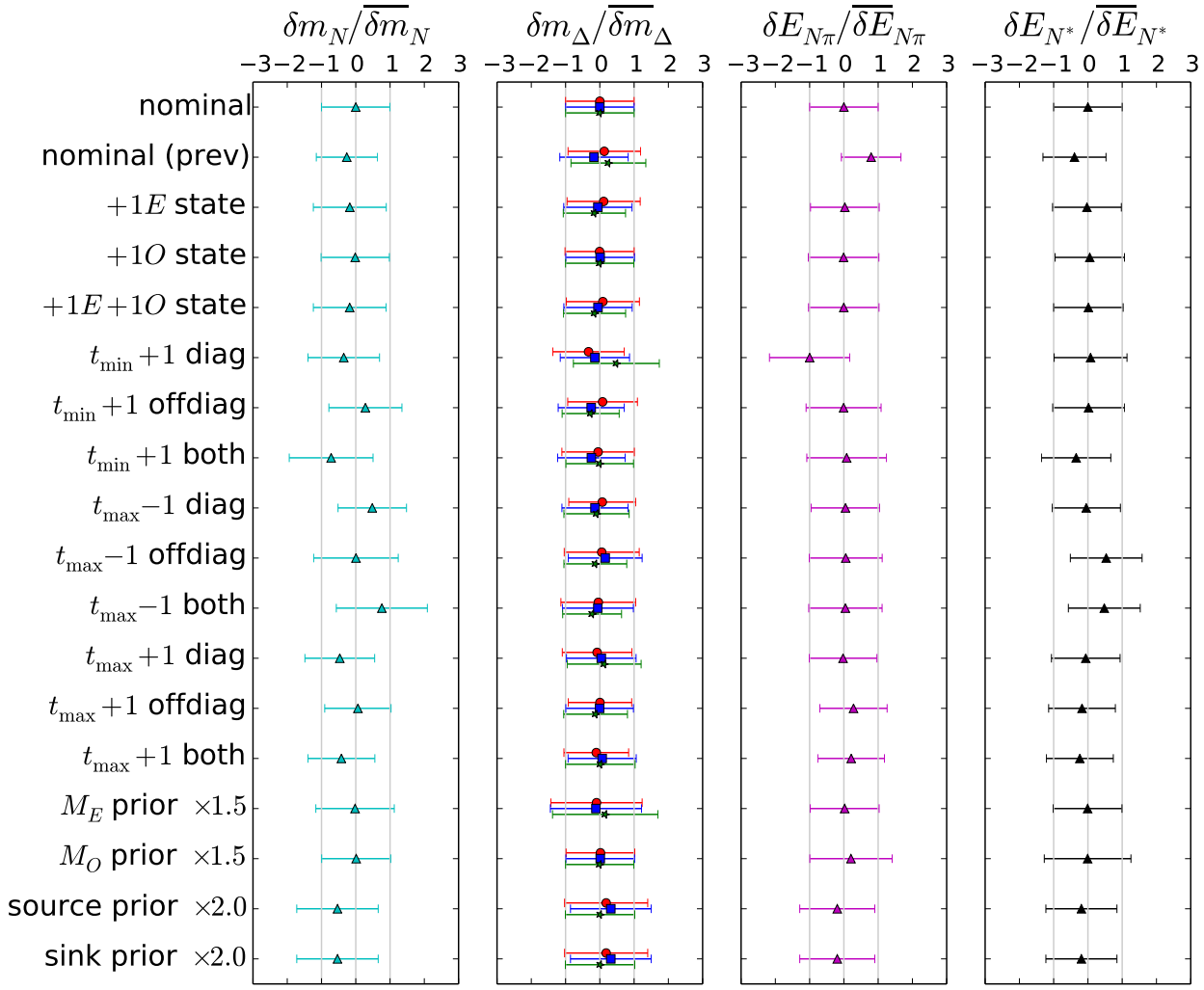

Figure 5.1: Same as Fig. 4.10, except with the set of source and sink operators consistent with the three-point functions. To make contact with the previous chapter, the nominal fit from Fig. 4.10 is included as the second nominal entry.

inversion for the daughter quark sequentially. In this method, a standard quark propagator, which is the result of inverting a generic source object, is used to create the source for a new propagator by applying some transformation to the quark operator at the sink. The quark propagator may be brought back to the current insertion and tied together with a quark propagating from the source and some spin-taste prescription. Thus, an interaction has been introduced into the correlation function. For the three-point functions constructed with staggered quarks, this method is not feasible as it would require (at least) 64 inversions, a factor of eight for the starting source and a factor of eight more for the sequential inversions,

to do one measurement. If more current insertions or time sources are desired, then that factor must also be applied to the number of inversions. To circumvent this technical issue, non-sequential inversions using sources with Gaussian random noise vectors are used in place of the sequential sources, and the operators are tied up with noise constructed to give back the requested operator again. This is detailed in Sec. 3.2.5.

5.2.1 Three-Point Correlation Function Fits

Because we are concentrating on nucleon matrix elements here,[1] the three-point functions are fit for the 16 representation only. As in the case of the two-point correlation functions, the correlation functions involving the class 3 operator have been omitted from the fits. The raw three-point correlation functions, normalized by the pion axial current matrix element, are shown in Fig. 5.2.

The three-point correlation functions for computing the nucleon axial charge are more affected by statistical noise than was expected. These expectations are derived from comparing to computations of baryon three-point functions with similar statistics or for meson three-point functions in staggered lattice QCD. There is some concern that the method of using noisy sink operators is responsible for the statistical errors. To test this, many random wall propagators were computed on a single gauge configuration. These propagators were used to compute the local three-point axial current matrix element with a local baryon operator at both the source and sink. As a comparison, a two-point function was constructed with the exact same source and sink operators, but no current insertion. The two-point function sees no issues with the signal-to-noise when constructed this way, giving an answer with a few percent statistical uncertainty for 100 random noise propagators. This computation of the two point function agrees with the two-point function constructed without the random noise vectors. The corresponding three-point correlation function, where the only difference is that

1. Neutrino physics will also need $N \to \Delta$ transition form factors, but that is beyond the scope of this work.

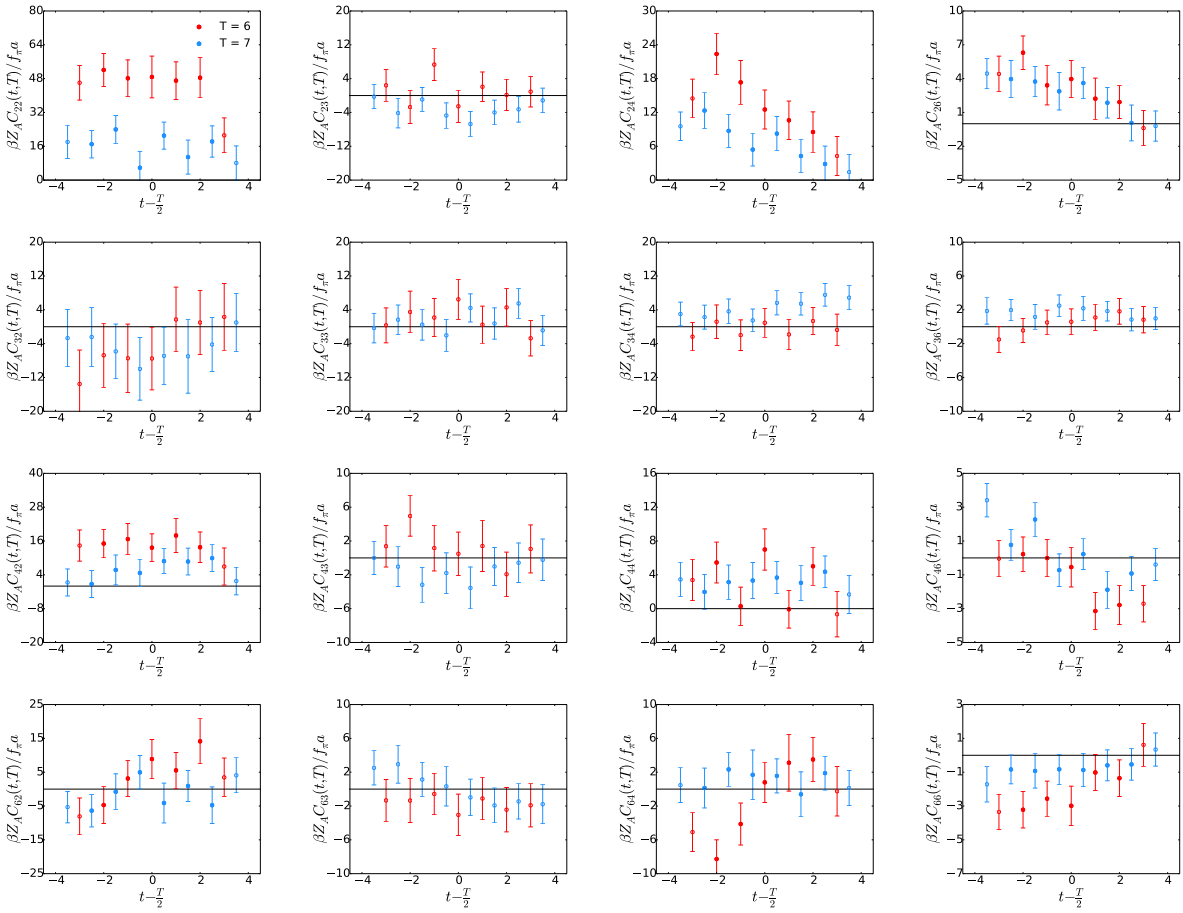

Figure 5.2: Plots of the raw three-point correlation function data for the 16 representation. The correlations functions for two source and sink separations, 6 (red) and 7 (blue) timeslices, and both correlation functions are plotted in the figures. The class 3 operators (second row and column) are again too noisy to put into the fit, and are consistent with zero for most of the data. For simplicity, the class 3 operators are omitted from the fits.

the "noisy leg" of the two-point function is replaced by the quark interaction with a current, sees the same signal-to-noise issue, which is visible in the three-point functions of Fig. 5.2. Had the noisy sink been the principle origin of the statistical fluctuations, the two-point functions constructed with random walls should have suffered from the same signal-to-noise problems as the three-point functions.

The systematics checks for the three-point functions are the same as for the two-point functions, with a few additional checks that pertain only here, including

- $t^3_{\text{fit}} = [2, T-2]$: The fit range for the three-point functions. The same fit range is used

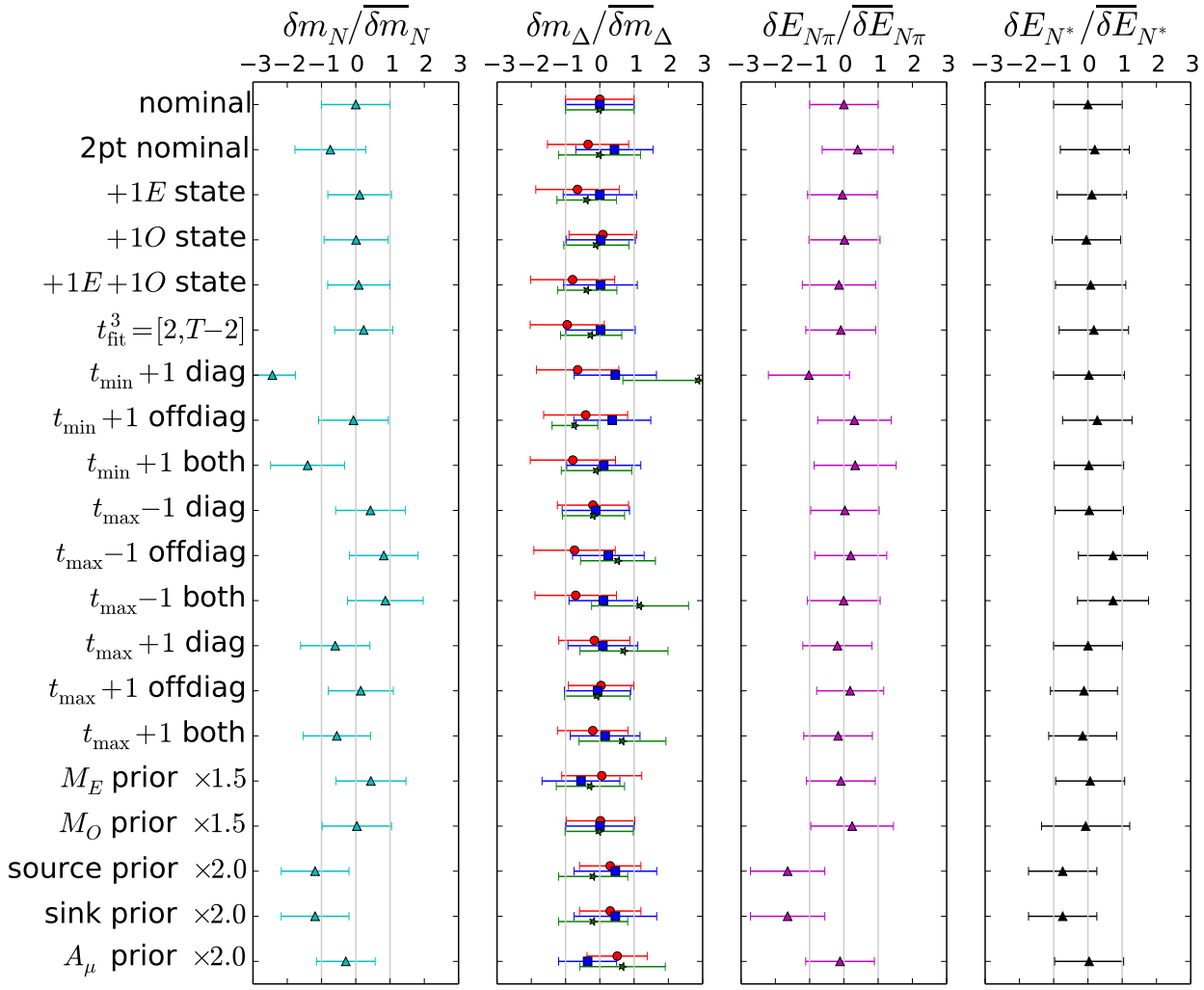

Figure 5.3: Plot of the changes relative to the central values and posteriors of the masses of the 16 representation states under various systematic checks when three-point correlation functions are included in the fits. Most of the same checks that were used in Sec. 4.3.1, with a few additions. The new checks are described in the text. The systematics checks shown here are less stable than they were for the two-point correlation function checks.

for all combinations of source and sink operators. The nominal fit has a fit range of $[1, T-1]$, inclusive, where $T = 6$ or 7.

- A_μ prior ×2.0: The prior width for the current insertion amplitudes is increased by a factor of 2.

The systematics checks with the three-point functions included have larger variations than when the two-point functions are fit alone. The check reducing $t_{\rm min}$ for the diagonal

correlation functions only and for both the diagonal and off-diagonal have large deviations for the N-like mass. This shift can be eliminated by additionally removing the two off-diagonal correlators with a class 6 source operator. This shift is driven by the second Δ-like state, which is most significant at low-t. When the lowest timeslices for the diagonal operators are removed, the restrictions keeping the overlap factors small for this state are removed. The large slopes on the correlation functions in the bottom row of Fig. 5.2 enhance the overlap factors, partially absorbing the contribution of the N-like state from the two-point functions. For the checks that enhance the source and sink operators, the unconstrained state above the N^* state in the last column partially absorbs the N^* state shown, displacing the entire spectrum to lower masses.

Taking the nominal fit with statistical errors only, the nucleon axial charge and the $N-\Delta$ transition charge are

$$\beta g_A M_N / f_\pi = 11.2(1.8)\,, \tag{5.33}$$

$$\beta g_{N\Delta_1} \sqrt{M_N M_\Delta} / f_\pi = 9.8(2.9)\,. \tag{5.34}$$

Using the fit values $M_N a = 0.7740(52)$ and $M_\Delta a = 1.029(11)$ as well as the experimental value of $f_\pi = 130.50(14)$ MeV [1] and the lattice spacing $a = 0.1509(13)$ fm from Ref. [75], the blinded best fit axial current matrix elements are

$$\beta g_A = 1.45(22)\,, \tag{5.35}$$

$$\beta g_{N\Delta_1} = 1.09(33)\,, \tag{5.36}$$

reporting only the statistical errors.

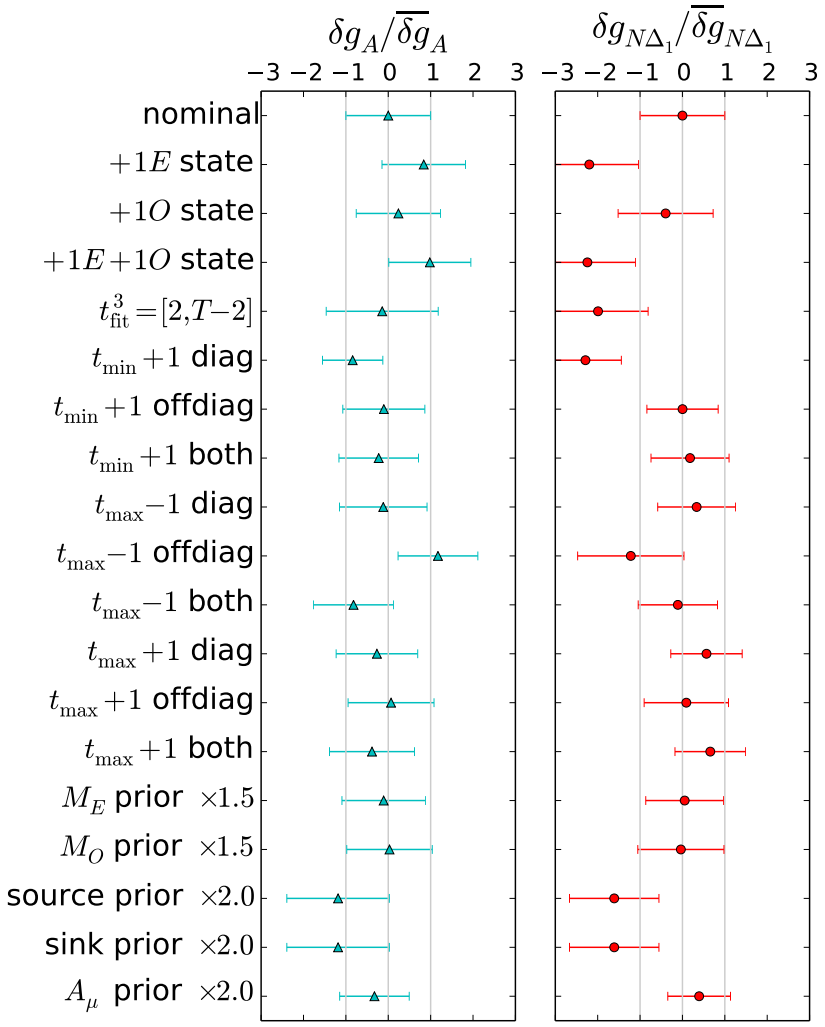

Figure 5.4: Plot of the changes in the current amplitude posteriors for the 16 representation states under various systematic checks. Shown are the axial charge (first column), the N-Δ transition at zero momentum for the second Δ-like taste state. The other $N-\Delta$ transitions are unconstrained by the data. For the statistical precision in this thesis, the other transitions are consistent with zero.

5.2.2 Fitting Challenges

The excited states with small mass splittings from taste violations make the data difficult to fit. The data presented in this dissertation test the limits of constrained curve fitting. The difficulty of developing well-informed priors for the overlap factors gives the fitter a large parameter space to explore and fitting the data requires human intervention. Ideally, the fitting algorithms would be as hands-off as possible. This section details some of the

challenges that were encountered in fitting and puts forth some proposed solutions to the challenges encountered here.

Fitters are not often required to deal with such large, degenerate parameter spaces. As a result, the fitting algorithms are written to move as quickly as possible toward the perceived minimum of the fit. For fits to many exponential decay functions, this is a sub-optimal approach to finding the global minimum of the fit function. To see this, consider a theory that has many low- and high-mass states, but is fit with only a single exponential. Unless the priors for the parameters in the exponential are very aggressive, the fitter will attempt to use the parameters to fit the most well-constrained state or some average of a few of the most well-constrained states, even if the priors are set to accurately and precisely describe one of the excited states. This is the behavior that appears when the fitter is started far from the minimum, when the cross-talk between fit parameters is relatively minimal. The fitting algorithm will start by trying to fit the parameters of every state to the most constraining data, only going back and filling in the higher excited states when the lowest states are well-described.

When the most well-constrained low-mass states are described by the fit parameters, then the data and priors will try to correct the fit parameters to describe the higher-mass states. Occasionally, the fitter will move into a region of parameter space where one of the higher-mass states will supplant a low-mass state. When this happens, the low-mass state will be pushed down beyond what is sensible and becomes spurious. The mass splitting on the state that does the displacing gives a posterior close to the prior central value, but with a small width. The displaced low-mass state then gives a posterior that is far displaced from its prior and with all of its overlap factors consistent with zero.

The chained fitting procedure employed to use the posterior information from the $8'$ fit as priors for the 16 fit is especially vulnerable to these displaced spurious states. This procedure introduces prior widths that are narrower on the higher-mass states than the lower-mass states. In this case, it is initially favorable for the fitter to use the narrow prior

widths to fit the well-constrained states, even if this may not be the case for the global fit. This pushes the fit algorithm to a region of parameter space where it is difficult to escape to the global minimum.

There are two ways to combat these issues. The first way is to change the starting guesses used for the parameters in the fit. The most straightforward solution is to use random starting guesses for overlap factors to find the minimum. If the priors are sensible and the initial values are reasonable, this method was able to find the minimum the majority of trials in the fits presented here. Once a fit minimum is determined, the initial values may be reused to compute variations on the fits quickly.

Another way to prevent spurious states is to arrange priors to remove the phase space where they occur. This is done by changing the reference mass that is used for the fit. In the fits considered here, the reference value was 0 and the lowest-mass state was treated as an energy splitting away from 0. If the states are strictly ordered, as is done in this work, then raising the reference value to some finite mass puts a floor on the lowest mass that can be fit. This value can be set a few prior widths below where the lowest state is expected, yet it will still exclude a large region of parameter space where spurious states appear. This may be paired with another technique where multiple streams of even and odd states are allowed in the fits, each with their own reference mass. The pair of these techniques should be sufficient to eliminate the spurious states due to tight priors on excited states, as is the case in the fits presented in Sec. 4.3.2.

CHAPTER 6

SUMMARY AND CONCLUSIONS

The precision neutrino oscillation experiments that are coming in the following decades will test the limits of scientific understanding of nuclear physics. These experiments will require an equivalent development of theoretical predictions, including creation of advanced nuclear physics models that accurately portray the interactions inside of a nucleus. However, creation of precise nuclear models requires a robust understanding of the free nucleon amplitudes that are used as inputs to the nuclear models. The axial form factor, one of the essential free nucleon amplitudes, is especially difficult to constrain via experimental measurements because it is accessed only through interactions involving a weak current. Lattice QCD offers an independent approach for computing the form factors of the nucleon, making it an attractive remedy for this difficulty. The work in this dissertation provides a realistic estimate of the uncertainties in the determination of the axial form factor from the world's best determination on nearly-free nucleon targets. The axial form factor at zero momentum transfer, the axial charge, is also computed using staggered lattice QCD for one ensemble at physical pion mass. The work in this dissertation represents the first step in a new initiative to use lattice QCD to compute matrix elements needed by neutrino oscillation experiments.

In Chapter 2, the z expansion parametrization of the axial form factor is fit to deuterium bubble chamber data to get an estimate of the true form factor uncertainty. The results in Figs. 2.7 and 2.8 show that the form factor and cross section uncertainties are significantly underestimated when the dipole parametrization is used. The uncertainty in the free nucleon form factor is significant, making up a large portion of the data-theory discrepancy shown in Fig. 2.9. These observations indicate that the axial form factor is not as well-determined as the dipole model implies. If studies such as that in Fig. 2.9 are to be used to constrain nuclear models, then uncertainties in the free nucleon form factor uncertainties must be quantified realistically, and a program is needed—such as lattice QCD—to reduce them..

Chapters 3–5 present the first steps in such a program. Chapter 3 delineates the group

theory needed to compute baryon observables with lattice QCD using the staggered action. In this chapter, the staggered timeslice group is fully decomposed into its spin and taste subgroups, making the decomposition from the continuum group to the lattice subgroup manifest. From the group transformations, the spectrum of zero-momentum states expected for each combination of isospin and spin-taste is predicted. These results are used in Chapter 4, where the spectrum of the $8'$ and 16 representations of the staggered timeslice group are computed. The extra taste symmetry in the group transformations results in extra baryon taste states. Due to strong correlations among the correlation function data, the spectrum of the staggered baryons can be precisely predicted. Fig. 4.8 depicts the stability of the 16 representation spectrum, showing that the correlation functions constrain many more states than would be implied from a variational method alone. The stability of results when subjected to various alternate fits and systematics checks is shown in Fig. 4.10. This stability gives confidence that the mass posteriors presented in Sec. 4.3.3 are a robust an accurate result of the underlying data.

Chapter 5 goes over the computation of the axial charge from staggered lattice QCD. The three-point correlation function data in Fig. 5.2 are simultaneously fit with the two-point function data to extract the axial charge. Despite large statistical errors, cross-correlations among the data improve the extraction of observables from the data, allowing for more precise extraction of the axial charge. The computation is absolutely normalized by forming a ratio with an axial current matrix element coupled to a pion. Removing the extraneous factors, the computation yields a blinded result of $\beta g_A = 1.45(22)$ with statistical errors only. Extensions to this calculation will include computing the axial form factor with nonzero momentum and including ensembles with smaller lattice spacings for a full continuum extrapolation. Fits to the form factor shape will be computed with the z expansion parametrization, providing a set of coefficients and a covariance matrix to be implemented into the Monte Carlo generators used in neutrino physics. The axial form factor data will be unblinded when all systematic uncertainties have been estimated and fit procedures have been finalized.

The work in this dissertation provides an overview of the importance of the axial form factor to neutrino physics. Although the standard dipole ansatz underestimates its uncertainties, the model-independent z expansion offers a superior alternative. It is already available as an option in GENIE, using our z fits of the deuterium bubble-chamber data. From now on, however, lattice QCD offers a way to access the nucleon matrix elements directly, providing an alternative determination for matrix elements that are difficult to extract from experiment. These results will provide essential ingredients to the nuclear models on which determinations of the neutrino oscillation experiments rely. Thus, it is apparent that lattice QCD will prove to be an invaluable tool for neutrino oscillation physics in the years to come, providing the missing puzzle pieces necessary to study some of the most elusive and interesting particles known to this day.

APPENDIX A

GROUP THEORY DETAILS

In this appendix, we will enumerate the group structure of the staggered action in more detail. The symmetries of a timeslice with the staggered quark action include staggered shifts, rotations, spatial inversion, and the temporal taste transformation Ξ_4.

Even when all transformations but shifts are neglected, the full staggered quark shift group is cumbersome. It is simpler to apply the strategy of Ref. [56] and work with translations and discrete taste transformations rather than shifts:

$$T_\mu \equiv \left[\left(S_\mu\right)^2\right]^{-1/2}, \quad \Xi_\mu \equiv S_\mu \left(T_\mu\right)^{-1} . \tag{A.1}$$

These operators are nonlocal, but the desired shift group the subgroup obtained from using the local operators $S_\mu = \Xi_\mu T_\mu$ as generators instead of both the Ξ_μ and T_μ separately. The consequence of taking this subgroup is to eliminate the irreps that would have momentum larger than half the maximum momentum; in other words, the phases obtained from translating high-momentum irreps are made to be degenerate with the staggered phases obtained from taste transformations.

A.1 Discrete Taste Transformations

Focusing only on the subgroup of discrete taste transformations, one finds that the resulting symmetries are part of a quotient of a direct product group [63]:

$$\{\Xi_{12}, \Xi_{23}\} \times \{\Xi_{123}, \Xi_4\} \,/\, \{-\mathbb{1} \times -\mathbb{1}\} \cong \left(\mathbb{Q}_8 \times D_4\right) / \mathbb{Z}_2 \,. \tag{A.2}$$

The set of elements listed in braces are the generators of that group. Here, $\mathbb{Q}_8$ denotes the order 8 quaternion group (generated by the Pauli spin matrices $i\sigma_i$) and D_4 specifies the order 8 dihedral group (generated by $i\sigma_2$ and σ_3).

$\mathbb{Q}_8$	D_4	$\{\mathbb{1}\}$	$\{-\mathbb{1}\}$	$\{\pm\Xi_{12}/\Xi_{123}\}$	$\{\pm\Xi_{13}/\Xi_{1234}\}$	$\{\pm\Xi_{23}/\Xi_4\}$
a_1	a_{++}	1	1	1	1	1
b_x	b_{-+}	1	1	-1	-1	1
b_y	b_{--}	1	1	-1	1	-1
b_z	b_{+-}	1	1	1	-1	-1
σ	σ	2	-2	0	0	0

Table A.1: Character table for the $\mathbb{Q}_8$ and D_4 groups. The character tables for both groups are identical, but the irreps and group operations are not the same.

The $\mathbb{Z}_2$ factor in the quotient forces the $-\mathbb{1}$ element of both groups to be the same element. If we define "fermionic" ("bosonic") irreps to mean irreps with a negative (positive) character for the conjugacy class containing the $-\mathbb{1}$ element, then this quotient eliminates the irreducible representations of the direct product group that have different characters for the $-\mathbb{1}$ conjugacy class. In other words, we may only pair bosonic irreps of the $\mathbb{Q}_8$ subgroup with bosonic irreps of D_4, and similarly fermionic with fermionic.

The group symmetries have a very clean interpretation when written in this way. The quaternion group factor $\mathbb{Q}_8$ represents the taste transformations induced by shifts in two independent directions, connecting even sites only to other even sites and odd sites to odd sites. The dihedral group factor D_4 represents the shifts by three lattice sites, which connects the odd sites to the odd sites (that will be referred to as site-parity), and the taste transformation in the temporal direction. Each of these groups conveniently has the same character table, displayed in Table A.1. This means that they both have five irreducible representations; four of these representations are one-dimensional and are bosonic representations, while the last is a two-dimensional fermionic representation. As we will see, the two-dimensional representations will both make up factors of two in the dimension of the fermionic irreducible representations of the full lattice timeslice group.

A.2 Rotations

The rotations belong to the group SW_3, the cubic rotation group. This group has five irreducible representations, with an additional three that appear in the double cover. There are

two 1-dimensional, one 2-dimensional, and two 3-dimensional irreducible representations in the single cover of the group. The two 1-dimensional and two 3-dimensional representations differ only by a factor of -1 in the representation matrices for the group generators R_{ij}. The matrices with a negative character are those corresponding to representations with a larger spin.

Combining the rotational symmetries with the discrete taste symmetries mixes up operators with the same site-parity and leads to the semidirect product $\mathbb{Q}_8 \rtimes SW_3$. In Ref. [56], this factor was isomorphic to the four-dimensional cubic rotation group, SW_4. The irreps of the fermionic representations are either four- or eight-dimensional, corresponding to operators that are a one- or two-vector at each of the four sites with the same site-parity within a unit cube. The bosonic representations are constructed from sums of operators over these four sites.

Under rotations, the orbits of the representations are simple to determine. The two easiest cases are the trivial irrep, which will only transform into itself, and the fermionic irrep, which must transform because group orbits can only connect irreps of the same dimension. The remaining three irreducible representations transform into each other like a 3-vector. This can be seen if one notes that the rotations act by interchanging the operators Ξ_{ij} with each other. This nontrivial orbit is represented by labeling the irreps of $\mathbb{Q}_8$ as A^k in Table A.3, where k denotes the operator $\epsilon_{ijk}\Xi_{ij}$ that has a positive character in said irrep.

Including spatial inversion takes the group factor from $SW_3 \to W_3$. The new operator I_S does not commute with the body-diagonal taste transformation Ξ_{123}. This is remedied by replacing I_S with the nearly-equivalent continuum parity operator $I_S\Xi_4$, which is a good symmetry of the lattice at zero momentum. The effect is simply to introduce a group parity, doubling the number of irreducible representations. In practice, constructing lattice operators with definite parity requires spreading the operator out over the entire temporal extent, which would introduce unwanted contact terms into measurements of observables. As a result, parity is often neglected in the construction of operators. A full summary of the

SW_3	$\{\mathbb{1}\}$	$\{+R\}$	$\{+RR'\}$	$\{\pm R^2\}$	$\{\pm RR'R\}$	$\{-\mathbb{1}\}$	$\{-R\}$	$\{-RR'\}$
A_1	1	1	1	1	1	1	1	1
A_2	1	-1	1	-1	1	1	-1	1
E	2	0	-1	0	2	2	0	-1
T_1	3	1	0	-1	-1	3	1	0
T_2	3	-1	0	1	-1	3	-1	0
$\bar{2}$	2	$\sqrt{2}$	1	0	0	-2	$-\sqrt{2}$	-1
2	2	$-\sqrt{2}$	1	0	0	-2	$\sqrt{2}$	-1
4	4	0	-1	0	0	-4	0	1

Table A.2: Character table for the double cover of the W_3 (cubic rotation) group. The single cover of the rotation group is the 5×5 block in the upper-left corner of this character table.

irreducible representations is given in Table A.3.

A.3 Nonzero Momentum

The direction of the momentum can be changed under rotations. This means that the little groups of the rotation group are different when generalizing to nonzero momentum. The semidirect product now acts on the subgroup $\mathcal{T}_M \times \mathbb{Q}_8$ instead of just the quaternion subgroup.

Some of the considerations to take into account when generalizing to nonzero momentum include

1. the size of the orbits under SW_3 change,

2. continuum parity takes $p \to -p$ and must be paired with other symmetry operations to be represented in the little group, and

3. the directions of the momenta and $\mathbb{Q}_8$ irreps transform together, and so the dimensions of the irreps may be smaller than the product of the two constituent orbit sizes.

$\mathcal{T}_M \otimes \mathcal{Q}_8$	Dim.	Orb.Size	Gens.	Little grp.	LG Irreps	Mult.	Tot.Dim.
$(0,0,0) \otimes A^0$	1	1	$\{R_{ij}, \Xi_4 I_S\}$	$SW_3 \times \mathbb{Z}_2$	$A_1^{\pm}, A_2^{\pm}$	4×4	1
					$E^{\pm}$	2×4	2
					$T_1^{\pm}, T_2^{\pm}$	4×4	3
$(0,0,0) \otimes A^k$	1	3	$\{R_{12}, R_{13}^2, \Xi_4 I_S\}$	$D_4 \times \mathbb{Z}_2$	$A_0^{\pm}, A_1^{\pm}, A_2^{\pm}, A_3^{\pm}$	8×4	3
					$\sigma^{\pm}$	2×4	6
$(0,0,0) \otimes \sigma$	2	1	$\{R_{ij}, \Xi_4 I_S\}$	$\widetilde{SW_3} \times \mathbb{Z}_2$	$2^{\pm}, \overline{2}^{\pm}$	4	4×2
					$4^{\pm}$	2	8×2
Summary:							
bosonic						16	1
						8	2
						48	3
						8	6
fermionic						4	8
						2	16

Table A.3: Summary of irrep multiplicities and dimensions for the lattice symmetries at zero momentum after going through the Wigner little group analysis. For this case, the bosonic irreps have three parities, corresponding to the operators Ξ_{123}, Ξ_4, and continuum parity $\Xi_4 I_S$. A factor of four in the multiplicity column of this table represents the first two of these parities, and the continuum parity is included in counting the total representations in the Little Group Irreps column. The fermionic irreps have only the continuum parity, $\Xi_4 I_S$, where the other parities from Ξ_{123} and Ξ_4 are absorbed into the operator dimension.

$\mathcal{T}_M \otimes \mathcal{Q}_8$	Dim.	Orb.Size	Gens.	Little grp.	LG Irreps	Mult.	Tot.Dim.
$(0,0,\pm p)\otimes A^0$	1	6	$\{R_{12}, R_{13}^2\Xi_4 I_S\}$	D_4	A_0, A_1, A_2, A_3	4×4	6
					σ	1×4	12
$(0,0,\pm p)\otimes A^k$ $(k \parallel p)$	1	6	$\{R_{12}, R_{13}^2\Xi_4 I_S\}$	D_4	A_0, A_1, A_2, A_3	4×4	6
					σ	1×4	12
$(0,0,\pm p)\otimes A^k$ $(k \perp p)$	1	12	$\{R_{12}^2, R_{13}^2\Xi_4 I_S\}$	$\mathbb{Z}_2\times\mathbb{Z}_2$	$A_+^+, A_+^-, A_-^+, A_-^-$	4×4	12
$(0,0,\pm p)\otimes \sigma$	2	6	$\{R_{12}, R_{13}^2\Xi_4 I_S\}$	D_8	$2, \overline{2}$	2	24×2
Summary:							
bosonic						32	6
						24	12
fermionic						2	48

Table A.4: The same as Table A.3, but with nonzero momentum in a single direction. The addition of momentum has forced the continuum parity to be mixed up within the irreps. The double cover of D_4 extends the group to D_8, which introduces two new conjugacy classes of dimension 2.

$\mathcal{T}_M \otimes \mathcal{Q}_8$	Dim.	Orb.Size	Gens.	Little grp.	LG Irreps	Mult.	Tot.Dim.
$(\pm p, \pm p, 0) \otimes A^0$	1	12	$\left\{R_{13}^2 R_{12}^{-1}, R_{12}^2 \Xi_4 I_S\right\}$	$\mathbb{Z}_2 \times \mathbb{Z}_2$	$A_+^+, A_+^-, A_-^+, A_-^-$	4×4	12
$(\pm p, \pm p, 0) \otimes A^k$ $(k \perp p)$	1	12	$\left\{R_{13}^2 R_{12}^{-1}, R_{12}^2 \Xi_4 I_S\right\}$	$\mathbb{Z}_2 \times \mathbb{Z}_2$	$A_+^+, A_+^-, A_-^+, A_-^-$	4×4	12
$(\pm p, \pm p, 0) \otimes A^k$ $(k \parallel p)$	1	24	$\left\{R_{12}^2 \Xi_4 I_S\right\}$	$\mathbb{Z}_2$	A^+, A^-	2×4	24
$(\pm p, \pm p, 0) \otimes \sigma$	2	12	$\left\{R_{13}^2 R_{12}^{-1}, R_{12}^2 \Xi_4 I_S\right\}$	D_4	2	1	48×2
Summary:							
bosonic						32 8	12 24
fermionic						1	96

Table A.5: The same as Table A.3, but with identical nonzero momentum in two directions. The double cover of $\mathbb{Z}_2 \times \mathbb{Z}_2$ is the group D_4.

$\mathcal{T}_M \otimes \mathcal{Q}_8$	Dim.	Orb.Size	Gens.	Little grp.	LG Irreps	Mult.	Tot.Dim.
$(\pm p, \pm p, \pm p) \otimes A^0$	1	8	$\{R_{13}^2 R_{12} \Xi_4 I_S,$ $R_{12}^2 R_{13} \Xi_4 I_S\}$	D_3	A_0, A_1	2×4	8
					σ	1×4	16
$(\pm p, \pm p, \pm p) \otimes A^k$	1	24	$\{R_{13}^2 R_{12} \Xi_4 I_S\}$	$\mathbb{Z}_2$	A^+, A^-	2×4	24
$(\pm p, \pm p, \pm p) \otimes \sigma$	2	8	$\{R_{13}^2 R_{12} \Xi_4 I_S,$ $R_{12}^2 R_{13} \Xi_4 I_S\}$	$D_3 \times \mathbb{Z}_2$	$1^+, 1^-$	2	16×2
					2	1	32×2
Summary:							
bosonic						8	8
						4	16
						8	24
fermionic						2	32
						1	64

Table A.6: The same as Table A.3, but with identical nonzero momentum in all three directions. The double cover of D_3 is the trivial extension to $D_3 \times \mathbb{Z}_2$.

REFERENCES

[1] C. Patrignani *et al.* [Particle Data Group], Chin. Phys. C **40**, no. 10, 100001 (2016). doi:10.1088/1674-1137/40/10/100001

[2] L. Aliaga Soplin, Ph. D. thesis, William-Mary Coll., 2016. FERMILAB-THESIS-2016-03.

[3] J. A. Formaggio and G. P. Zeller, Rev. Mod. Phys. **84**, 1307 (2012) doi:10.1103/RevModPhys.84.1307 [arXiv:1305.7513 [hep-ex]].

[4] F. P. An *et al.* [Daya Bay Collaboration], Phys. Rev. Lett. **108**, 171803 (2012) doi:10.1103/PhysRevLett.108.171803 [arXiv:1203.1669 [hep-ex]].

[5] R. Acciarri *et al.* [DUNE Collaboration], arXiv:1512.06148 [physics.ins-det].

[6] H. Nunokawa, S. J. Parke and J. W. F. Valle, Prog. Part. Nucl. Phys. **60**, 338 (2008) doi:10.1016/j.ppnp.2007.10.001 [arXiv:0710.0554 [hep-ph]].

[7] I. Esteban, M. C. Gonzalez-Garcia, M. Maltoni, I. Martinez-Soler and T. Schwetz, JHEP **1701**, 087 (2017) doi:10.1007/JHEP01(2017)087 [arXiv:1611.01514 [hep-ph]].

[8] K. Iwamoto and O. B. O. T. Collaboration, PoS ICHEP **2016**, 517 (2016).

[9] H. B. Nielsen and M. Ninomiya, Phys. Lett. **105B**, 219 (1981). doi:10.1016/0370-2693(81)91026-1

[10] C. Bernard *et al.*, PoS LAT **2007**, 090 (2007) [arXiv:0710.1118 [hep-lat]].

[11] C. Bernard, Phys. Rev. D **73**, 114503 (2006) doi:10.1103/PhysRevD.73.114503 [hep-lat/0603011].

[12] A. S. Kronfeld, PoS LAT **2007**, 016 (2007) [arXiv:0711.0699 [hep-lat]].

[13] A. S. Kronfeld, Ann. Rev. Nucl. Part. Sci. **62**, 265 (2012) doi:10.1146/annurev-nucl-102711-094942 [arXiv:1203.1204 [hep-lat]].

[14] R. Aaij *et al.* [LHCb Collaboration], Nature Phys. **11**, 743 (2015) doi:10.1038/nphys3415 [arXiv:1504.01568 [hep-ex]].

[15] J. L. Rosner, S. Stone and R. S. Van de Water, [arXiv:1509.02220 [hep-ph]].

[16] J. A. Bailey *et al.* [MILC Collaboration], Phys. Rev. D **92**, no. 3, 034506 (2015) doi:10.1103/PhysRevD.92.034506 [arXiv:1503.07237 [hep-lat]].

[17] J. A. Bailey *et al.* [Fermilab Lattice and MILC Collaborations], Phys. Rev. D **92**, no. 1, 014024 (2015) doi:10.1103/PhysRevD.92.014024 [arXiv:1503.07839 [hep-lat]].

[18] W. Detmold, C. Lehner and S. Meinel, Phys. Rev. D **92**, no. 3, 034503 (2015) doi:10.1103/PhysRevD.92.034503 [arXiv:1503.01421 [hep-lat]].

[19] J. Green, M. Engelhardt, S. Krieg, J. Negele, A. Pochinsky and S. Syritsyn, PoS LATTICE **2012**, 170 (2012) [arXiv:1211.0253 [hep-lat]].

[20] S. Durr *et al.*, JHEP **1108**, 148 (2011) doi:10.1007/JHEP08(2011)148 [arXiv:1011.2711 [hep-lat]].

[21] Y. B. Yang, M. Gong, K. F. Liu and M. Sun, PoS LATTICE **2014**, 138 (2014) [arXiv:1504.04052 [hep-ph]].

[22] B. J. Owen, J. Dragos, W. Kamleh, D. B. Leinweber, M. S. Mahbub, B. J. Menadue and J. M. Zanotti, Phys. Lett. B **723**, 217 (2013) doi:10.1016/j.physletb.2013.04.063 [arXiv:1212.4668 [hep-lat]].

[23] S. Dinter, C. Alexandrou, M. Constantinou, V. Drach, K. Jansen and D. B. Renner, Phys. Lett. B **704**, 89 (2011) doi:10.1016/j.physletb.2011.09.002 [arXiv:1108.1076 [hep-lat]].

[24] T. Bhattacharya, S. D. Cohen, R. Gupta, A. Joseph, H. W. Lin and B. Yoon, Phys. Rev. D **89**, no. 9, 094502 (2014) doi:10.1103/PhysRevD.89.094502 [arXiv:1306.5435 [hep-lat]].

[25] T. Bhattacharya, R. Gupta and B. Yoon, PoS LATTICE **2014**, 141 (2014) [arXiv:1503.05975 [hep-lat]].

[26] R. Gupta, T. Bhattacharya, A. Joseph, H. W. Lin and B. Yoon, PoS LATTICE **2014**, 152 (2014) [arXiv:1501.07639 [hep-lat]].

[27] T. Bhattacharya, V. Cirigliano, S. Cohen, R. Gupta, H. W. Lin and B. Yoon, Phys. Rev. D **94**, no. 5, 054508 (2016) doi:10.1103/PhysRevD.94.054508 [arXiv:1606.07049 [hep-lat]].

[28] S. Ohta [RBC and UKQCD Collaborations], PoS LATTICE **2013**, 274 (2014) [arXiv:1309.7942 [hep-lat]].

[29] S. N. Syritsyn *et al.*, Phys. Rev. D **81**, 034507 (2010) doi:10.1103/PhysRevD.81.034507 [arXiv:0907.4194 [hep-lat]].

[30] J. Green, M. Engelhardt, S. Krieg, J. Negele, A. Pochinsky and S. Syritsyn, PoS LATTICE **2012**, 170 (2012) [arXiv:1211.0253 [hep-lat]].

[31] S. Syritsyn *et al.*, PoS LATTICE **2014**, 134 (2015) [arXiv:1412.3175 [hep-lat]].

[32] M. Gockeler *et al.* [QCDSF/UKQCD Collaboration], PoS LATTICE **2010**, 163 (2010) [arXiv:1102.3407 [hep-lat]].

[33] J. R. Green, J. W. Negele, A. V. Pochinsky, S. N. Syritsyn, M. Engelhardt and S. Krieg, Phys. Rev. D **90**, 074507 (2014) doi:10.1103/PhysRevD.90.074507 [arXiv:1404.4029 [hep-lat]].

[34] E. Berkowitz *et al.*, arXiv:1704.01114 [hep-lat].

[35] C. H. Llewellyn Smith, Phys. Rept. **3**, 261 (1972). doi:10.1016/0370-1573(72)90010-5

[36] K. A. Olive *et al.* [Particle Data Group], Chin. Phys. C **38**, 090001 (2014). doi:10.1088/1674-1137/38/9/090001

[37] V. Bernard, L. Elouadrhiri and U. G. Meissner, J. Phys. G **28**, R1 (2002) doi:10.1088/0954-3899/28/1/201 [hep-ph/0107088].

[38] A. A. Aguilar-Arevalo *et al.* [MiniBooNE Collaboration], Phys. Rev. D **81**, 092005 (2010) doi:10.1103/PhysRevD.81.092005 [arXiv:1002.2680 [hep-ex]].

[39] B. Bhattacharya, R. J. Hill and G. Paz, Phys. Rev. D **84**, 073006 (2011) doi:10.1103/PhysRevD.84.073006 [arXiv:1108.0423 [hep-ph]].

[40] G. P. Lepage and S. J. Brodsky, Phys. Rev. D **22**, 2157 (1980). doi:10.1103/PhysRevD.22.2157

[41] A. S. Meyer, M. Betancourt, R. Gran and R. J. Hill, Phys. Rev. D **93**, no. 11, 113015 (2016) doi:10.1103/PhysRevD.93.113015 [arXiv:1603.03048 [hep-ph]].

[42] N. J. Baker *et al.*, Phys. Rev. D **23**, 2499 (1981). doi:10.1103/PhysRevD.23.2499

[43] W. A. Mann *et al.*, Phys. Rev. Lett. **31**, 844 (1973). doi:10.1103/PhysRevLett.31.844

[44] S. J. Barish *et al.*, Phys. Rev. D **16**, 3103 (1977). doi:10.1103/PhysRevD.16.3103

[45] K. L. Miller *et al.*, Phys. Rev. D **26**, 537 (1982). doi:10.1103/PhysRevD.26.537

[46] T. Kitagaki *et al.*, Phys. Rev. D **28**, 436 (1983). doi:10.1103/PhysRevD.28.436

[47] S. K. Singh, Nucl. Phys. B **36**, 419 (1972). doi:10.1016/0550-3213(72)90227-1

[48] R. Bradford, A. Bodek, H. S. Budd and J. Arrington, Nucl. Phys. Proc. Suppl. **159**, 127 (2006) doi:10.1016/j.nuclphysbps.2006.08.028 [hep-ex/0602017].

[49] G. Lee, J. R. Arrington and R. J. Hill, Phys. Rev. D **92**, no. 1, 013013 (2015) doi:10.1103/PhysRevD.92.013013 [arXiv:1505.01489 [hep-ph]].

[50] G. Shen, L. E. Marcucci, J. Carlson, S. Gandolfi and R. Schiavilla, Phys. Rev. C **86**, 035503 (2012) doi:10.1103/PhysRevC.86.035503 [arXiv:1205.4337 [nucl-th]].

[51] A. Bodek, S. Avvakumov, R. Bradford and H. S. Budd, Eur. Phys. J. C **53**, 349 (2008) doi:10.1140/epjc/s10052-007-0491-4 [arXiv:0708.1946 [hep-ex]].

[52] J. C. Bernauer *et al.* [A1 Collaboration], Phys. Rev. C **90**, no. 1, 015206 (2014) doi:10.1103/PhysRevC.90.015206 [arXiv:1307.6227 [nucl-ex]].

[53] G. A. Fiorentini *et al.* [MINERvA Collaboration], Phys. Rev. Lett. **111**, 022502 (2013) doi:10.1103/PhysRevLett.111.022502 [arXiv:1305.2243 [hep-ex]].

[54] M. Martini, M. Ericson and G. Chanfray, Phys. Rev. C **84**, 055502 (2011) doi:10.1103/PhysRevC.84.055502 [arXiv:1110.0221 [nucl-th]].

[55] C. Andreopoulos *et al.*, Nucl. Instrum. Meth. A **614**, 87 (2010) doi:10.1016/j.nima.2009.12.009 [arXiv:0905.2517 [hep-ph]].

[56] M. F. L. Golterman and J. Smit, Nucl. Phys. B **255**, 328 (1985). doi:10.1016/0550-3213(85)90138-5

[57] L. H. Karsten and J. Smit, Nucl. Phys. B **183**, 103 (1981). doi:10.1016/0550-3213(81)90549-6

[58] N. Kawamoto and J. Smit, Nucl. Phys. B **192**, 100 (1981).

[59] F. Gliozzi, Nucl. Phys. B **204**, 419 (1982). doi:10.1016/0550-3213(82)90199-7

[60] A. Duncan, R. Roskies and H. Vaidya, Phys. Lett. **114B**, 439 (1982). doi:10.1016/0370-2693(82)90088-0

[61] H. Kluberg-Stern, A. Morel, O. Napoly and B. Petersson, Nucl. Phys. B **220**, 447 (1983). doi:10.1016/0550-3213(83)90501-1

[62] M. F. L. Golterman and J. Smit, Nucl. Phys. B **245**, 61 (1984). doi:10.1016/0550-3213(84)90424-3

[63] G. W. Kilcup and S. R. Sharpe, Nucl. Phys. B **283**, 493 (1987). doi:10.1016/0550-3213(87)90285-9

[64] J. A. Bailey, Phys. Rev. D **75**, 114505 (2007) doi:10.1103/PhysRevD.75.114505 [hep-lat/0611023].

[65] G. P. Lepage, CLNS-89-971, C89-06-04.

[66] D. B. Renner, PoS LAT **2009**, 018 (2009) [arXiv:1002.0925 [hep-lat]].

[67] H. W. Lin, PoS LATTICE **2012**, 013 (2012) [arXiv:1212.6849 [hep-lat]].

[68] J. M. M. Hall, D. B. Leinweber and R. D. Young, Phys. Rev. D **88**, no. 1, 014504 (2013) doi:10.1103/PhysRevD.88.014504 [arXiv:1305.3984 [hep-lat]].

[69] M. Luscher, Commun. Math. Phys. **104**, 177 (1986). doi:10.1007/BF01211589

[70] S. R. Beane and M. J. Savage, Phys. Rev. D **70**, 074029 (2004) doi:10.1103/PhysRevD.70.074029 [hep-ph/0404131].

[71] A. A. Khan *et al.*, Phys. Rev. D **74**, 094508 (2006) doi:10.1103/PhysRevD.74.094508 [hep-lat/0603028].

[72] A. Bazavov *et al.* [MILC Collaboration], Rev. Mod. Phys. **82**, 1349 (2010) doi:10.1103/RevModPhys.82.1349 [arXiv:0903.3598 [hep-lat]].

[73] R. Li, Ph. D. thesis, Indiana U., 2014.

[74] A. S. Meyer, R. J. Hill, A. S. Kronfeld, R. Li and J. N. Simone, PoS LATTICE **2016**, 179 (2016) [arXiv:1610.04593 [hep-lat]].

[75] A. Bazavov *et al.* [MILC Collaboration], Phys. Rev. D **93**, no. 9, 094510 (2016) doi:10.1103/PhysRevD.93.094510 [arXiv:1503.02769 [hep-lat]].

[76] A. Bazavov *et al.* [MILC Collaboration], Phys. Rev. D **87**, no. 5, 054505 (2013) doi:10.1103/PhysRevD.87.054505 [arXiv:1212.4768 [hep-lat]].

[77] G. P. Lepage, B. Clark, C. T. H. Davies, K. Hornbostel, P. B. Mackenzie, C. Morningstar and H. Trottier, Nucl. Phys. Proc. Suppl. **106**, 12 (2002) doi:10.1016/S0920-5632(01)01638-3 [hep-lat/0110175].

[78] G. P. Lepage "Corrfitter v5.0.1," https://github.com/gplepage/corrfitter

[79] G. P. Lepage and Gohlke, C. "Lsqfit v8.1," https://github.com/gplepage/lsqfit

[80] G. P. Lepage "Gvar v8.1," https://github.com/gplepage/gvar

[81] A. Bazavov *et al.* [Fermilab Lattice and MILC Collaborations], Phys. Rev. D **90**, no. 7, 074509 (2014) doi:10.1103/PhysRevD.90.074509 [arXiv:1407.3772 [hep-lat]].